Monika Winkler, BSc BSc MSc

Investigation into the possibility of hyphenating laser ablation to flow digestion

DISSERTATION

zur Erlangung des akademischen Grades

Doktorin der technischen Wissenschaften

eingereicht an der

Technischen Universität Graz

Betreuer

Em. Univ.-Prof. Dr. techn. Dipl.-Ing. Günter Knapp

Institut für Analytische Chemie und Lebensmittelchemie

Graz, März 2019

EIDESSTATTLICHE ERKLÄRUNG

Ich erkläre an Eides statt, dass ich die vorliegende Arbeit selbstständig verfasst, andere als die angegebenen Quellen/Hilfsmittel nicht benutzt, und die den benutzten Quellen wörtlich und inhaltlich entnommenen Stellen als solche kenntlich gemacht habe. Das in TUGRAZonline hochgeladene Textdokument ist mit der vorliegenden Dissertation identisch.

Datum

Unterschrift

Danksagung

Im Laufe meiner Dissertation habe ich von vielen Seiten Unterstützung erhalten. Allen voran möchte ich mich hiermit bei meinen Betreuern Dr. Helmar Wiltsche und Prof. Günter Knapp bedanken. Vor allem Dr. Wiltsches Bereitschaft mich jederzeit tatkräftig zu unterstützen und für Fragen bereit zu stehen, ist es zu verdanken, dass diese Dissertation entstanden ist und ich die Zeit am Analytischen Institut der TU Graz genossen habe. Auch Prof. Knapps Hilfe und Bereitwilligkeit seine Erfahrungen zu teilen waren von unschätzbarem Wert.

Mein Dank geht auch an alle Mitglieder des Instituts für Analytische Chemie und Lebensmittelchemie, mit denen ich nicht nur interessante Fachgespräche führen konnte. Der freundliche Umgang und die Hilfsbereitschaft die jeder von ihnen an den Tag legte erleichterte den Arbeitsalltag und führte zu Freundschaften, die ich sehr schätze.
Ein besonderer Dank geht hiermit auch an meine Bürokollegen, die mich aufbauten, wenn etwas schief ging und sich mit mir freuten, wenn Versuche funktionierten. Ihre Freundschaft und Unterstützung bedeuten mir viel.

Zuletzt geht mein Dank an meine Familie, auf deren Rückhalt, Rat und bedingungslose Unterstützung ich mich jederzeit verlassen konnte.

Abschließend bedanke ich mich bei allen, die mich während meines Studiums unterstützt haben und welche hier nicht erwähnt wurden. Jeder einzelne von ihnen hätte es verdient genannt zu werden.

Abstract

The aim of this work was to develop and evaluate an underwater laser ablation system and couple it with a likewise newly developed high-pressure microwave flow digestion setup. A Nd:YAG laser (266 nm, 5ns, 30 mJ) was used to ablate various brass certified reference materials (BAM 223, 224, 229), which were embedded in a water body in a specially designed laser cell. Elemental fractionation can partially be avoided by using water as a carrier medium and adding a digestion step before measurement with ICP-MS. The setup works well for the ratio of the bulk elements Cu and Zn (highest mean deviation 6 %), but not so much for trace elements (mean deviations Cu/Pb of almost 50 %). An already existing flow digestion setup has been improved by changing the reactor shape. Additionally, a newly developed reactor with an inner conductor in analogy to a coaxial cable showed poor analytical performance, but provided important insight into the dependency of the microwave energy absorption to the sample conductivity and digestion tube arrangement. Because of problems with trace elements with the underwater laser ablation and general inefficient digestion properties of the coaxial reactor, the two systems were never coupled in the end.

Zusammenfassung

Ziel dieser Arbeit war es ein Unterwasser-Laser-Ablations-System zu entwickeln und zu testen. Weiters sollte es mit einem ebenfalls neu-entwickeltem Hochdruck-Mikrowellen-Durchflussaufschluss-Aufbau gekoppelt werden. Ein Nd:YAG Laser (266 nm, 5 ns, 30 mJ) wurde verwendet um verschiedene Messing-Standard-Referenz-Materialien (BAM 223, 224, 229) zu ablatieren, welche in einer speziellen Laserzelle in Wasser eingebettet wurden. Eine Fraktionierung von Elementen konnte teilweise verhindert werden, indem Wasser als Transportmedium verwendet und ein Aufschluss vor der Messung mittels ICP-MS durchgeführt wurde. Das System funktioniert für das Verhältnis der Mengenelemente Cu und Zn (höchste mittlere Standardabweichung 6 %), allerdings nicht für Spurenelemente (mittlere Standardabweichung Cu/Pb fast 50 %). Ein bereits bestehendes Durchfluss-Aufschluss-System wurde durch eine Änderung der Reaktorform verbessert. Zusätzlich wurde ein weiterer Reaktor mit einem Innenleiter anhand des Beispiels eines Koaxialkabels entwickelt. Dieser Reaktor zeigte eine nicht-zufriedenstellende analytische Leistung, führte aber zu der wichtigen Erkenntnis über die Abhängigkeit der Absorption der Mikrowellenenergie zu der Leitfähigkeit der Probe und der Anordnung des Aufschlussschlauches. Aufgrund der Spurenelement-Probleme der Unterwasser-Laser-Ablation und der generell unzulänglichen Aufschlussleistung des Koaxial-Aufbaus wurden die beiden Systeme nie miteinander verbunden.

CONTENTS

1 Underwater Laser Ablation

In the last 20-30 years nanosecond laser ablation has ascended as one of *the* methods for the analysis of solid samples. However, some materials proved to be difficult to measure with the established setups. Therefore, Luca Alberto Flamigni proposed the theory of an underwater laser ablation in 2014 to enable the examination of these samples. The aim of this thesis war to confirm his results, as well as to expand the number of samples and elements. But, to understand possible advantages of an underwater laser ablation, one must understand the processes undergoing with the common laser ablation, which are described in the chapters below.

1.1 Introduction and theoretical background

1.1.1 Common Laser Ablation

Laser ablation (LA), especially coupled with an ICP-MS, is a method with rising popularity for the last 30 years, regarding a direct solid sample analysis. Widespread applications are found in the field of geochemistry [1–3] and archaeology [4,5]. Furthermore, it is for example used in the analysis of glasses [6,7], alloys and highly alloyed steel [7–11]. Additionally, LA is used for the production of nanoparticles and for surface cleaning. Laser induced breakdown spectroscopy (LIBS) can be applied for monitoring these cleaning steps, as well as for the examination of samples, which should stay virtually untouched. This is especially important for samples like jewels or art [7,11,12].

Almost every analysis of solid samples by wet-chemical procedures requires an elaborate sample preparation step, which includes the possibility of contamination, as well as an increased amount of reagents and wastes. Laser ablation needs no, or almost no sample preparation and the medium used for the transportation of the ablated material to the ICP-MS is gas (mostly helium or argon). This reduces also the required amount of sample in comparison to a conventional liquid nebulization sample introduction. Depending on the laser used and its settings, a space-resolved determination of trace elements is possible, due to low limits of detection [13,14].

Stages of a LA and Fractionation

As this work concentrates on ns-LA of alloys and the possible overcoming of its drawbacks, the following chapters are dedicated mostly on nanosecond lasers.

The biggest problem regarding ns-LA is a possible elemental fractionation. This can happen during the initial ablation process, the transportation of the particles/aerosol and, if it is coupled with an ICP-system, also during the ionization [15].

There are a lot of factors influencing the results of a LA, including the laser used, the wavelength, the energy, the repetition rate and the carrier gas, to name just a few [9,10,13,16–18]. Kuhn and Günther [17] for example show, that the fractionation of brass is more pronounced, if argon is used as a medium, instead of helium. For other samples however an independence of the gasses was reported [19,20], whereas some authors describe that helium allows a better expansion of the aerosol plume and therefore a smaller particle size distribution [21,22].

The lasers most commonly used are Nd:YAG lasers with a fundamental wavelength of 1064 nm. They are frequency doubled, tripled, quadrupled or quintupled to provide laser light down to the deep UV. The choice of the wavelength depends strongly on the sample, as it is known, that different materials are for example ablated better with UV lasers, than one in the IR range [3]. The reason for this is the need of strong absorption of the laser light in a thin layer of the sample. If for instance the fundamental wavelength of the Nd:YAG laser is used for glass ablation, a wide distribution of coarse particles is produced. If on the other hand laser light in the deep UV is used, the particle size distribution becomes narrower and shifts towards finer particles.

During the initial step of the ns-LA the energy of the laser beam gets absorbed by the sample. This results in a heat transfer, the formation of a plasma and immediate vaporization and melting of the target [23,24].

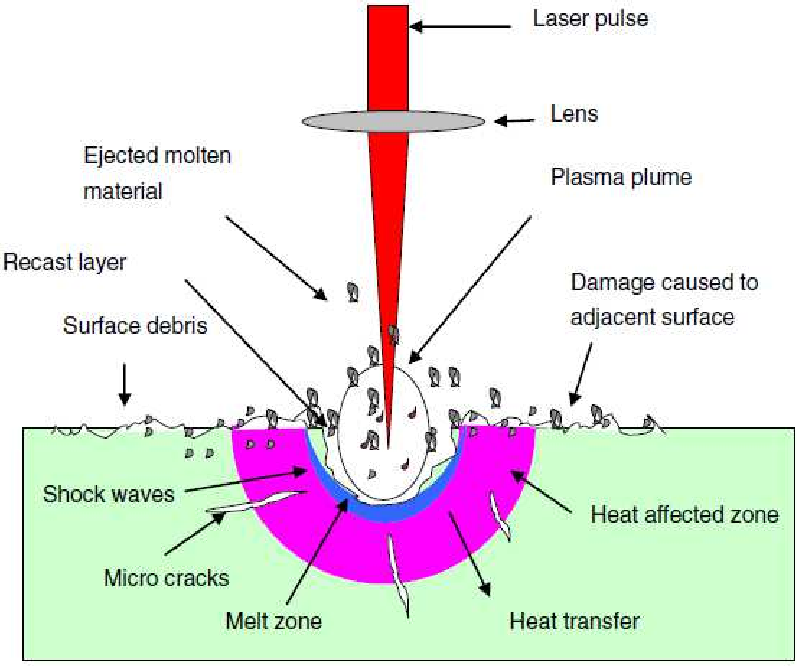

Figure 1.1: Processes of a ns-LA of a solid sample [3,23]

Figure 1.1 shows quite clearly, that the high energy of the laser beam creates heat, which doesn´t only effect the direct sample spot, but also the area around, the so-called heat-affected zone. In this heat-affected zone elements with different thermal properties can be redistributed [25]. Additionally, molten material is not only found ejected, but also remaining in and around the crater, when using ns-LA [8]. Therefore, often crater rims are created, which are higher than the sample surface. The remaining particles are also presumed to be of a different composition, then the original sample, due to depletion of volatile elements [21,26,27]. However, not all authors share this presumption [17].

Figure 1.2 shows a cross-section of craters produced by a ns and a fs laser. This illustrates clearly, that a femtosecond laser produces no, or at least less molten particles, which remain behind after the ablation. For metal samples these molten particles often appear optically as a black ring around the crater (see Figure 1.3).

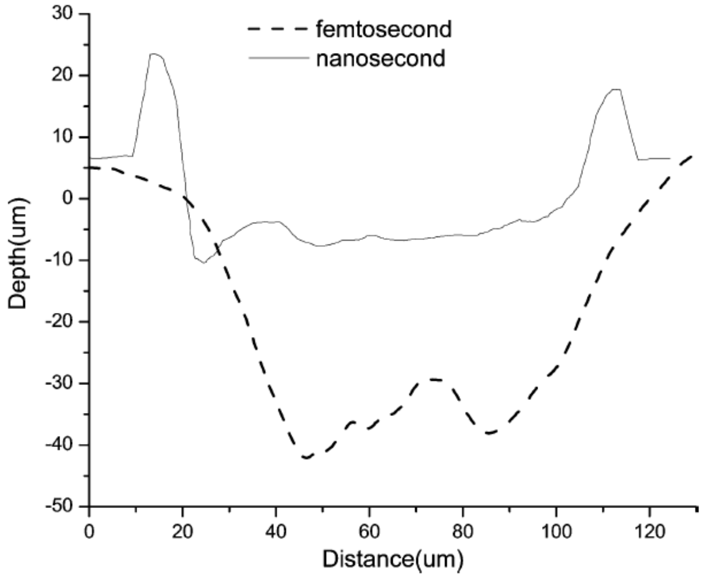

Figure 1.2: Comparison between the profiles of craters produced with a nanosecond and a femtosecond laser (50 laser shots each) [25]

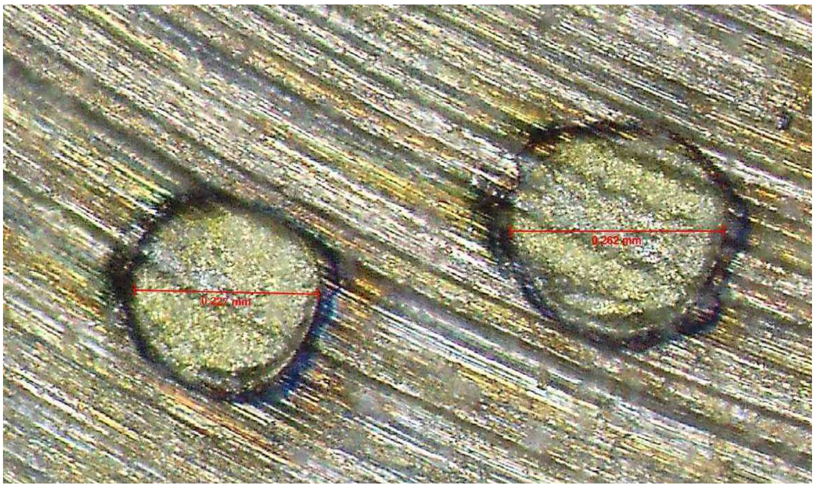

Figure 1.3: Crater produced with a Q-switched Nd:YAG laser (266 nm, 6 ns) on a brass sample

Another fractionation-point after the initial ablation is the transportation. Vaporized parts of the ablated material can condensate on cooler surfaces while being transported by the gas used, in particular on the inside of the tubes. Subsequently, the tube length should be as short as possible [13,18].

The last possible source of fractionation lies with the dissociation and ionization in the ICP. Depending on the laser and its settings, large particles may be produced during the ablation, which cannot be completely ionized in the ICP. This of course contributes to faulty measurements, as the composition of these particles are often dissimilar. Therefore, a setup which produced small particles would be preferential [28]. According to the 'zone model' from Vanhaecke [29] the composition of these particles also influences the position in the ICP, where the density of singly charged ions is maximized. This in turn has an impact on the signal intensity.

The last few paragraphs showed that a fractionation can occur at different stages of a LA measurement, especially one coupled with an ICP-MS, and that there are various factors influencing the amount of fractionation.

Reliable results are therefore dependent on solid calibration standards, which are very well matched to the matrix of the sample. Especially for environmental samples this could pose to be difficult, as the exact composition of the target is often not known [9].

Many authors report that the results obtained by fs-LA-ICP-MS match the target values better than the ns ones. Especially regarding agreement with certified values, reproducibility and consistency of the results.

Responsible for these improved outcomes are mostly two factors. Firstly, the (almost) absence of remaining molten particles at the ablation site, which was already shown in Figure 1.2. It should also be noted, that femtosecond lasers produce generally smaller particles, which results in an easier ionization in the ICP, dependent on the composition of the particles and the gas flow rates. [3,25,29–31].

Secondly, a fs-LA produces generally more signal. The reason behind this lies in the pulse duration. With nanosecond lasers this pulse duration is longer, than the quenching time of the plasma or rather the energy relaxation time of the phonons, which is around 10^{-13} s for metals. This results in an interaction of the end of the laser pulse with the plasma. Henceforth, part of the laser energy gets absorbed by the plasma, which is not the case with fs lasers. Additionally, the pulse duration of fs lasers is too short to cause severe heating of the material, which make fs-LA a nearly athermal process without any, or at least significantly reduced melting of the sample [3,18,32,33].

1.1.2 Brass

The measurement of brass has been titled as the worst case scenario regarding LA by more than one author [9,17,34]. The bulk elements Zn and Cu have very differing melting/boiling points (m.p. Cu: 1084.6 °C; b.p. Cu: 2562 °C; m.p. Zn: 419.5 °C; b.p. Zn: 907 °C) and subsequently also a different vapor pressure [13,35–37]. It is well known, that differences in the thermal properties of elements are a major factor regarding fractionation and therefore non-stochiometric sampling. These variations provoke an enrichment of elements with lower melting/boiling points in the vapor phase of the ablated material, and thereupon a possible depletion of the same elements in the molten particles. This means basically a non-homogeneously ablation of the sample [16,17].

Additionally, a fractionation can occur in the ICP, as particles above 100 nm were found to be composed of mainly copper. If these particles are not completely ionized, the determined ratios/concentrations change drastically [17].

A lot of research has been done on what parameters influence the elemental fractionation. Starting with the type of laser (Nd:YAG, KrF, XeCl, ArF,…), wavelength, pulse duration, gas and energy densities [9,10,17,38,39].

It is also noted, that a pulse energy far above the ablation threshold value of a specific laser results in more steady signals, regarding the Cu/Zn ratio. If the energy is lower or in the same range as the threshold value, the material gets more heated, instead of ablated. For example the ablation threshold value for a Nd:YAG laser (266 nm, 6ns) is around 1.8 $\mathrm{J\,m^{-2}}$ [17].

Additionally to the laser, its wavelength, pulse duration and so on, it has been stated, that also the composition of the target material has a big influence on the amount of fractionation [9,40]. This often leads to a non-linear calibration when comparing brass samples with a different composition. Borisov et al. [9] shows that the total amount of ablated mass increases with an increasing Zn concentration. This of course influences the element ratios, considering the fractionations, and could therefore be an explanation of the non-linear behaviour of Cu and Zn.

Gagean [10] shows, that not only the composition of a material influences the fractionation, but additionally the thermal treatment of the sample, such as annealing.

In order to enable the use of ns-LA for brass and similar samples, a lot of effort has been put in to find ways to overcome the fractionation problems. One suggestion is to use Cu as some kind of internal standard. [9]. The collecting of the ablated particles/vapor on filters, with a following digestion with 3 % nitric acid doesn´t produce values corresponding with the certified one, as fractionation occurring during the ablation process are not prevented [17].

Furthermore, the usage of a fs laser is proposed. These have generally improved results regarding fractionation, as the sample doesn´t undergo drastic structural changes. However, even with a femtosecond laser not all fractionations can be prevented. Colao et a. [11] show, that even with 250 fs laser pulses an increased evaporation of Zn takes place, but the effect is significantly reduced than with a ns laser.

1.1.3 Underwater Laser Ablation

The aim of this thesis is based on a theory of Luca Alberto Flamigni, which he presented in his doctoral thesis in the year 2014 [14]. He thought, that one could eradicate all, or at least some of the flaws of a nanosecond laser ablation, by ablating a sample underwater.

Fractionation occurring with the ns-LA are already mentioned in the chapters above. In these chapters it is also discussed, that the usage of a femtosecond laser could counter some of the problems, but not all of them. Furthermore, a femtosecond laser is significantly more expensive, so it would be of interest to find a way to use the cheaper, and easier to operate, nanosecond laser, without fearing the drawbacks.

The main problem when using ns-LA is the occurrence of fractionation, which is for instance partially depending on the sample. Especially the analysis of metallurgic samples is difficult, because of increased appearance of melting during the ablation process [17]. Therefore, Flamigni used brass, as a worst-case scenario, to test his theory and this is also the sample of choice in this thesis.

Underwater LA is a method, where the gas, which is usually used to transport the ablated material, is replaced by water. That means the ablation itself is also done underwater. In the following paragraphs each of the possible fractionations of the common laser ablation are addressed and the theoretical advantages of an underwater LA are discussed.

As already discussed in chapter 1.1.1 a fractionation can appear during the ablation process, which results in a non-stoichiometric distribution of the elements in the ablated/volatilized material, as well as in the molten part of the sample.

Underwater LA in a bigger relation is actually nothing new. Especially in the last few years it is already used as a method to create nanoparticles. Which means, that there are already some insights on the laser ablation process in liquids.

It is known that even in liquids a plasma with temperatures between 6000 and 10000 K is produced during an ablation. This results in a shockwave and the creation of a cavitation bubble with the extracted atoms inside. The bubble expands/fluctuates further, till is collapses and the particles are released into the surrounding liquid. The collapsing of the bubble creates a pressure higher than 10^7 Pa [41,42]. This pressure in combination with the resulting shockwave should, in theory, expel all ablated material into the liquid medium, even possible molten parts of the sample and thus resulting in a clean ablation spot.

Tamura et al. [43] used a laser induced breakdown spectroscopy (LIBS) setup for shadowgraph imaging of the ablation process. These images show not only the bubble, but also a shadow, which was assumed to be caused by the created shockwave. This assumption was supported by the fact, that the shadow expanded with about 2000 m s^{-1}. This speed is similar to the that of sound underwater (around 1500 m s^{-1}).

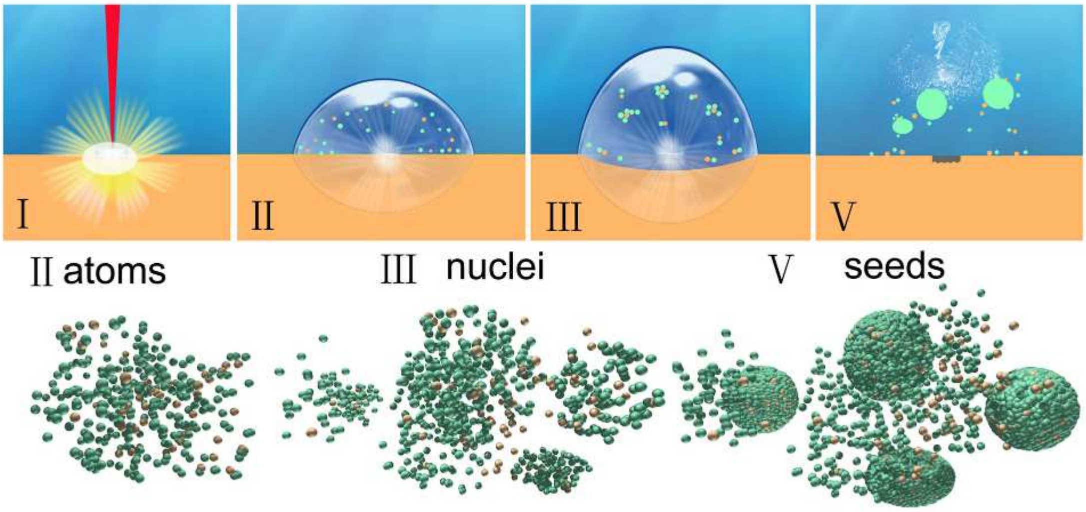

Figure 1.4: Processes of an underwater laser ablation, I) Plasma generation, II) formation of a bubble and dispersed atoms, III) expansion of the bubble and growing of particles, V) collapsing of the bubble and releasing the particles into the liquid [44]

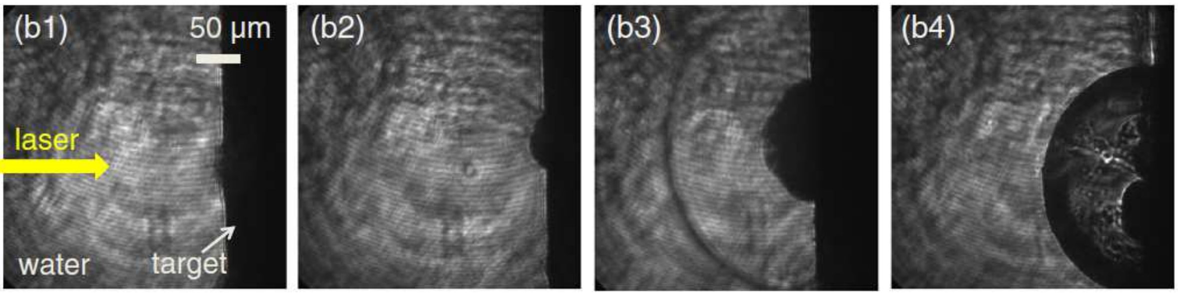

Figure 1.5: Shadowgraph images of a 150 ns laser pulse underwater [45]

If a LA is performed with water and not a gaseous medium, it doesn´t change the fact, that the longer pulses of a nanosecond laser creates craters with a smaller volume, than for example a femtosecond laser. The laser pulses are too long, so that part of the energy gets absorbed by the already created plasma and not by the sample surface [45].

The second possibility of a fractionation in the common LA is during the transport to the ICP-system. Heavy particles may sediment and volatile parts of the ablated material can condensate on the cooler tubes. With underwater LA the transport medium is water, which has a significantly higher viscosity than either of the gasses used normally. This should prevent any sedimentation and also the transport of the volatile parts should be guaranteed in the form of solutes or even solid particles [14].

Lastly, in the common LA many authors have described a fractionation occurring in the ICP, because of incomplete ionization of larger particles. The solution for this problem for Flamigni, as well as in this thesis, was the addition of a digestion step with nitric acid before the actual measurement. Therefore, no particles remained and no fractionation can occur.

Although Flamigni has shown very promising results in his thesis, only one sample has been investigated. The aim of this thesis is therefore an examination of further samples, especially standard reference materials, as well as the analysis of more elements, than just Cu and Zn.

1.2 Experimental

1.2.1 Instrumentation

Laser system

In this work the laser system LUV266 of the company New Wave Research was used. It is a Q-switched Nd:YAG laser (266 nm, 5 ns, 30 mJ) with two frequency multiplication crystals.

Figure 1.6: Nanosecond laser ablation system, 266 nm

Laser ablation cell and glass

In order to operate the laser ablation system underwater, a cavity needed to be constructed, where it was possible to apply a continuous water flow. The sample was also ground so that the surface was at the same height as the water in- and outlet, to optimize the transportation of the ablated particles. The sample, as well as the cover glass were pressed by O-rings and aluminium plates and therefore easily changeable.

At the same time the laser cell needed to be as small as possible. Not only was the available space in the laser cavity limited, but also the waterbody needed to be minimised to avoid further dilution.

To prevent a possible contamination of the water, the material used for this laser ablation cell was PEEK. Figure 1.7 and Figure 1.8 show a cross section of the final laser cell, as well as the actual appearance respectively.

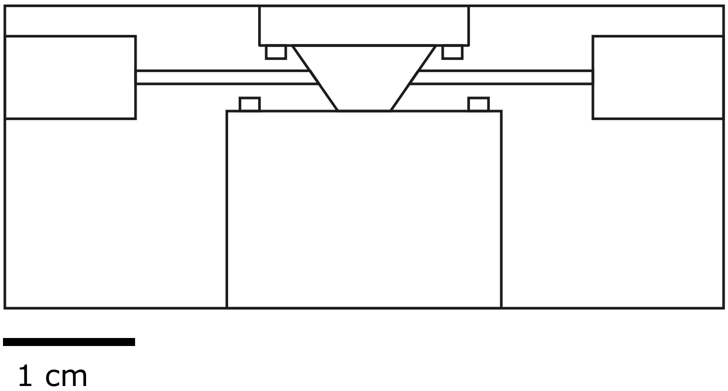

Figure 1.7: Cross section of the underwater laser ablation cell with water in- and outlet

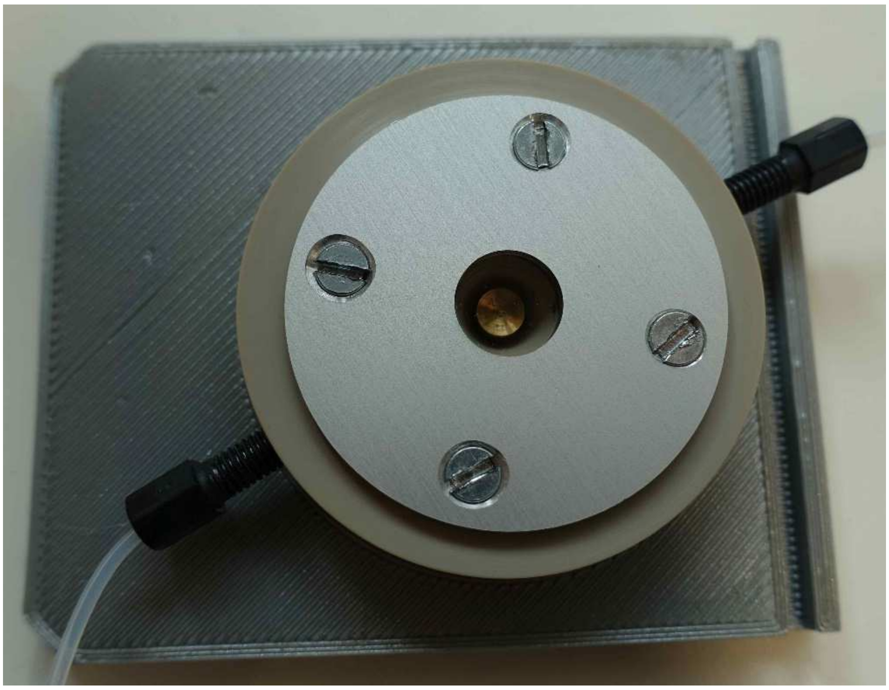

Figure 1.8: PEEK laser cell with sample, cover glass and tubes

The final laser cell had a height of 2.05 cm (including the aluminium cover plate) and a diameter of 5.50 cm. The inside of the cell contained approximately 400 µL water.

During the first stages of the project sapphire, as well as quartz were used as cover glasses. Both had a diameter of 15 mm and a thickness of 2 mm. Because of recurring damaging of the glasses, which is explained further along in this chapter, only quartz glass was used in the final experiments.

Samples and Standards

In the common laser ablation, a lot of problems occur when metallurgic samples are used, which consist of elements with very different melting/boiling points (see chapter 1.1.2). Therefore, in this work a solid brass sample was used, as well as three different copper-alloy Standard Reference Materials (BAM 223, BAM 224, BAM 229). The bulk of these samples consisted of copper and zinc. In this work only the ratio between copper and zinc, as well as copper and lead for the samples BAM 223 and BAM 224 were of interest.

The actual ratio of the solid brass sample was determined by using a microwave assisted digestion with the Multiwave 3000 (Anton Paar, Graz, Austria) and the measurement with ICP-MS and ICP-OES.

In the beginning the flat solid brass sample was just pressed to the underside of the cone in the laser cell, which was filled with water. However, that was changed quickly. Because of problems with the camera focus the sample needed to be higher up and therefore also closer to the laser. This resulted in a change of the sample shape, with the final form shown in Figure 1.9.

Figure 1.9: Solid brass sample

The final shape of the brass sample had an upper diameter of 5.1 mm (surface available for ablation) and a diameter of 18 mm at the bottom. At the top the sample was formed like a trapezoid to enable a better pressing and therefore sealing of the laser cell. This is also the shape that the standard reference materials had to be. As they came in the form of chips this wasn´t as easy as cutting and polishing them into the right shape.

With the silicon rubber Elastosil® M 4370 (Wacker Chemie AG, München, Germany), a negative-form of the solid brass sample was produced (Figure 1.10). This silicon rubber form was further filled with the epoxy EPO-TEK® 301 (Epoxy Technology, Massachusetts, USA) and the standard reference material chips. After drying the epoxy as the producer recommends, the samples were ground and polished, using the machine LaboPol-25 (Struers GmbH, Willich, Germany) with the waterproof silicon carbon paper FEPA#320 and FEPA#1200 were used. The final form of the standard reference materials is shown exemplarily in Figure 1.11.

Figure 1.10: Negative silicon rubber form of the solid brass sample

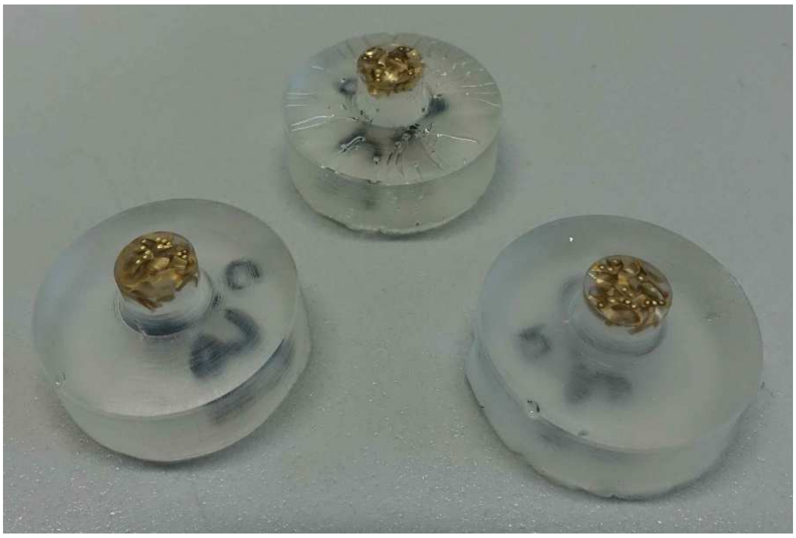

Figure 1.11: Epoxy form with the embedded standard reference material chips of the sample BAM 229

In this thesis only the ratio between elements were of interest, which were determined by a measurement with ICP-MS and ICP-OES. For a liquid calibration the following reagents were used: purified water (18 MΩ cm, Barnstead Nanopure, Thermo Fisher Scientific, USA); nitric acid (69 %, purified by subboiling); single elements stock solutions of Cu, Zn, Pb, Sc (1 g L^{-1}, in 2 % HNO_3, Roth, Germany); single stock solution of Ge (1 g L^{-1}, in H_2O, SCP Science, USA). Sc was used as an internal standard for the ICP-OES and Ge for the ICP-MS measurements.

1.3 Method development

During the first stages of this project a few problems were encountered. There seems to be a loss of energy due to absorption in the water, even if 266 nm is almost at the lowest point of the absorption spectra of liquid water. This leads at least optically to ablation craters with a lower depth, than compared to a common LA.

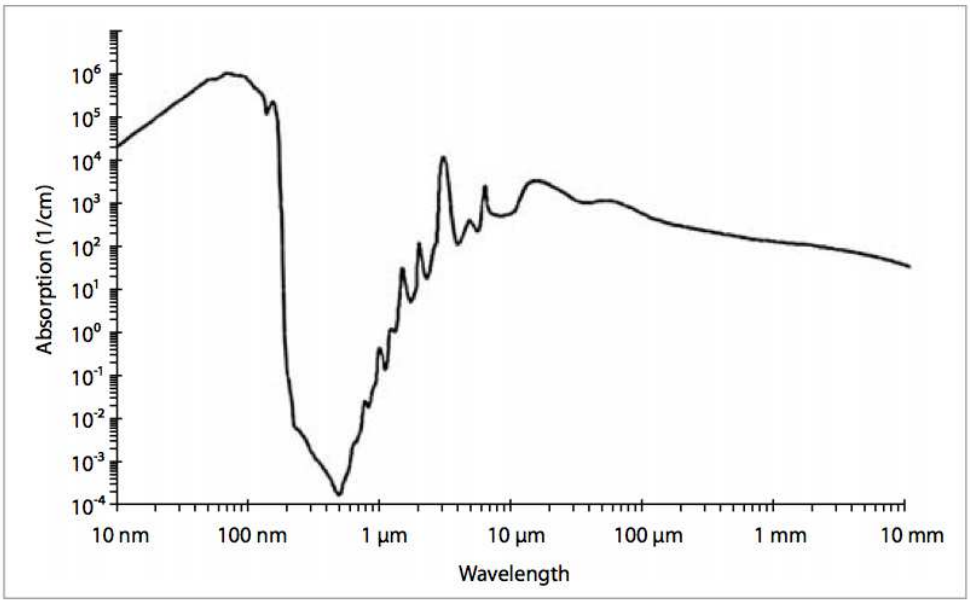

Figure 1.12: Absorption spectra of liquid water [46]

Defocusing

Another problem which was encountered during the whole project, was the need to intentionally set the focus point of the laser beam off the sample surface, when operating underwater. The actual ablation zone differs from the focus point, when using the camera of the laser ablation system. This is due to a different light refraction of water.

Experiments showed that when focussing the camera on the surface, the real ablation point lies above the sample. This resulted not only in very small, or no crater at all, but also in recurring damaging of the cover glass, regardless of the material of the same. Throughout the developing steps the sapphire glass was generally more damaged than the quartz glass. Therefore, in the later stages of the project, quartz glass was used exclusively.

Figure 1.13: Damaged sapphire cover glass

To avoid constantly damaging the cover glass and get actual craters on the surface of the sample, the right amount of defocusing 'into' the sample needed to be worked out. This defocusing step had to be evaluated every time the design of the laser cell, or the shape of the sample was changed, as this resulted in a different level of water between the sample and the cover glass.

Figure 1.14 shows exemplarily one of these defocusing evaluations. The right amount of defocusing was determined as a combination of whether the cover glass was damaged, the crater diameter and the general appearance of the crater.

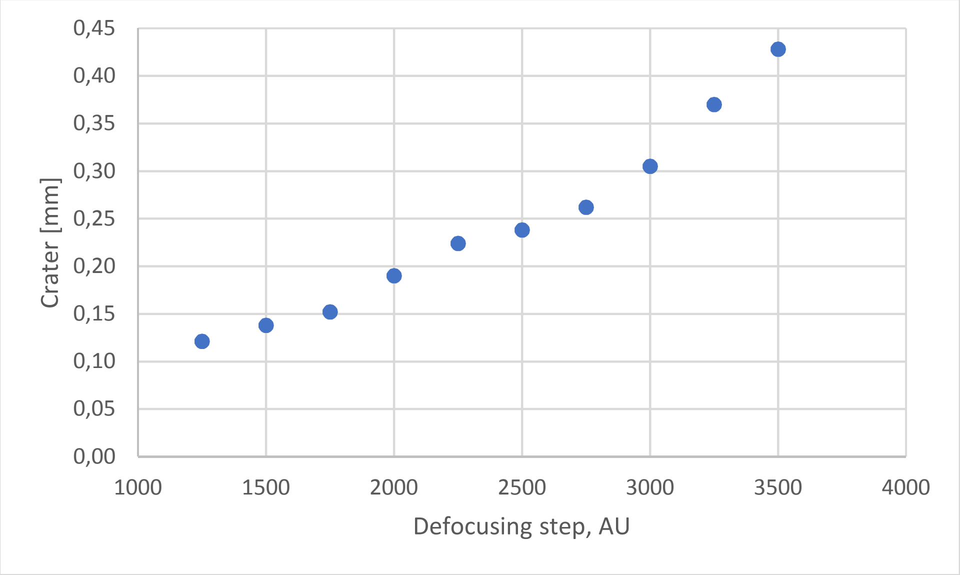

Figure 1.14: Example of a defocusing experiment with the solid brass sample

Figure 1.15: Defocusing experiment, solid brass sample

After the fixation on the final shape of the samples and the laser cell, a defocusing step of 2500 was used for the solid brass sample, which equals ~2.5 mm. This was later changed for the standard reference materials to 3500 (~3.5 mm), because of infrequent damaging of the cover glass with the lower defocusing step.

Surface cleaning

The earliest experiments showed a poor reproducibility of the results, concerning the crater diameter, the amount of ablated material, as well as differing ratios between the elements. As it was assumed that this was caused by either oxidation of the surface or just contamination, a cleaning step was included. While putting the sample in an ultrasonic bath after every ablation appeared to be very effective, it was also quite time consuming, as the laser cell needed to be dismantled every time.

In the end the cleaning of the surface was done by 60 laser shots without collecting the water, followed by the actual ablation on the same spot.

Digestion

To enable the use of a liquid calibration and in order to receive continuous signals without spikes, a digestion step between the ablation and the measurement was included. Brass is a sample, which is easily digested with nitric acid. Therefore, the digestion step consisted of adding 200 µL nitric acid (69 %) and putting the solution into a drying cabinet at 60 °C for 15 minutes.

A transient measurement with 600 replicates showed that the whole sample was digested and no larger particles remained (Figure 1.16). This digestion also results in a reduction of spikes, due to the absent of large particles.

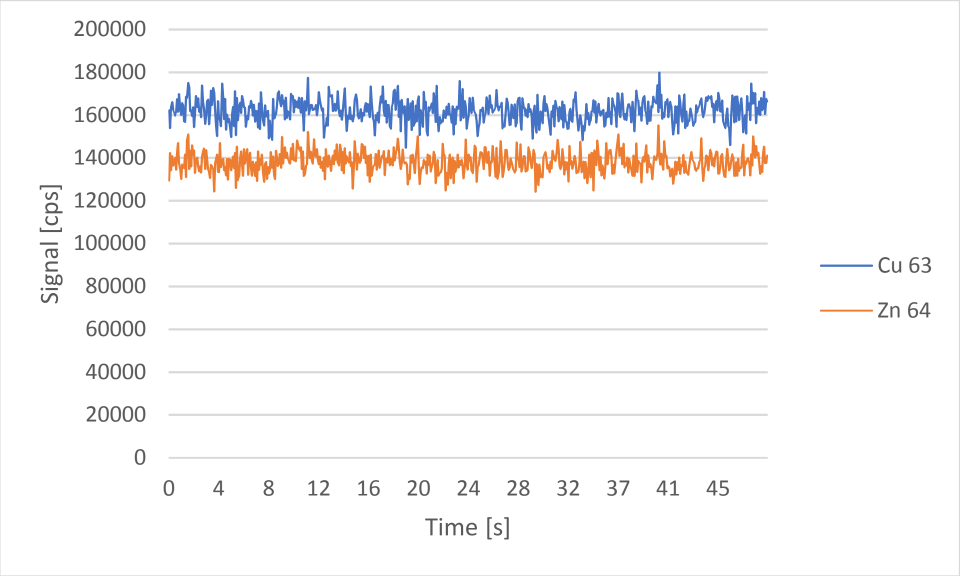

Figure 1.16: ICP-MS transient measurement to prove the efficiency of the digestion

The digestion step equalizes the results of the underwater ns-LA to that of a common fs-LA regarding the consistency of the signals. For a comparison of a ns-LA and a fs-LA with both methods using gas as a medium see Figure 1.17.

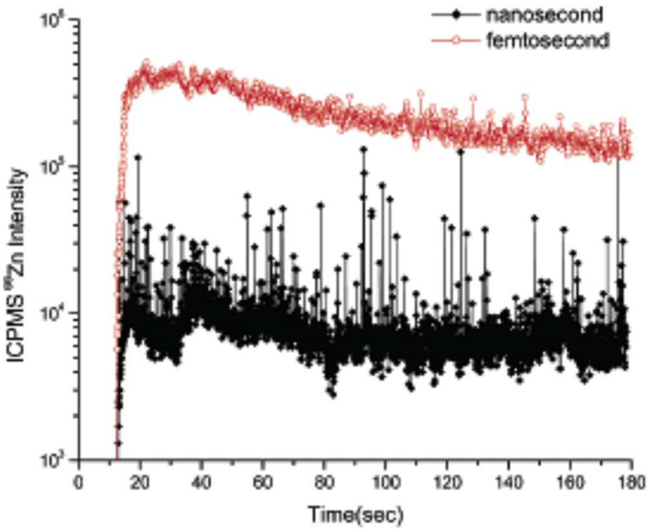

Figure 1.17: Comparison of the ICP-MS signals of ^{66}Zn, produced with a Nd:YAG laser (6 ns, 266 nm) and a Ti:sapphire laser (150 fs, 266 nm) [25]

1.4 Results and discussion

In this work only the ratio between elements is observed. As all samples are copper alloys it is mainly the ratio between copper and zinc, which will be described as Cu/Zn. To simplify the presentation of the results the Cu/Zn ratio will be shown for example as 1.50, which means the concentration of copper is 1.50 times the concentration of zinc. It can also be read as 1.50 : 1 (Cu : Zn). The same goes for the ratio of Cu/Pb.

The concentrations which will be shown in the following chapters are those of the ablated and digested material, diluted to an end volume of 10 mL. Scandium was used as internal standard with the ICP-OES, Ge was the choice for the ICP-MS. The concentrations are mainly featured to highlight the considerable differences in the amount of the ablated sample. It is important to note that by performing underwater LA the sample is considerably diluted when compared with classical LA. This results in a proportional loss in sensitivity of the method.

Laser ablation is commonly used in combination with an ICP-MS measurement. With the used laser settings, the concentrations of the investigated elements (with the exception of lead) are high enough to enable an analysis with an ICP-OES. Therefore, a comparison between these measurement methods is possible.

Furthermore, the approximate diameters of the craters will be shown. These were determined manually by means of a photo of the sample, created with the digital camera microscope DigiMicro Profi (dnt). However, this is only an approximation of the actual crater dimensions.

1.4.1 Standard reference materials

1.4.1.1 Concentration and ratio

As already mentioned, a comparison between an ICP-MS and an ICP-OES measurement of the ablated samples was done, especially for the standard reference materials. However, the results of these measurements proved to be very different. As the measured samples were taken out of the exact same tubes, an error in the sample preparation could be excluded.

To show the discrepancy between the two measurements, the concentration and ratio will be shown for both methods exemplarily for the sample BAM 229. Because of reasons, which will be explained in regard to the results of that sample, only the ICP-MS measurement will be presented for the other two standard reference materials.

Table 1.1: Laser settings for the measurement of the standard reference materials

Wavelength	266 nm
Frequency	10 Hz
Set crater diameter	300 µm (calibrated on air)
Quartz glass	15.0 mm diameter 2 mm thickness
Ablation sequence	60 laser shots (cleaning) 200 laser shots (actual ablation)
Defocusing	3.5 mm (‘into’ the sample)

ICP-OES: CIROS Vision EOP, Spectro Analytical Instruments Inc., Kleve, Germany

Table 1.2:ICP-OES settings; Gas: Argon 5.0

Plasma Power	1350 W
Coolant Flow	12.50 L min^{-1}
Auxiliary Flow	0.60 L min^{-1}
Nebulizer Flow	0.83 L min^{-1}
Cu	324.754 nm
Zn	213.856 nm
Sc	361.384 nm

ICP-MS:

- Elan DRC+, cyclon-spraychamber, Perkin Elmer, Massachusetts, USA
- Elan DRC-e, scott-spraychamber, Perkin Elmer, Massachusetts, USA

Table 1.3: ICP-MS settings; Gas: Argon 5.0

Plasma Power	1350 W
Coolant Flow	15.00 L min^{-1}
Auxiliary Flow	1.20 L min^{-1}
Nebulizer Flow	1.00 L min^{-1}
Oxide rate	< 3 %
Doubly charged rate	< 3 %
Cu isotope	63
Zn isotope	64
Pb isotope	208
Ge isotope	74

BAM 229

Table 1.4: Concentrations and ratios of the sample BAM 229; comparison of ICP-MS and ICP-OES

	ICP-MS			**ICP-OES**		
Shot position	Cu [µg L^{-1}]	Zn [µg L^{-1}]	Cu/Zn	Cu [µg L^{-1}]	Zn [µg L^{-1}]	Cu/Zn
1	85.9	48.1	1.79	86.0	57.0	1.51
2	79.2	45.0	1.76	83.0	57.0	1.46
3	187	102	1.83	189	121	1.56
4	72.0	39.5	1.82	74.0	49.0	1.51
5	60.2	34.7	1.74	60.0	42.0	1.43
6	53.4	30.1	1.78	55.0	38.0	1.45
7	50.4	27.0	1.87	55.0	36.0	1.53
8	85.1	43.2	1.97	91.0	56.0	1.63
9	69.5	39.8	1.75	67.0	46.0	1.46
10	71.3	37.0	1.93	74.0	47.0	1.57
11	61.6	33.0	1.87	62.0	40.0	1.55
12	77.6	42.6	1.82	77.0	51.0	1.51
13	127	71.5	1.77	133	88.0	1.51
14	142	79.5	1.79	133	89.0	1.49
			1.82 ± 0.07			1.51 ± 0.05

In Table 1.4 it is easy to see that the amount of ablated material differs quite a lot at the various shot positions. During the preparation of the epoxy sample, the surface was ground and polished, so there should be no height differences. Additionally, every shot position was 'cleaned' before the actual ablation by 60 laser shots on the same spot. Therefore, also an oxidation and contamination of the surface can be excluded. Pre-measurements showed that there are no fluctuations of the laser energy, which would result in craters with different depths. Therefore, no definite reason could be found for the great differences in the concentrations. Especially, as the crater diameters are approximately in the same range, as will be shown later.
As a matter of fact, other authors reported the same occurrence of ablating different amounts of the same sample, even if the ablation conditions doesn´t change. This is shown in Figure 1.18.

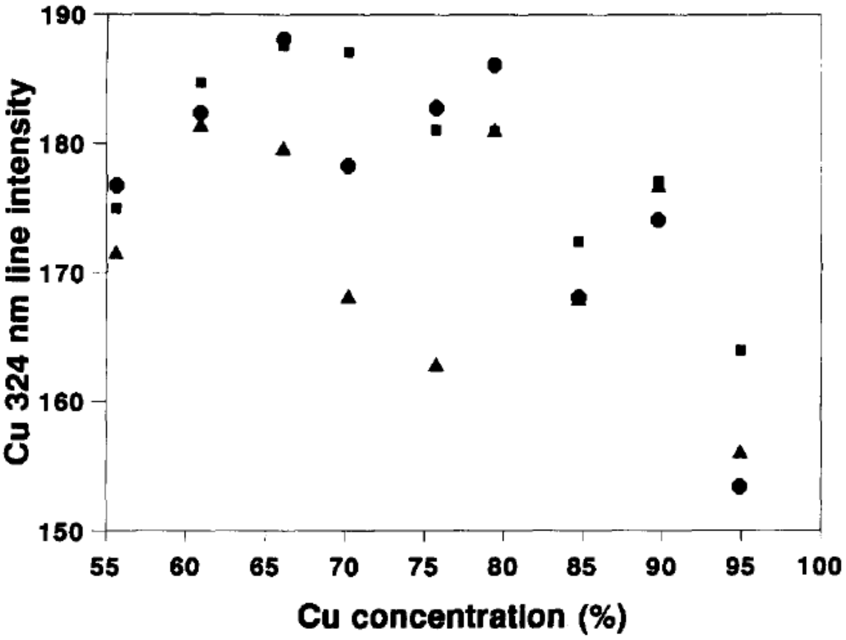

Figure 1.18: Cu signals of three ICP-OES measurements, Nd:YAG laser (266 nm, 10 mJ, 10 Hz), sample was polished between experiments

Table 1.4 also highlights the very different results regarding the Cu/Zn ratio, comparing the ICP-MS and ICP-OES measurements. As already mentioned, the measurements were done out of the same tubes, so there is no possibility of differences in the sample preparation.
Obviously, the copper concentrations are quite alike, with a mean deviation of 3.4 % and maximum deviation of 8.4 % between the two methods. This leads to the

assumption, that there is some kind of problem with the measurement of zinc. The comparison of the zinc concentrations shows a mean deviation of 18.3 % and a maximum deviation of 25.0 %.

The concentrations are high enough to be easily measured by either method and no obvious interferences could be found.

To prove, which method provides reliable results the original standard reference material chips were prepared and measured, to compare these results with the certified values. For the sample preparation a microwave assisted digestion with a mixture of nitric acid and water was done with the Multiwave 3000 (Anton Paar, Graz, Austria).

Temperature program: 1200 W (Ramp 20:00 min; Hold 15:00 min), 0.5 bar s^{-1}, IR temperature limit: 210 °C, pressure limit: 40 bar

After an appropriate dilution the digested samples were again measured with both methods. The results, as well as the certified values are shown in Table 1.5.

Table 1.5: Certified and measured Cu/Zn ratio of the standard reference material BAM 229 (mean value ± standard deviation, n=14)

BAM 229	**Cu [%]**	**Zn [%]**	**Cu/Zn**
certified	63.334 ± 0.007	36.63 ± 0.04	1.73
ICP-MS			1.72 ± 0.01
ICP-OES			1.66 ± 0.02

It is easy to see, that the ratio found with the ICP-MS measurement matches the certified ratio quite well. That leads to the conclusion that the problem with the determination of zinc lies with the ICP-OES measurement. For an unknown reason the zinc concentration with this method is obviously overestimated. Spectral interferences on the Zn(I) 213.856 nm emission line were not found to be the reason for these results. Admittedly, the difference between the ICP-OES ratio and the certified one isn´t as high as the difference between the ratio of the ablated samples and the certified one. Nevertheless, because of these results, only the ICP-MS measurement will be regarded.

The determined ICP-MS Cu/Zn ratio of the ablated sample (Table 1.4) is 1.82 ± 0.07. This means a mean difference of 5.2 % in regard to the certified ratio.

BAM 223

Table 1.6: Concentrations and ratios of the sample BAM 223 (mean value ± standard deviation, n=12)

Shot position	**Cu [µg L^{-1}]**	**Zn [µg L^{-1}]**	**Pb [µg L^{-1}]**	**Cu/Zn**	**Cu/Pb**
1	120	74.5	6.34	1.61	19.0
2	71.3	45.4	4.10	1.57	17.4
3	82.8	51.7	7.52	1.60	11.0
4	99.0	61.3	10.3	1.61	9.65
5	144	93.3	11.7	1.55	12.4
6	75.7	47.3	6.09	1.60	12.4
7	49.5	32.5	8.35	1.52	5.93
8	147	94.6	9.26	1.55	15.9
9	167	105	9.90	1.59	16.9
10	110	70.1	6.76	1.57	16.3
11	96.1	59.9	6.32	1.61	15.2
12	276	177	11.1	1.56	24.9
				1.58 ± 0.03	14.8 ± 4.9

Table 1.7: Certified concentrations and ratios of the sample BAM 223

BAM 223	**Cu [%]**	**Zn [%]**	**Pb [%]**	**Cu/Zn**	**Cu/Pb**
certified	58.74 ± 0.02	38.82 ± 0.09	2.13 ± 0.02	1.51	27.6

BAM 224

Table 1.8: Concentrations and ratios of the sample BAM 224 (mean value ± standard deviation, n=16)

Shot position	**Cu [µg L^{-1}]**	**Zn [µg L^{-1}]**	**Pb [µg L^{-1}]**	**Cu/Zn**	**Cu/Pb**
1	243	161	7.39	1.51	32.9
2	222	147	7.28	1.51	30.5
3	77.9	50.7	4.36	1.54	17.9
4	149	102	4.58	1.47	32.6
5	65.2	41.7	4.02	1.56	16.2
6	57.3	36.5	2.99	1.57	19.2
7	71.8	46.5	5.66	1.54	12.7
8	71.0	46.4	4.65	1.53	15.3
9	145	94.4	5.26	1.54	27.6
10	83.8	53.0	3.85	1.58	21.8
11	67.5	45.6	5.56	1.48	12.1
12	54.7	33.3	1.43	1.64	38.3
13	80.6	51.0	1.99	1.58	40.5
14	135	87.6	3.54	1.55	38.2
15	86.0	55.3	2.81	1.56	30.7
16	154	99.9	4.45	1.54	34.6
				1.54 ± 0.04	26.3 ± 9.8

Table 1.9: Certified concentrations and ratios of the sample BAM 224

BAM 224	**Cu [%]**	**Zn [%]**	**Pb [%]**	**Cu/Zn**	**Cu/Pb**
certified	57.40 ± 0.02	39.40 ± 0.04	1.13 ± 0.04	1.46	50.8

Table 1.6 and Table 1.8 show that for the samples BAM 223 and BAM 224 the amount of ablated material differs a lot, the same way as with the sample BAM 229. In comparison to that, the Cu/Zn ratios fluctuate only slightly.

Opposed to the Cu/Zn ratios, the Cu/Pb ratios differ quite wildly depending on the shot position. Not only does this result in a very high standard deviation, but the calculated ratios are far off the certified ones. It is important to note, that for all ablation spots investigated, the determined Cu/Pb ratio was smaller than the certified one. This clearly proves that a heterogeneous distribution of Pb in the sample can be excluded as a potential reason for the low findings.

Table 1.10 and Table 1.11 show a summary of the three standard reference materials with the certified and measured ratios, as well as the mean percentual deviation between those two values.

Table 1.10: Summary of the Cu/Zn ratios; BAM 223, BAM 224 and BAM 229; (mean value ± standard deviation, n=12, n=16, n=14, respectively)

	certified Cu/Zn	**measured Cu/Zn**	**mean deviation [%]**
BAM 223	1.51	1.58 ± 0.03	4.3
BAM 224	1.46	1.51 ± 0.04	6.0
BAM 229	1.73	1.82 ± 0.07	5.2

Table 1.11: Summary of the Cu/Pb ratios; BAM 223 and BAM 224; (mean value ± standard deviation, n=12, n=16, respectively)

	certified Cu/Pb	**measured Cu/Pb**	**mean deviation [%]**
BAM 223	27.6	14.8 ± 4.9	46.5
BAM 224	50.8	26.3 ± 9.8	48.2

With mean (and also maximum) deviations well under 10 % the determined Cu/Zn ratios seems to be in accordance to the certified ones. However, as all three samples yield in ratios a little bit too high, one could assume a slight underestimation of zinc.

In comparison to the relatively good results of the Cu/Zn ratios, the Cu/Pb ratios look even worse. The calculated mean Cu/Pb ratios are almost half of the certified ones.
Because of the good accordance of the measured Cu/Zn ratios with the certified values, it is apparent to suggest that the discrepancy between the Cu/Pb ratios and the certified ones originate from a faulty determination of the Pb concentration.

Assuming that the Cu concentrations were measured correctly, that means that this discrepancy comes from a highly overestimation of Pb.

These concentrations are unfortunately too low to be measured with an ICP-OES, and therefore no comparison to the results of another method is possible.

Pb and Zn, as well as a few other elements are labeled as fractionating elements, when using nanosecond LA, because of their low melting/boiling temperature [8,47]. Therefore, it is a bit astonishing to see this contrary trend of overestimating Pb, as well as at the same time underestimating Zn.

1.4.1.2 Crater diameter

As already mentioned, the crater geometry could only be determined approximately, because it was sometimes hard to define the exact crater edge.
Furthermore, the microscope used for the images couldn´t produce a magnification high enough to actually see the inside of the craters. Flamigni [14] showed that craters produced underwater have cleaner internal walls, without protrusions. Unfortunately, with the microscope used in this thesis no such pictures could be produced.

Figure 1.19 shows the approximate crater diameters of the samples BAM 223, BAM 224 and BAM 229 combined in one image. The shot positions were the same as those used for the determination of the concentrations and ratios, which are shown in the tables above this chapter.

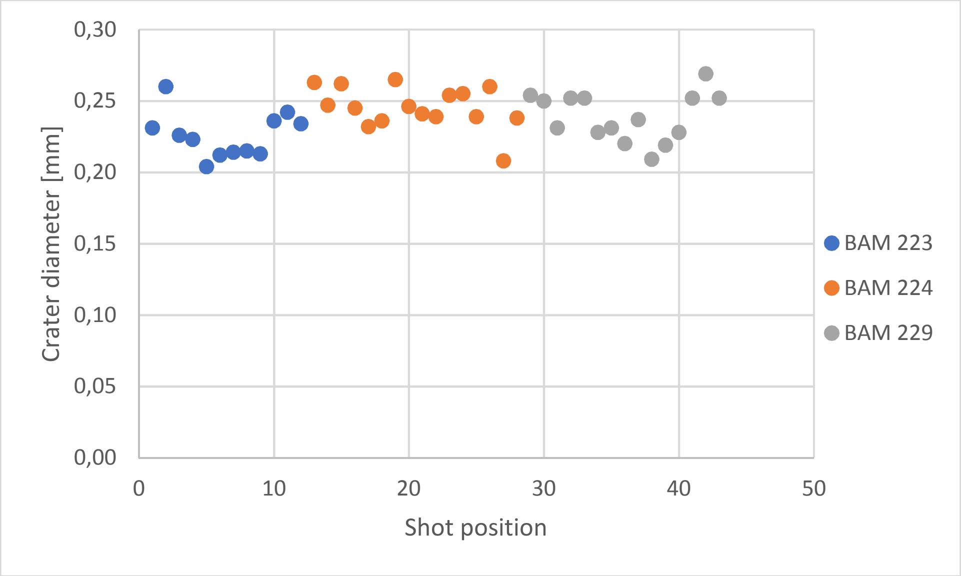

Figure 1.19: Ablation crater diameters of the samples BAM 223, BAM 224 and BAM 229

Even if this is just an approximate determination of the crater geometry, it is obviously, that even though the amount of ablated material differs quite a lot, the crater diameters are very consistent with only a fluctuation in a very small range. There is also no definite differentiation between the samples.

The figures below show an example of the determination of the crater diameters, as well as a few microscope pictures of some of the ablated samples. The crater diameters were determined on the basis of the black line (Figure 1.21), which had a known width.

Figure 1.20: microscope picture of the sample BAM 229_a

Figure 1.21: microscope picture of the sample BAM 229_a; digital determination of the crater diameters

Figure 1.22: microscope picture of the sample BAM 229_b

Figure 1.23: microscope picture of the sample BAM 223_a

Figure 1.24: microscope picture of the sample BAM 223_b

Figure 1.25: microscope picture of the sample BAM 224_a

In all the pictures above it is easy to see some kind of black ring around most of the craters. This would indicate molten particles remaining behind after the ablation and transportation of the ablated material. In chapter 1.1.2 it was indicated that the molten parts of the sample would consist mainly of Cu, which would lead to an underestimation of this element in the samples. That matches the faulty Cu/Pb ratios but definitely not the Cu/Zn ratios.

1.4.2 Solid brass sample

The solid brass sample was mostly used for the preliminary studies and the method development.

Unfortunately, the ablated samples could only be measured with an ICP-OES. The results in the previous chapters showed, that there is obviously a problem with the ICP-OES measurement. This is also proved when comparing the target ratio of the solid brass sample determined with an ICP-MS and an ICP-OES, as these vary wildly. Consequently, the calculated concentrations and ratios are discarded.

1.4.2.1 Crater diameter

The determined crater diameters shown in Figure 1.26 are significantly smaller than the ones of the standard reference materials (Figure 1.19). This difference was caused by a lower defocusing step.

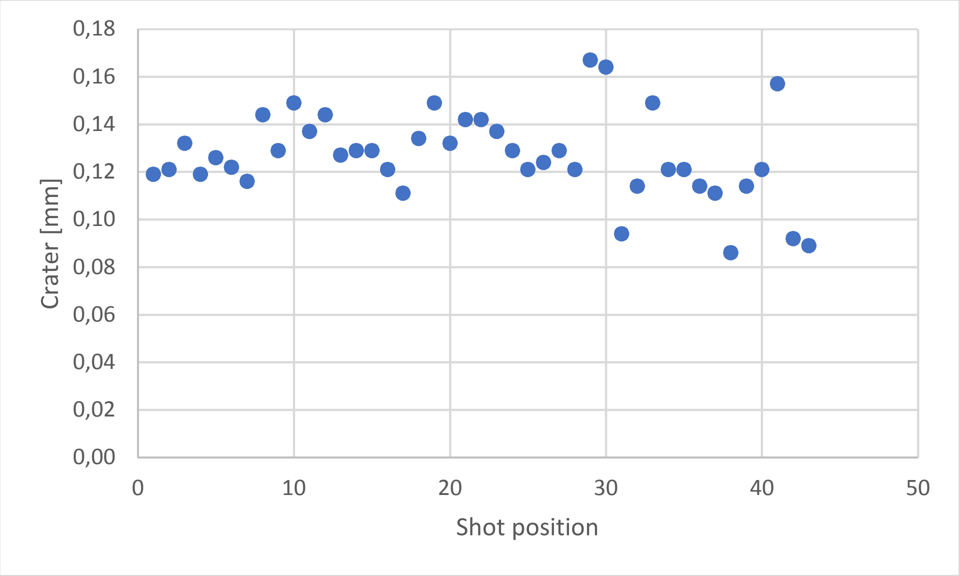

Figure 1.26: Ablation crater diameters of the solid brass sample

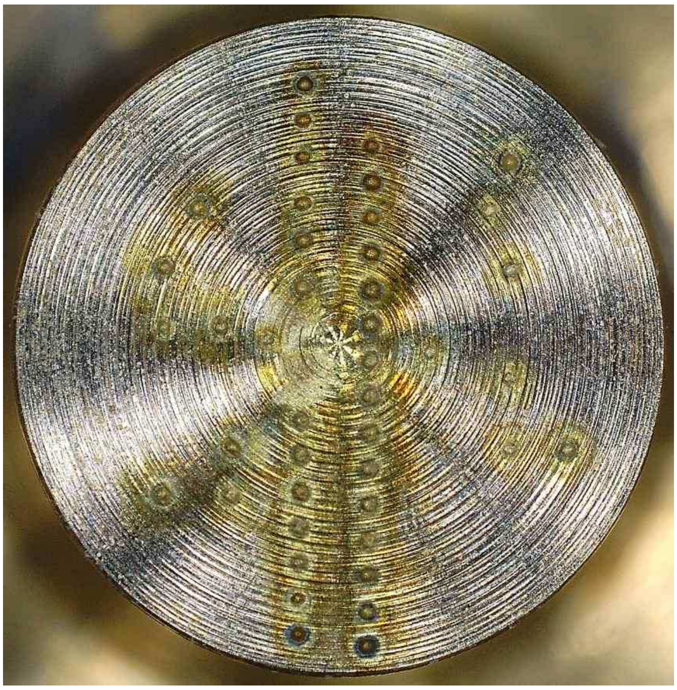

Figure 1.27: microscope picture of the solid brass sample

The shot positions 1 to 15 correspond with the right line of craters shown in the picture above (going from the top the bottom). 16 to 28 are the craters on the left line (going from the bottom to the top). The remaining shot positions are scattered around these lines. Figure 1.26 shows an increase regarding the fluctuation of the crater diameters starting from shot position 29. Furthermore, in Figure 1.27 some of these craters aren´t as defined as the ones in the lines.

This could suggest a spacial dependence of the ablation efficiency. However, as the determined ratios were in good agreement when comparing the shot positions with each other (data not shown) this can be disregarded.

1.5 Summary and Outlook

It is shown in the chapters above that the underwater LA leads to conflicting results. The aim of this work was to investigate if a LA underwater overcomes the fractionation problems a normal LA has and if it would be worth it to work on a combination with a flow digestion setup, which will be described in the next chapters. The relatively good Cu/Zn ratios (deviations <10 %) would indicate that this is indeed the case. However, the Cu/Pb ratios (deviations ~50 %) would beg to differ.

The digestion step proves to be helpful, as it guaranties an independence on the particle size and a possible elemental fractionation in the ICP can be avoided.
Although the microscope pictures indicate molten particles at the crater rims, this doesn´t seem to affect the ratio of the bulk elements, which is actually an improvement to the common LA.

It would be beneficial to compare the obtained results with the ones of others. Unfortunately, as it is described in chapter 1.1.1, the amount of fractionation is dependent on a lot of factors, most of all the laser wavelength and pulse duration used and the sample composition. Therefore, it is almost impossible to find a publication where the same laser (kind of laser, wavelength, pulse duration and energy) as well as the same sample (elemental composition and provider) was used.

To sum this up in one sentence: the system seems to work quite well for the bulk, but not for trace elements. Although, to prove that a lot more samples and additional trace elements would need to be measured.

2 Flow digestion

Microwave assisted digestion is a well-established method for sample preparation. However, in most cases a batch mode system is used, which is not only time consuming and impossible to automate, but an additional cleaning step between digestions is necessary. To overcome these disadvantages a high-pressure flow digestion system can be used.

The flow digestion setup used and developed in this thesis takes the theoretical background of a setup called Autoflow, which was developed by Knapp et al. in 1995 [48]. The Autoflow, while being fully developed and working well analytical wise, had also some drawbacks. The part of the sample loop which was heated was very limited and contained only 3.7 mL. Therefore, the duration of stay of a sample in the heated area was quite short.

To improve the analytical performance a new flow digestion setup was developed, which has undergone several changes in the last few years. Figure 2.1 shows a schematic of the new setup. During the development everything outside of the microwave-heated zone stayed the same.

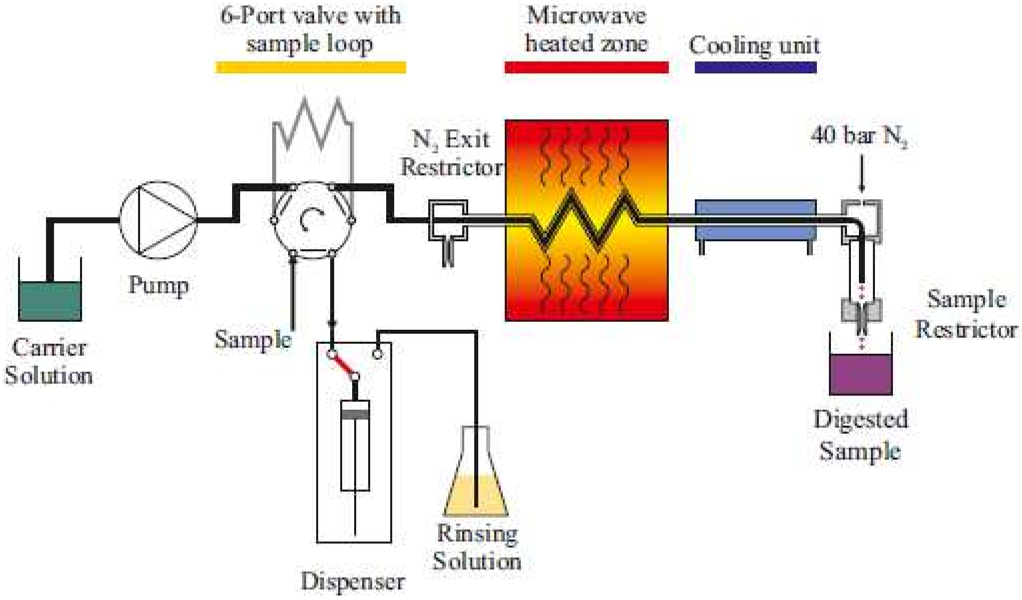

Figure 2.1: Universal schematic of the 'new' flow digestion system

In the following chapters a brief overview over the developing steps is given with a more detailed description of the changes made during this thesis.

Some parts of the setup stayed the same during the whole development. A titanium HCPL pump (Knauer, Germany) was responsible for the constant carrier solution flow and a wide bore, polymer sealed six-port valve (Knauer, Germany) was used for the addition of the sample into the digestion tube. Diluted nitric acid (1 % v/v) was used as a carrier solution with most commonly a flow of 2 or 5 mL min^{-1}. To avoid a dilution of the sample with the carrier solution 2 mL 30 % (v/v) nitric acid were placed in front of and after the sample in the tube, using an electronic dispenser (MultiDispenser, ProLiquid, Germany). The tube consisted of PFA with an inner diameter of 1.5 mm and an outer diameter of 2.5 mm.

As the samples which were used for the development, were mostly slurries it was necessary to implement a stirrer (PEEK paddle) next to the sample uptake needle of the autosampler (ASX-1400, Cetac, USA). Additionally, the autosampler had a second needle installed which was connected to the exit part of the flow digestion setup. To limit the mechanical stress on the digestion tube the surrounding area was pressurized with N_2 to 40 bar. This resulted in a similar pressure inside and outside of the tube, which was beneficial in the case of a violent reaction with the formation of large volumes of gaseous reaction products and a resulting high pressure inside of the PFA tube. The increased pressure would only result in a faster ejection of the liquid and gasses into the exit port unit and not in the damaging of the tube.

A more in-depth description of the system was done by Wiltsche et al. [49].

Glass coil reactor

As already mentioned, the major issue which had to be improved was the heated reactor volume. Prior to the starting point of this thesis a glass coil reactor was used, where borosilicate glass encased the digestion tube. To create the pressure equilibrium the gap between the glass wall and the PFA tube was filled with 40 bar N_2.

The glass coil reactor was placed in the cavity of the commercially available batch system microwave Multiwave 3000 (Anton Paar, Graz, Austria). This cavity has been constructed to contain an explosion of 80 bar, which is double the pressure the flow digestion setup was operated with and comes with several safety features.

Figure 2.2 shows the glass coil reactor inside the microwave cavity, where it was placed above the two waveguides. In the picture they are behind the two white PTFE sheets.

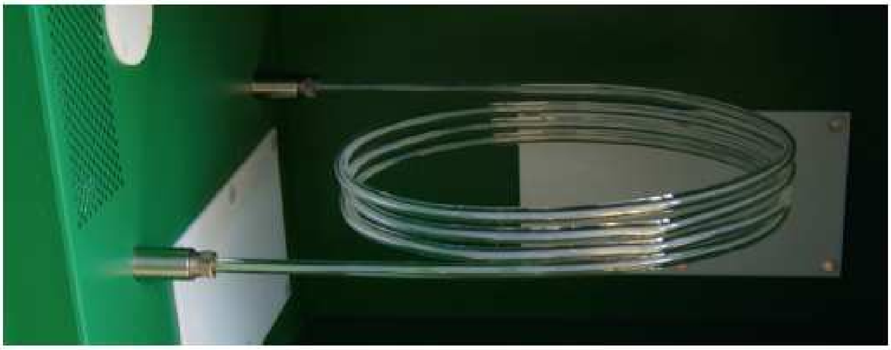

Figure 2.2: Glass coil reactor inside the Multiwave 3000 cavity

A more detailed description of this setup as well as the analytical performance have been reported elsewhere [49]. To sum it up however, while the digestions were optically completed (clear solutions with no remaining particles) and good agreements with certified values were found, a dependency on the composition of the digestion acid cocktail was shown, which should be avoided. Additionally, the system proved to be unsuitable for samples, which are not easily digested, shown by a high residual carbon content (RCC) of the example of glycine. This was assumed to be caused by the still relatively small reactor volume of 6 mL.

Glass tube reactor

To further improve the flow digestion setup and increase the reactor volume the high-pressure glass tube reactor was constructed. The PFA tube was wrapped around a PTFE coil former and encased by a borosilicate glass tube (inner diameter of 28 mm; wall thickness of 9.8 mm). For a pressure tight seal two PEEK endcaps were used. Again, a pressure equilibrium was obtained by a constant N_2 flow between the digestion tube and the glass wall. A picture of the glass tube reactor and its placement in the microwave cavity is shown in the figures below.

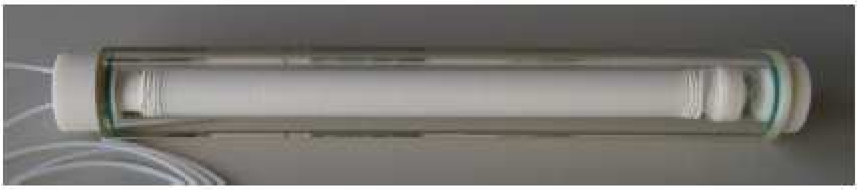

Figure 2.3: Picture of the glass tube reactor, including the coiled digestion tube and end caps

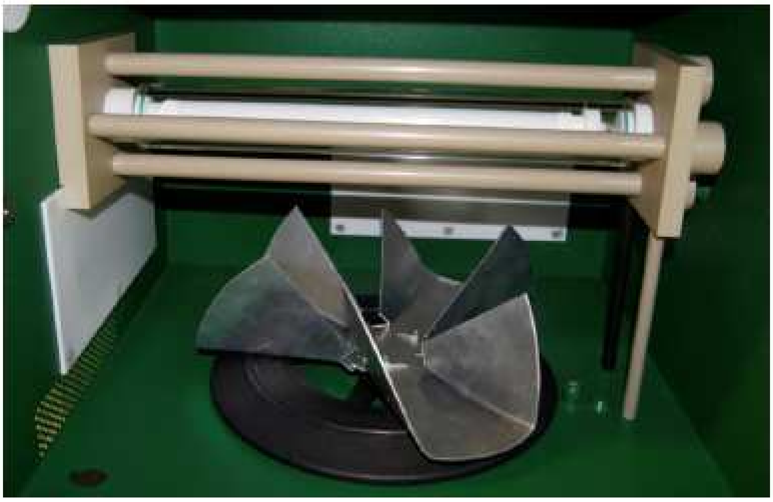

Figure 2.4: Picture of the placement of the glass tube reactor inside the microwave cavity of the Multiwave 3000

This new tube reactor allowed a heated reactor volume of 13.5 mL, which is more than double the volume of the glass coil reactor (6 mL).

An improved digestion efficiency of this setup compared to the glass coil reactor has been shown by Marques et al. [50]. The RCC of glucose at 500 W microwave power was around 2.3 % (~ 20 % with the glass tube reactor) and that of glycine was around 35 % (almost 100 % with the glass tube reactor). The measurement of two standard reference materials showed good agreement with the certified values, with the exception of Fe and Al. These results, as well as the measurement conditions can be found in the publication mentioned above.

Additionally to the standard reference materials, glucose and glycine, as well as two other substances to determine the digestion efficiency, a few ‘real life’ sample were measured. The analysis of bovine liver and muscle, shrimp, spinach, as well as tomato and orange leaves showed in general a good agreement with the reference concentrations obtained by a closed vessel digestion and measurement with ICP-OES [50].

The measurement conditions and results of the analysis of apple juice, mango juice and milk are shown more detailed below.

2.1 Performance evaluation of a high-pressure microwave-assisted flow digestion system for juice and milk sample preparation [51]

Thiago L. Marques, Helmar Wiltsche, Joaquim Nóbrega, Monika Winkler, Günter Knapp

This chapter was published under the title shown above in Anal Bioanal Chem, Volume 409 (2017), pages 4449–4458; DOI: 10.1007/s00216-017-0388-5

2.1.1 Abstract

Acid digestion is usually required for metal determination in food samples. However, this step is usually performed in batch mode which is time consuming, labor intensive, and may lead to sample contamination. Flow digestion can overcome these limitations. In this work, the performance of a high-pressure microwave-assisted flow digestion system with a large volume reactor was evaluated for liquid samples high in sugar and fat (fruit juice and milk). The digestions were carried out in a coiled perfluoroalkoxy (PFA) tube reactor (13.5 mL) installed inside an autoclave pressurized with 40 bar nitrogen. The system was operated at 500 W microwave power and 5.0 mL min^{-1} carrier flow rate. Digestion conditions were optimized with phenylalanine, as this substance is known to be difficult to digest completely. The combinations of HCl or H_2O_2 with HNO_3 increased the digestion efficiency of phenylalanine, and the residual carbon content (RCC) was around 50 % when 6.0 % V/V HCl or H_2O_2 was used in combination with 32 % V/V HNO_3. Juice samples were digested with 3.7 mol L^{-1} HNO_3 and 0.3 mol L^{-1} HCl, and the RCC was 16 and 29 % for apple and mango juices, respectively. Concentrated HNO_3 (10.5 mol L^{-1}) was successfully applied for digesting milk samples, and the RCCs were 23 and 25 % for partially skimmed and whole milk, respectively. Accuracy and precision of the flow digestion procedure were compared with reference digestions using batch mode closed vessel microwave-assisted digestion and no statistically significant differences were encountered at the 95 % confidence level.

2.1.2 Introduction

Milk is an important food in the human diet which is rich in fat, proteins, carbohydrates, and minerals. The major nutrients present in milk are Ca, Mg, P, and S, while Fe and Zn are minor constituents [52–54]. Fruit juices have also been included in human diet as good source of nutrients as carbohydrates, proteins, vitamins, antioxidant compounds, and minerals. The main elements are Ca, K, P, and Mg as macronutrients and Fe, Mn, and Mo as minor nutrients [55,56]. The consumption of both products has increased in the last years, and it is important to control the quality of them [52,56].

Methods for the direct analysis of metals in these samples using spectrometric techniques can be found in the literature. However, both fruit juice with pulp and milk tend to clog the nebulizer during analysis and, consequently, sample filtration or centrifugation steps may be needed [57–62]. Furthermore, matrix effects must be considered when large quantities of carbon are introduced into an inductively coupled plasma optical emission spectrometer (ICP-OES). Wiltsche et al. [63] reported that the carbon enhancement effect is a multifactorial phenomenon strongly dependent on the specific instrument and operational conditions.

Thus, a dedicated sample preparation step is usually necessary for metal determination in these samples to avoid the aforementioned problems. Acid digestion is most commonly used for food samples either in block digestion or by microwave-assisted sample digestion. However, both procedures are performed in batch mode which may led to analytical errors due to element losses and sample contamination during sample handling [52,61,64,65]. Flow digestion systems are attractive alternatives for decreasing sample handling and they inherently avoid contamination and losses. Moreover, collection of the digested samples and dilution can be automated. Fruit juice and milk samples are not easily digested in a flow system. Juice samples are rich in glucose, which can react vigorously with nitric acid resulting in sudden pressure spikes inside the reactor. On the other hand, milk samples are rich in fat and require high digestion temperature to be completely mineralized [49,50,66]. Consequently, it is necessary to use a robust and stable flow digestion system which can be operated at high temperature and pressure to promote an efficient and fast digestion of these samples.

Few high-temperature pressure flow digestion systems with continuous carrier flow have been reported in the literature. Pichler et al. [66] proposed a high-temperature microwave assisted digestion flow system with a polytetrafluoroethylene (PTFE) tube put inside a pressurized autoclave which can stand pressure up to 35 bar and reach temperatures higher than 250 °C. Satisfactory results were obtained for solid certified reference materials; however, the only liquid sample tested was orange juice to evaluate Hg losses during digestion. Wiltsche et al. [49] developed another high-pressure microwave-assisted flow digestion system with a PFA tube inserted into a coiled borosilicate glass tube that was pressurized withN_2 in order to reach higher temperatures (ca. 230 °C) and pressures (40 bar). Solid standard reference materials, milk powder, apple juice, and orange juice have been used to evaluate the flow system performance. However, the digestion efficiency was lower in this system than the prior one [66] due to the small reactor volume inside the microwave-irradiated zone.

Recently, Marques et al. [50] improved the flow digestion system developed by Wiltsche et al. [49] by using a new large volume reactor which increases the sample residence time inside the irradiated zone and thus the digestion efficiency. The new reactor consists of a coiled PFA tube placed inside an autoclave formed by a thick-walled borosilicate tube and two thick polyetherether ketone (PEEK) end caps. The digestion efficiency was similar to that achieved by Pichler et al. [66] and significantly better than with the previous reactor [49]. The new large volume reactor had been used for the digestion of solid samples and solid certified reference materials (animal and vegetable tissues). However, a thorough evaluation of performance for liquid samples, such as juice and milk, is still missing.

Despite some previous attempts to digest orange juice as described before [49], there is no application for fresh milk digestion in high-pressure microwave-assisted flow digestion system. There are just some applications using atmospheric pressure microwave-assisted digestion flow system operated in stopped flow mode [67,68].

The aim of this work was to evaluate the performance of this new high-pressure microwave-assisted flow digestion system to digest juice and milk samples.

2.1.3 Materials and Methods

Instrumentation

An axially viewed ICP-OES (Ciros Vision EOP, SPECTRO Analytical Instruments GmbH, Kleve, Germany) was used to quantify analytes, total carbon content (TCC), and RCC [49]. The liquid samples were diluted in deionized water before TCC determination by ICP-OES. The RCC and consequently the digestion efficiency were based on the carbon content determinations in liquid samples before and after digestion in the flow system. Carbon was determined using the atomic emission line 199.091 nm. The residual acidity in the digests was determined by manual titration with 0.1 mol L^{-1} NaOH standardized solution (Carl Roth, Karlsruhe, Germany) using phenolphthalein as indicator.

An ultrasonic bath (Transsonic T 420, Elma, Germany) and a vortex stirrer (REAX 2000, Heidolph, Germany) were used to homogenize the milk emulsions before digestion in the microwave-assisted digestion flow system or direct analyses in the ICP-OES, respectively. A commercial microwave-assisted sample digestion system (Multiwave 3000, Anton Paar GmbH, Graz, Austria) was used to perform digestions n batch mode (BHF^ rotor; maximum pressure of 40 bar). For batch digestions, a volume of 2 g (ca. 2.0 mL) of liquid sample was mixed with 5 mL concentrated HNO_3 and 0.5 mL concentrated HCl. The microwave power was ramped to 1400 W during the first 15 min. Thereafter, the heating was reduced to maintain 40 bar inside the vessels for additional 20 min. The digests were analyzed by ICP-OES.

Reagents and samples

Deionized water (18 MΩ cm, Barnstead Nanopure, Thermo Fisher Scientific,Waltham,MA, USA) and the following high purity reagents were used to prepare all standards solutions, dispersions, and emulsions: HNO_3 (purified by subboiling in a quartz distiller), HCl (Suprapur, Merck, Germany), H_2O_2 (Pharm., Merck, Germany), and Triton X-100 (p.a., Merck, Germany). Calibration solutions were prepared from a 100 mg L^{-1} multielement standard solution (Carl Roth, Karlsruhe, Germany) and 1000 mg L^{-1} P and S standard solutions (SCP Science, Baie-d'Urfé, QC, Canada) in 3 % V/V HNO_3 for elemental analysis and potassium hydrogen phthalate (p.a., Merck, Germany) for RCC determination.

Phenylalanine solutions were prepared from its respective solid (p.a., Merck, Germany). Samples studied in this work were apple juice (100 % Apfel, SPAR, Austria), mango juice (Happy Day, RAUCH, Austria), partially skimmed milk (0.9 % fat, Österreichische Bio-Bergbauern-Leichtmilch, Naturapur SPAR, Austria), and whole milk (3.5 % fat, Vollmich, Jeden Tag, Austria) obtained in local supermarket in Graz, Austria. Aliquots of 50 mL of these samples were transferred to polyethylene tubes and stored in a freezer at −18 °C for later analysis.

Flow digestion system

A high-pressure microwave-assisted digestion flow system with a large volume reactor (13.5 mL) operated in continuous flow mode was used in this work (Figure 2.5). The new reactor has been thoroughly described in a previous publication [50]. A solution of 0.2 mol L^{-1} HNO_3 was used as carrier solution. The flow digestion system is fully computer controlled allowing unattended operation. Previously optimized conditions (500 W microwave power and 5.0 mL min^{-1} carrier flow rate) were also used in this work [50]. The measurements were performed off-line, and the digested solutions were analyzed by ICP-OES to determine analytes and RCC.

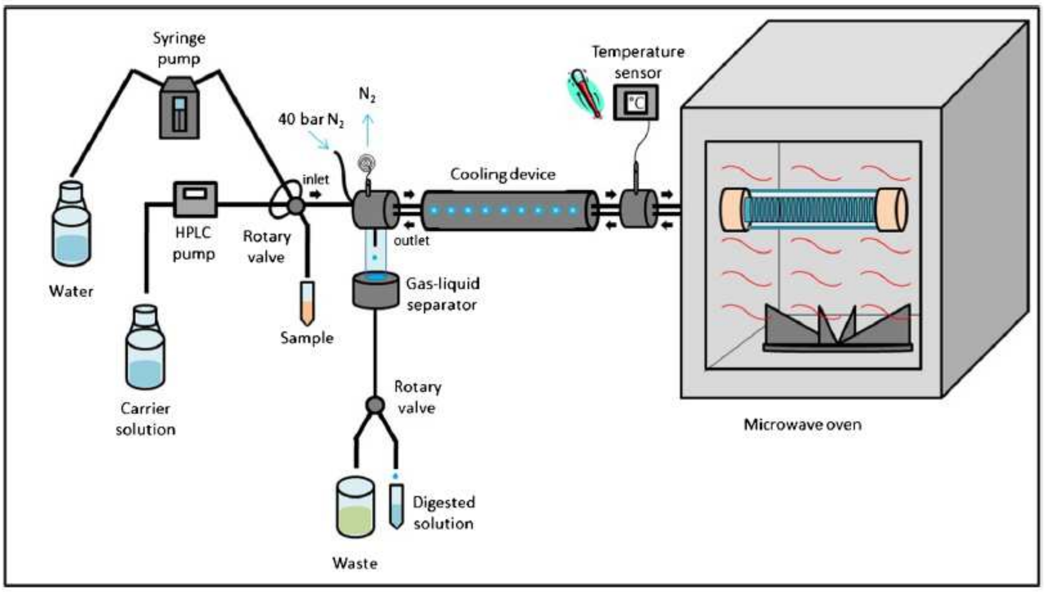

Figure 2.5: Schematic of the high-pressure microwave-assisted flow digestion system

Sample preparation

Phenylalanine standard solutions

Phenylalanine is difficult to digest due to the presence of a stable aromatic ring which requires aggressive conditions [69,70]. In the previous work developed by Marques et al. [50], the digestion efficiency was 77.9 ± 0.7 %, when digesting a phenylalanine standard solution with 5.0 g L^{-1} of total carbon content in 6 mol L^{-1} HNO_3 at optimized conditions (500 W microwave applied power and 5.0 mL min^{-1} carrier flow rate). In order to improve the digestion efficiency in this system, the combination of 6 mol L^{-1} HNO_3 with HCl (0.5, 0.9, and 1.9 mol L^{-1}) or H_2O_2 (0.5, 1.0, and 2.0 mol L^{-1}) was evaluated. Similarly to the previous study, 2 mL of phenylalanine solution with 5.0 g L^{-1} of total carbon content was used.

Juice samples

Juice samples were prepared in different acid media (3.7 mol L^{-1} HNO_3, 3.7 mol L^{-1} HNO_3 plus 0.3 mol L^{-1} HCl, or 3.7 mol L^{-1} HNO_3 plus 0.3 mol L^{-1} H2O2). During flow digestion, a sample aliquot of 2.4 mL was embedded in 3.6 mL of 3.7 mol L^{-1} HNO_3 to avoid dilution by the carrier solution at the ends of the sample segment. After digestion, the collected samples were made up to a final volume of 40 mL (dilution factor 1:25 v/v). Juice samples were also analyzed directly after dilution with ICP-OES based on the procedure proposed by Cindrić et al. [62]: a sample volume of 500 µL (ca. 500 mg) of juice was diluted to 10 mL in 2 % v/v HNO_3 (dilution factor 1:20 v/v). Scandium at a concentration of 1 mg L^{-1} was used as an internal standard in ICP-OES measurements.

Milk samples

Initially, the best strategy to prepare a milk emulsion in acid medium had to be evaluated, since milk coagulates in acid medium causing heavy protein precipitation. In order to prepare a homogenous milk emulsion, stabilizers, sonication, and heating effects on the emulsion preparation were studied. In four different flasks, 0.8 mL of whole milk was mixed with 2.0 mL concentrated nitric acid. The first flask served as reference solution without adding other reagents; in the second, one 50 µL of 0.2 mol L^{-1} EDTA was added; in the third, 50 µL of 10 % w/w Triton X-100; and in the fourth, 50 µL of 0.2 mol L^{-1} EDTA plus 50 µL of 10 % w/w Triton X-100. The volume of all flasks was made up to 4 mL with deionized water in order to prepare a 20 % v/v milk emulsion. All solutions were shaken thoroughly by hand and were allowed thereafter to rest for 4 min, before being sonicated in an ultrasonic bath for 1 min. It was found that a stable milk emulsion could be prepared by mixing 1 mL of milk sample, which was diluted with concentrated nitric acid to 4 mL with the internal standard, and sonicating the resulting emulsion for 1 min in an ultrasonic bath.

These optimized methods were used to prepare milk emulsions to be digested in the microwave-assisted flow digestion system. Thus, milk samples were prepared in a final concentration of 20 and 25 % v/v in 7.0 and 10.5 mol L^{-1} HNO_3. Sample aliquots of 3.0 mL were introduced into the flow system embedded between 1.0 mL HNO_3 segments with same acid concentration as the sample (7.0 or 10.5 mol L^{-1} HNO_3). The collected fraction was diluted to a final volume of 36 mL when working with a 20 % v/v milk emulsion (dilution factor 1:60 v/v) and 30 mL for a 25 % v/v milk emulsion (dilution factor 1:40 v/v). Milk direct analyses were based on the method developed by McKinstry et al. [57]: 250 mg (ca. 250 µL) of milk was diluted in 6 mL of deionized water (ca. 37 °C) and mixed using a vortex stirrer. After the dispersion rested to reach room temperature, 100 µL of a 10 % w/w Triton X-100 solution was added and then the emulsion was diluted to a final volume of 10 mL (dilution factor 1:40 v/v). Scandium was added as an internal standard solution (1.0 mg L^{-1}) to all emulsions. Analytes were determined using an ICP-OES, and a 1 % w/w Triton X-100 solution was used for rinsing.

Performance evaluation

The digestion efficiency of the high-pressure microwave-assisted digestion flow system was evaluated by determining the RCC and the residual acidity in the samples. The limits of detection (LODs) were determined by the blank method using blank samples from the flow digestion system. The LODs were calculated based on the literature [71,72], using background equivalent concentrations (BEC), signal-to-background ratios (SBR), and relative standard deviations (RSD). Accuracy and precision were estimated by comparing results obtained with the flow digestion system with those obtained by microwave-assisted digestion in closed vessels. Values were statistically compared by using F and t tests.

2.1.4 Results and discussion

The conditions of sample digestion, such as the sample volume and the digested solution volume collected, are easily changed since the flow system is fully computer controlled. Both juice samples and milk react violently when heated with nitric acid, generating large volumes of gaseous decomposition products (CO_x and NO_x). However, due to the system pressure of 40 bar, these reaction products remain dissolved in the digestion acid mixture and are liberated only during the depressurization step. It is interesting to note that the reaction of juice and milk with nitric acid is significantly more violent than the solid samples investigated in a previous study [50]. The sample throughput was eight samples per hour when including the time needed for sampling and collection digest solution. On the other hand, the commercial microwave oven used for batch mode digestions contained a rotor with 16 vessels. The heating program applied for sample digestion and the cooling down the vessels after digestion took around 40 min plus additional 10 min of sample handling (pouring into polypropylene tubes and making up to volume). Also, after sample digestion, a cleaning step was required that took additional 30 min. Thus, the effective sample throughput for microwave-assisted digestion in closed vessels was around 12 samples per hour. Clearly, the sample throughput of a batch mode digestion system will depend strongly on the number of samples that can be processed in parallel (rotor type), the applied digestion program, and the cooling capabilities of the instrument after digestion. In the adopted conditions, the sample throughput of the digestion flow system was lower than in the microwave-assisted digestion in batch mode but is important to note that flow systems are inherently capable of parallel operation. By installing several digestion reactors inside the microwave cavity, the sample throughput could be easily increased.

Phenylalanine standard solution

In order to assess the digestion efficiency of the high-pressure microwave-assisted flow digestion system, phenylalanine was used as reference sample to optimize the digestion acid mixture. The molar concentrations for HCl and H_2O_2 were converted to % v/v for better data visualization in Figure 2.6. Both HCl and H_2O_2 improved the digestion efficiency. At 1.5 % v/v HCl, the digestion was more efficient than at the same concentration of H_2O_2, but at higher concentrations, the mixture of HNO_3 plus H_2O_2 was as efficient as the mixture containing the same concentration of HCl and HNO_3. However, the increase in the H_2O_2 concentration led to the formation of large volumes of gas that could not be absorbed in the digestion acid and consequently the sample was prematurely ejected from the reactor. Based on these observations, HCl was considered the best option to improve phenylalanine digestion.

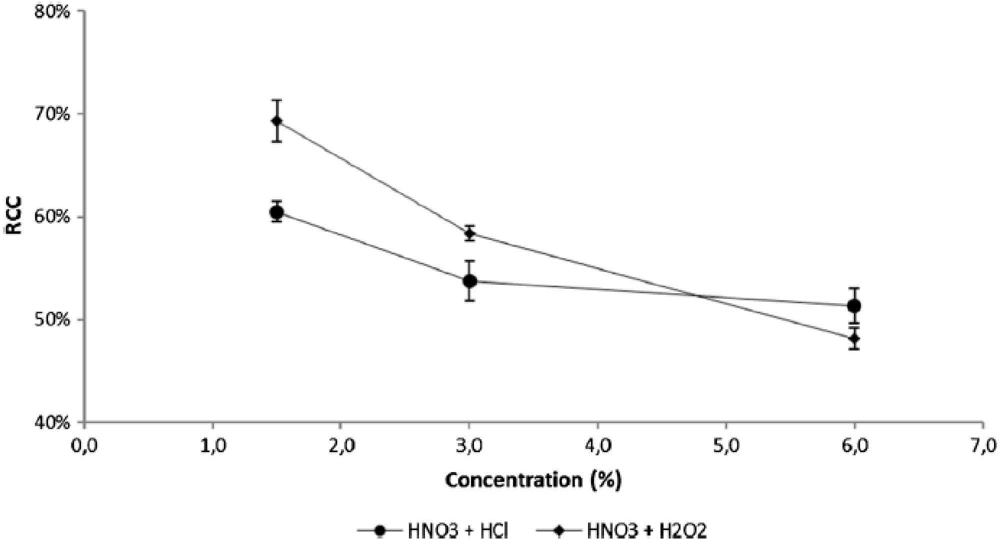

Figure 2.6: Effect of combination of HCl or H_2O_2 with HNO_3 on the digestion efficiency of phenylalanine at 500 W microwave power and 5.0 mL min^{-1} carrier flow rate

Juice samples

Juice samples are rich in sugars (about 120 g L^{-1} of glucose and fructose), which are easily digested, but leading to vigorous reactions with huge gas formation which led to premature ejection of the sample from the microwave-irradiated zone. Digestions were carried out using concentrated juice sample suspensions (67 % v/v juice), in order to avoid excessive sample dilution. The digestions using the microwave-assisted flow system were tested using the following acid solutions: 3.7 mol L^{-1} HNO_3, 3.7 mol L^{-1} HNO_3 plus 0.3 mol L^{-1} HCl, or 3.7 mol L^{-1} HNO_3 plus 0.3 mol L^{-1} H_2O_2. The RCCs in the juice digests were 22, 16, and 22 % for apple juice and 41, 29, and 46 % for mango juice digested with HNO_3, HNO_3 plus HCl, or HNO_3 plus H_2O_2, respectively. Best digestion efficiencies were obtained for apple juice which is a clarified juice without large suspended particles. The best reagent mixture was the combination of HNO_3 and HCl for both samples. Similar behaviour was observed in the abovementioned experiments with phenylalanine and for animal tissues digested using this same flow system in a previous work [50].

The residual acidities determined in all digested juice samples were around 0.6 mol L^{-1}. Since this residual acidity comes from sample, carrier solution, as well as from the acid used to embed the sample plug, it is important to establish the amount of acid effectively consumed for sample digestion. Considering just the sample plug, the acid consumption was about 90 %, which means that it is possible to perform online measurements of juice samples without dilution due to the low residual acidity (0.3 mol L^{-1}).

Limits of detection were determined in five replicates for each mixed acid solution. Average LODs for each element in the procedure blank are reported in Table 2.1.

Table 2.1: Limit of detections for flow digestion and batch mode digestions. Concentrations in µg L^{-1} and n=5

Element	**Flow System**		**Batch Digestion Milk and Juice**
	Juice	Milk	
Al	7	-	10
B	8	-	30
Ba	7	-	1
Ca	200	300	30
Cu	6	-	10
Fe	2	1	3
K	50	60	150
Mg	20	30	8
Mn	0.4	-	0.4
Na	10	60	10
P	10	10	30
S	30	30	80
Sr	0.5	0.3	0.2
Zn	1	30	4

The LODs were better in the flow system for Al, B, Cu, K, P, S, and Zn, while they were better in the batch mode digestion for Ba, Ca, Mg, and Sr.

The analyte concentrations determined in juice samples are shown in Table 2.2.

Table 2.2: Comparison of flow and closed vessel batch digestion of apple and mango juices in different acid solutions (mean value ± standard deviation, n=5)

Sample	**Element [mg L^{-1}]**	**Flow digestion**			**Closed vessel digestion HNO_3 + HCl[d]**
		HNO_3[a]	HNO_3 + HCl[b]	HNO_3 + H_2O_2[c]	
Apple juice	Al	0.40 ± 0.03	0.39 ± 0.03	0.35 ± 0.03	0.4 ± 0.1
	B	1.6 ± 0.1	1.74 ± 0.06	1.57 ± 0.05	1.86 ± 0.06
	Ba	0.18 ± 0.01	0.10 ± 0.01	0.07 ± 0.01	0.11 ± 0.01
	Ca	115 ± 4	123 ± 4	116 ± 4	123 ± 4
	Fe	0.87 ± 0.03	0.85 ± 0.03	0.80 ± 0.03	0.85 ± 0.03
	K	740 ± 30	800 ± 30	620 ± 20	670 ± 20
	Mg	53 ± 2	55 ± 2	51 ± 2	53 ± 2
	Mn	0.38 ± 0.01	0.38 ± 0.01	0.36 ± 0.01	0.38 ± 0.01
	Na	13.8 ± 0.5	15.3 ± 0.5	14.1 ± 0.5	15.0 ± 0.4
	P	63 ± 2	68 ± 2	60 ± 2	63 ± 2
	S	27 ± 1	29 ± 2	26 ± 2	27 ± 2
	Sr	0.79 ± 0.04	0.83 ± 0.03	0.75 ± 0.03	0.79 ± 0.02
	Zn	0.11 ± 0.02	0.10 ± 0.01	0.10 ± 0.01	0.10 ± 0.02
Mango juice	Al	0.14 ± 0.02	0.08 ± 0.01	0.075 ± 0.003	0.16 ± 0.04
	B	0.7 ± 0.1	0.18 ± 0.03	0.13 ± 0.02	0.13 ± 0.02
	Ba	107 ± 4	90 ± 3	92 ± 3	92 ± 3
	Cu	ND	0.1 ± 0.02	0.15 ± 0.01	0.15 ± 0.02
	Fe	0.51 ± 0.04	0.44 ± 0.02	0.45 ± 0.02	0.48 ± 0.05
	K	350 ± 10	330 ± 10	350 ± 10	330 ± 10
	Mg	48 ± 2	44 ± 2	45 ± 2	44 ± 2
	Mn	0.36 ± 0.01	0.33 ± 0.01	0.35 ± 0.01	0.34 ± 0.02
	Na	10.1 ± 0.3	9.7 ± 0.3	9.7 ± 0.3	9.8 ± 0.3
	P	39 ± 1	37 ± 1	37 ± 1	37 ± 1
	S	33 ± 1	31 ± 1	32 ± 1	30 ± 2
	Sr	0.63 ± 0.02	0.59 ± 0.02	0.59 ± 0.02	0.58 ± 0.02
	Zn	0.26 ± 0.02	0.27 ± 0.02	0.28 ± 0.02	0.27 ± 0.03

ND not determined

[a] 3.7 mol L^{-1} HNO_3

[b] 3.7 mol L^{-1} HNO_3 and 0.3 mol L^{-1} HCl

[c] 3.7 mol L^{-1} HNO_3 and 0.3 mol L^{-1} H_2O_2

[d] 9.3 mol L^{-1} HNO_3 and 0.8 mol L^{-1} HCL

In general, results are in good agreement with those determined by the reference method (i.e., microwave-assisted digestion in closed vessels). Not surprisingly, he acid mixture used for juice digestion affected the results. This effect was also observed in batch digestions and in a previous work [49,50]. The acid mixtures were evaluated and compared using statistical tests (F and t tests). According to F test presented in Table 2.3, the precision for samples digested in the flow system was not different from those digested in batch mode, with exception for Al in both samples and all mixed acids, Ba in mango juice digested in 3.7 mol L^{-1} HNO_3, and Fe in in mango juice digested in 3.7 mol L^{-1} HNO_3 plus 0.3 mol L^{-1} H_2O_2. Based on paired t test (see Table 2.3), most macro- and micronutrient concentrations determined in apple and mango juices in different digests were in agreement with those determined using closed vessel microwave-assisted digestion. Only for B and K in apple juice for all studied acid solutions there were no agreement with reference values. All other determined elements were in agreement with reference values at least for one studied acid solution. Therefore, based on F test and t test, it may be concluded that the developed procedure for fruit juice sample preparation using the flow digestion system presented good precision and accuracy, respectively.

Table 2.3: Evaluation of precision and accuracy of flow digestion procedure for fruit juice sample preparation using different digestion solutions and direct analysis procedure based on *F*-test and *t*-test respectively, n=5, P=95 %, ND= not determined, F_{cri}=6.63, t_{cri}=2.30 and t_{cri} exceptions: *2.57 and **2.78

Sample	**Element**	**Flow digestion system**						**Direct analysis**	
		HNO_3		HNO_3 + HCl		HNO_3 + H_2O_2			
		F_{cal}	t_{cal}	F_{cal}	t_{cal}	F_{cal}	t_{cal}	F_{cal}	t_{cal}
Apple juice	Al	12.20	0.79*	17.16	0.74**	12.75	0.18*	25.85	0.73**
	B	3.21	4.73	1.13	2.84	0.72	7.55	1.60	10.74
	Ba	1.01	8.39	2.50	1.24	1.07	5.28	2.50	1.60
	Ca	1.15	3.44	1.32	0.03	1.18	2.71	4.56	1.35
	Fe	1.37	0.88	1.31	0.16	1.16	3.14	1.26	1.09
	K	1.63	5.06	1.87	8.39	1.13	3.92	1.08	5.07
	Mg	2.12	0.49	1.42	1.77	1.23	1.71	1.25	1.34
	Mn	1.28	0.81	1.31	0.16	1.33	3.05	1.38	1.11
	Na	1.13	3.95	1.39	1.19	1.17	3.01	1.40	1.37
	P	1.33	0.19	1.53	3.64	1.21	2.23	1.47	2.52
	S	2.50	0.04	1.58	1.75	1.39	0.78	5.71	2.57
	Sr	2.76	0.0	1.45	2.26	1.18	2.71	1.28	0.78
	Zn	2.55	0.65	3.94	0.22	5.34	0.61	5.01	3.15
Mango juice	Al	7.89	1.21*	14.80	3.93*	292.35	4.31*	2.78	3.00
	Ba	76.69	8.28**	2.51	3.58	1.75	0.11	14.59	1.88*
	Ca	1.78	7.27	1.25	1.37	1.33	0.21	1.33	0.15
	Cu	ND	23.22	1.60	4.14	3.03	0.19	1.49	0.87
	Fe	1.75	0.81	4.08	2.10	9.09	1.55*	10.35	2.92*
	K	1.55	3.97	1.33	0.10	1.51	3.25	1.50	3.16
	Mg	1.02	3.96	1.22	0.05	1.15	1.28	1.15	1.27
	Mn	2.72	1.35	3.18	1.65	2.74	0.86	2.62	1.64
	Na	1.40	1.32	1.41	0.55	1.31	0.28	1.14	3.71
	P	1.45	2.32	1.34	0.42	1.31	0.16	1.44	2.10
	S	1.78	3.20	1.95	1.53	1.90	2.00	1.84	6.74
	Sr	1.54	3.97	1.39	1.21	1.36	0.77	1.46	2.55
	Zn	2.30	0.65	2.10	0.06	3.42	0.44	6.13	1.51

The direct analysis proposed by Cindrić et al. [62] for juice samples seems to be a simple and fast procedure that may be easily applied in routine analyses, because it is not necessary to digest the sample. Based on F test showed in Table 2.3, there were no significant differences among the precision for most elements determined by direct analysis and by batch mode digestion. The only exceptions were Al in apple juice and Ba and Fe in mango juice. According to a paired t test, most analytes showed no statistical difference with values determined using the reference digestion method (Table 2.3). In general, determinations were not accurate for B, K, P, S, and Zn in apple juice and Al, Fe, K, Na, and S in mango juice. Thus way, accurate determinations could be performed by both evaluated procedures (flow digestion and direct analysis); however, the developed flow digestion procedure presented a higher number of elements accurately determined when compared to the batch mode digestion. Moreover, the lower carbon content determined in the digested solutions would cause less carbon matrix effects on macro- and micronutrient determinations by ICP-OES [63].

Milk samples

The performance of the microwave-assisted flow digestion system was also evaluated for milk samples, since this type of sample is rich in fat which is difficult to digest [73]. Moreover, the preparation is not straightforward, as it is well known that acidification leads to heavy protein precipitation that in general causes severe problems in both direct analysis and digestion. In fact, even the addition of a small volume of an internal standard (about 1 % v/v of the sample volume) was found to lower the pH sufficiently to initiate a phase separation. Once the coagulation has started, even prolonged sonication in the ultrasonic bath did not produce a homogeneous phase again.

It is important to note that in batch digestion, the coagulation is not problematic, as commonly the sample is brought into contact with the acid in the digestion vessel. For direct analysis, however, coagulation will result in a nonrepresentative aerosol and possibly nebulizer clogging. In flow digestion systems, any coagulation prior the introduction into the sample loop will result in a non-representative sampling. It is therefore important that the acidified milk samples will be stable long enough until being introduced into the flow digestion system. An alternative approach would be an online mixing of milk and acid after the automatic sampler. This option was not available on the investigated flow digestion system but will be pursued in the future.

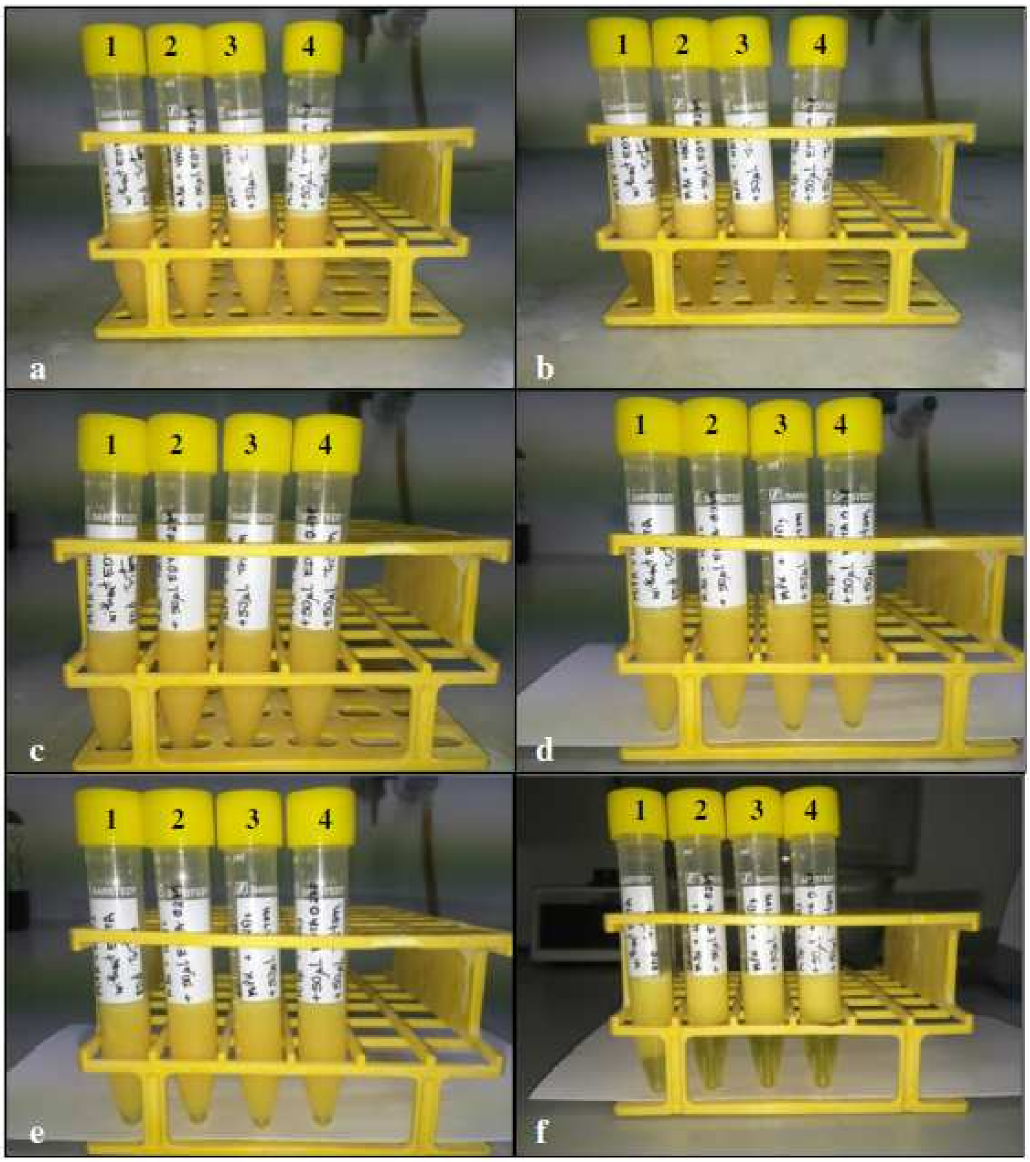

Figure 2.7: Optimization of milk emulsion preparation: effect of stabilizers, ultrasonic bath, and heating on emulsion stability and homogeneity. **a** After sample and reagents mixing and shaking. **b** Four minutes after shaking. **c** after sonication. **d** Twenty minutes after sonication **e** Fourty-four minutes after sonication. **f** After 20 min of heating. *1* Without chemical stabilizer. *2* With EDTA. *3* With Triton X-100. *4* With EDTA and Triton X-100

As shown in Figure 2.7, different approaches for circumventing this precipitation prior digestion have been evaluated: 0.2 mol L^{-1} EDTA, 10 % w/w Triton X-100, and their combination were investigated as emulsion stabilizers for acidified milk samples. All emulsions seemed stable immediately after reagent mixing and sample shaking (Figure 2.7a), but phase separation was observed in less than 4 min (Figure 2.7b). Sonication in an ultrasonic bath for 1 min (Figure 2.7c) improved the stability of the milk emulsions to about 20 min before phase separation started (Figure 2.7d). Emulsions prepared by mixing milk, nitric acid, and deionized water (Figure 2.7e) followed by 1-min sonication in the ultrasonic bath proved most stable showing signs of phase separation only after 44 min. To further improve the stability of the milk/acid emulsion, a predigestion step in an oven at 60 °C for 20 min was investigated. However, the heating quickly led to a complete phase separation (Figure 2.7f), and the solutions could not be homogenized thereafter even when they were sonicated in an ultrasonic bath. From this experiment, it became apparent that the addition of EDTA and/or Triton X-100 did not improve the stability of the acidified milk, but sonication in an ultrasonic bath proved to be feasible.

Milk samples were digested using nitric acid solutions containing 7.0 and 10.5 mol L^{-1} HNO_3 for 20 and 25 % v/v milk emulsions after 1-min sonication in ultrasonic bath, respectively. The RCCs found in the milk digests were 34 and 23 % for partially skimmed milk and 34 and 25 % for whole milk digested with 7.0 and 10.5 mol L^{-1} HNO_3, respectively. Best results were found using the latter condition for both milk sample types. These results can be explained by the higher nitric acid concentration. The residual acidities for partially skimmed and whole milk were 1.0 and 1.7 mol L^{-1} in the milk samples digested in 7.0 and 10.5 mol L^{-1} HNO_3, respectively. Similarly, to the discussion for juice samples, acid consumption was also evaluated considering the sample plug and an acid consumption of 45 and 39 % was encountered in the milk samples digested in 7.0 and 10.5 mol L^{-1} HNO_3, respectively.

The LODs were also determined in five replicates for each acid concentration, and a mean LOD for each element in the procedure blank was calculated (Table 2.1), since there was no significant difference between the values obtained in 7.0 and 10.5 mol L^{-1} HNO_3. Better LODs were reached in the flow system for Fe, K, P, S, and Zn, while they were better in the batch mode digestion for Ca, Mg, and Na.

Element concentrations determined in milk samples are listed in Table 2.4.

Table 2.4: Comparison of flow and closed vessel batch digestion of partially skimmed and whole milk in different acid solutions (mean value ± standard deviation, n=5)

Sample	**Element [mgL^{-1}]**	**Flow digestion system**		**Closed vessel digestion HNO_3 + HCl^c**
		HNO_3^{a}	HNO_3^{b}	
Partially skimmed mild	Ca	1413 ± 68	1259 ± 43	1236 ± 43
	Fe	0.10 ± 0.03	0.12 ± 0.04	0.14 ± 0.03
	K	1203 ± 50	1214 ± 42	1092 ± 38
	Mg	114 ± 6	103 ± 4	104 ± 4
	Na	354 ± 17	337 ± 12	318 ± 11
	P	1026 ± 38	950 ± 33	945 ± 33
	S	334 ± 25	323 ± 19	332 ± 21
	Sr	0.22 ± 0.03	0.21 ± 0.02	0.21 ± 0.01
	Zn	3.8 ± 0.2	3.5 ± 0.1	3.7 ± 0,1
Whole milk	Ca	1405 ± 68	1231 ± 42	1232 ± 42
	Fe	0.4 ± 0.5	0.62 ± 0.02	0.19 ± 0.06
	K	1189 ± 41	1160 ± 40	1067 ± 37
	Mg	115 ± 5	100 ± 3	106 ± 4
	Na	351 ± 14	322 ± 11	309 ± 11
	P	1058 ± 37	949 ± 33	991 ± 34
	S	352 ± 24	327 ± 18	356 ± 29
	Sr	0.34 ± 0.04	0.28 ± 0.01	0.28 ± 0.02
	Zn	4.2 ± 0.2	3.7 ± 0.1	4.2 ± 0.2

ND not determined

^{a}7.0 mol L^{-1} HNO_3

^{b}10.5 mol L^{-1} HNO_3

^{c}9.3 mol L^{-1} HNO_3 and 0.8 mol L^{-1} HCl

Table 2.5: Evaluation of precision and accuracy of flow digestion procedure for milk sample preparation using different nitric acid concentrations based on *F*-test and *t*-test, respectively, n=5, P=95 %, F_{cri}=6.63, t_{cri}=2.30 and t_{cri} exceptions: *2.78 and **2.57

Sample	**Element**	**Flow digestion system**				**Direct analysis**	
		7.0 mol L^{-1} HNO_3		10.5 mol L^{-1} HNO_3			
		F_{cal}	t_{cal}	F_{cal}	t_{cal}	F_{cal}	t_{cal}
Partially skimmed milk	Ca	2.51	5.09	1.04	0.85	1.03	0.72
	Fe	1.19	1.65	1.54	0.58	1.32	0.47
	K	1.74	4.04	1.24	4.88	1.12	2.61
	Mg	2.63	3.42	1.01	0.27	1.05	1.04
	Na	2.50	3.99	1.13	2.7	1.30	6.01
	P	1.37	3.60	1.01	0.24	1.15	3.25
	S	1.40	0.78	1.17	0.72	1.04	2.36
	Sr	20.67	0.62*	6.30	0.55	1.18	3.70
	Zn	1.87	0.38	0.88	2.83	1.11	2.36
Whole milk	Ca	2.58	4.95	1.00	0.02	1.04	0.96
	Fe	52.67	1.20*	7.27	14.67**	13.99	2.44**
	K	1.24	4.95	1.18	3.85	1.12	2.51
	Mg	2.13	3.35	1.10	2.28	1.01	0.28
	Na	1.67	5.35	1.08	1.78	1.29	5.86
	P	1.14	3.01	1.09	2.01	1.05	1.02
	S	1.533	0.26	2.72	1.91	2.21	0.13
	Sr	2.23	2.91	6.09	0.12	1.68	2.49
	Zn	1.82	0.24	1.52	5.34	1.34	2.47

Generally, results were in good agreement with those determined by microwave-assisted closed vessel digestion. Based on *F* test (Table 2.5), there were no statistical differences between precision in the flow system and in batch mode for most elements in both acid concentrations, with exception for Fe in whole milk in both acid concentrations and Sr in partially skimmed milk digested in 7.0 mol L^{-1} HNO_3. According to a paired *t* test (Table 2.5), there were significant differences among most elements determined in milk samples digested with 7.0 mol L^{-1} HNO_3 using the flow digestion system compared to those determined by microwave-assisted digestion. At this acid concentration, just Fe, S, Sr, and Zn determinations in both milk samples and Sr in partially skimmed milk were in good agreement with reference contents. Better results were obtained when using 10.5 mol L^{-1} HNO_3 for milk sample digestion. There were no significant differences for Ca, Mg, P, S, and Sr determinations in both samples and Fe in partially skimmed milk and Na in whole milk. Based on the statistical tests, the developed procedure for milk samples digestion with 10.5 mol L^{-1} HNO_3 using the microwave-assisted flow digestion system presented good precision and accuracy when compared with the reference method.

The direct analysis of milk samples proposed by McKinstry et al. [57] seems a simple and fast alternative to the flow digestion approach used in this work. This procedure just requires a vortex stirrer for mixing the milk sample with Triton X-100 and water. The direct analysis of milk samples however required changing the rinsing solution to 1 % w/w Triton X-100 instead of the commonly applied diluted nitric acid, as otherwise severe coagulation of the milk happened inside spray chamber and nebulizer. McKinstry et al. used radial observation of the plasma and a high solid nebulizer. It is known that spectral interferences are more intense in axially viewed plasmas than in a radial viewed ICP-OES [74]. Therefore, it was decided to prepare more diluted emulsions (dilution factor 1:40 v/v). When adopting these strategies, measurements could be performed without critical problems. It is important to note that despite using a surfactantcontaining rinsing solution, it was necessary to clean the entire sample introduction system after the end of the analysis by washing with a detergent and then soaking overnight in an acid solution (HNO_3 10 % v/v) for removing solid protein remains.

There were no significant differences among the precision for macro- and micronutrient determinations by direct analysis and the reference method based in an *F* test (Table 2.5), with exception for Fe in whole milk. According to a paired *t* test, most elements determined by direct analysis showed significant differences compared with those contents determined using the reference method (Table 2.5). Good agreement was achieved just for Ca, Fe, and Mg determinations in partially skimmed milk and Fe, Mg, P, and S in whole milk. Consequently, for accurate macro- and micronutrient determination in milk samples is recommended to perform sample digestion either using flow digestion system or using microwave-assisted digestion in closed vessel.

2.1.5 Conclusions

The high-pressure microwave-assisted digestion flow system was able to digest juice and milk samples without difficulties. The combination of HNO_3 and HCl resulted in lower RCCs in juice digestions. When compared to fruit juice, milk samples were more difficult to digest due to the fat content. Moreover, it was found that for milk samples, the most critical step was the preparation of a stable, acidified milk emulsion. Results obtained using the high-pressure microwave-assisted flow digestion system were in good agreement with those obtained with the reference method, i.e., microwave-assisted digestion in closed vessel. Based on comparison with the reference method, direct analysis of milk after dilution was found to be a good alternative but required special care to avoid cross-contamination and nebulizer clogging. However, it is important to mention that for milk samples, a higher dilution was necessary than that proposed in the literature due to the use of ICP-OES with axial viewing.

2.2 Coaxial microwave cavity

2.2.1 Introduction and experimental

The previous chapters have shown that a successful increasing of the reactor volume has been done and that the analytical performances are in general satisfactory. However, for both reactors which have been discussed the relatively large microwave cavity of the Multiwave 3000 was used. Such a large cavity is not only not necessary, but also comes with a few disadvantages. Apart from the space needed it is also quite expensive and has most likely am inhomogeneous microwave filed distribution. Although this can be compensated to a certain extent by a metallic mode stirrer at the bottom of the cavity it is assumed that a microwave field changes depending on the sample in the digestion tube.

The aim of this step of the flow digestion development was to build a microwave cavity in which the microwave field was distributed homogeneously and the energy was transferred more efficiently into the sample. For this purpose, a PFA digestion tube (inner diameter 1.5 mm; outer diameter 2.5 mm) was coiled around a hollow PTFE coil former, similar to the glass tube reactor, but in this case the coiling was done in two layers. Consequently, the total volume in the heated zone could be further increased to 21 mL. A PTFE tape was used at both ends to keep the digestion tube in place. An outer PTFE tube covered the digestion tube and was sealed with two PEEK end caps. The pressure autoclave was a titanium tube with an outer diameter of 80 mm and a wall thickness of 15 mm.

The microwave applicator was designed similarly to a coaxial cable. An inner conductor (aluminium rod with a diameter of 10 mm) was placed inside the hollow PTFE coil former and was stabilised with the end caps. That, in combination with the titanium autoclave formed the coaxial arrangement.

Similar as to the other two setups already discussed, the PFA tube entered and left the autoclave through two stainless steel tubes, which were also the in and out for the N_2 used to create the pressure equilibrium.

The schematic of this setup as well as the actual appearance is shown in the Figure 2.8 and Figure 2.9.

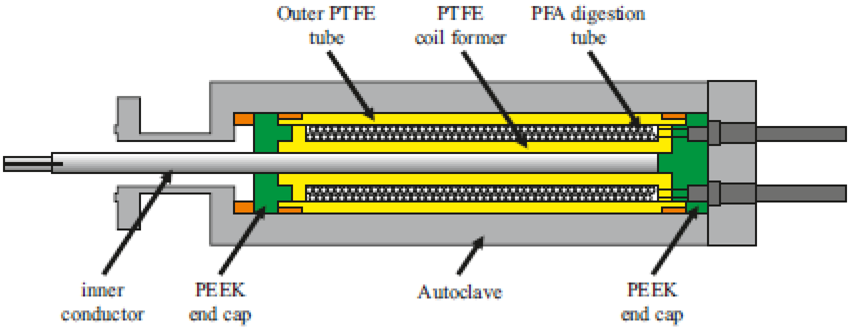

Figure 2.8: Schematic of the coaxial high-pressure reactor

Figure 2.9: Picture of the assembled digestion tube coiled around the coil former, the PTFE outer tube and the PEEK end caps

The microwave energy was supplied by a magnetron (Panasonic 2N244-M16, 1000 W), which was connected to the Multiwave 3000 for the required anode voltage (4350 V) and filament voltage (3.2 V). The second high-voltage transformer of the

Multiwave 3000 was disconnected to avoid a power splitting between the magnetrons and enable a correct power reading.

A coaxial magnetron launcher (CMLD 1.1, S-Team, Slovakia) was used to couple the energy of the magnetron to the inner conductor. The HF-diodes of this launcher were in turn connected to an oscilloscope (DS1104Z-S, Rigol, China) via two coaxial cables. This enabled the measurement of forward and reflected power. For safety reasons the autoclave and the launcher/magnetron part were separated by a 3 mm thick aluminium sheet. Furthermore, the two parts combined were also encased in an aluminium box (3 mm wall thickness).

Figure 2.10 and Figure 2.11 show the mounted setup as well as the cooling units around the steel rods (two peltier elements, 30 W each) and the digestion tube exit port.

Figure 2.10: Upper part of the setup including the autoclave, launcher and magnetron

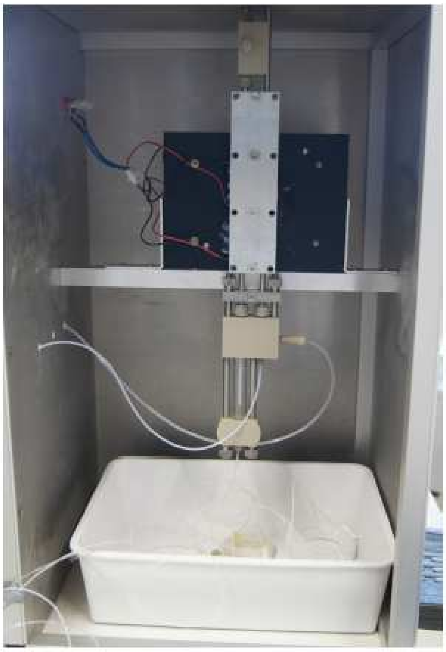

Figure 2.11: Lower part of the setup including the cooling unit, steel rods and digestion tube exit port

Instrumentation and reagents

For the measurement of the digested samples the same axially viewed ICP-OES (Ciros Vision EOP, Spectro, Germany) has been used as with the glass tube and coil reactors. To compare the results the same samples were also digested in a batch system (Multiwave 3000, Anton Paar, Austria) using ceramic supported PFA digestion vessels (rotor type HF, 40 bar maximum pressure). The digestion program was the following: ramp of 10 minutes to 1400 W and holding it for 20 minutes. A vector network analyser (ZVL6, Rohde & Schwarz, Germany) was used to characterize and tune the microwave of the coaxial setup.

Reagents used were the following: purified water (18 MΩ cm, Barnstaed Nanopur, Thermo Fisher Scientiffic, USA), HNO_3 (purified by subboiling), HCl (Suprapur, Merck, Germany), multi element stock solution ($100\,mg\,L^{-1}$, Roth, Germany) and potassium hydrogen phthalate (PA quality, Merck, Germany).

The stock solution as well as the potassium hydrogen phthalate were used for the liquid calibration.

The acid digestion cocktails were either solely HNO_3 ($6\,mol\,L^{-1}$) or a mixture of HNO_3 ($6\,mol\,L^{-1}$) and HCl ($0.4\,mol\,L^{-1}$). Slurries with 1% (m/m) solids were prepared in these cocktails. The internal standard was Sc (end concentration 1 mg L^{-1}). The same autosampler with the integrated paddle for homogenization as with the other setups was used. Again 2 mL sample were surrounded by 2 mL nitric acid (6 mol L^{-1}) on both ends in the digestion tube to avoid dilution with the carrier solution. A flow of 2.5 mL min^{-1} and 250 W microwave power were used.

2.2.2 Results and discussion

Microwave characterization

Figure 2.12 shows a computer simulation (HFSS, Ansys Inc. USA) of the electric field distribution inside the autoclave. Areas of high field intensity are easy to see.

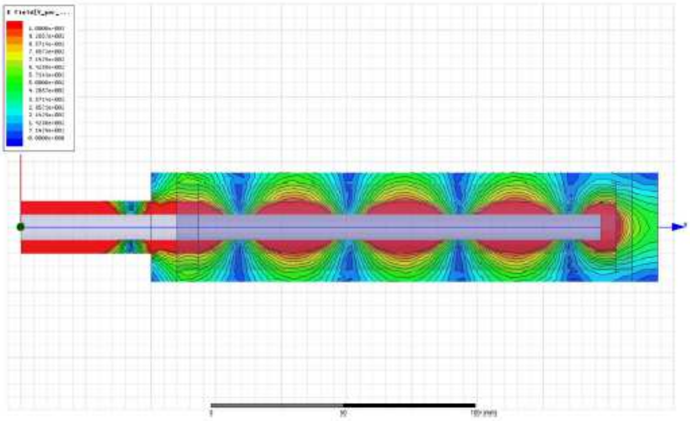

Figure 2.12: Computer simulation of the electric field in the titanium autoclave

The field distribution and resulting absorption of the microwave power is dependent not only on the inner geometry of the autoclave and the tube length, but also on the sample introduced. For reference the coaxial reactor was tuned for a maximum absorption at 2.45 GHz with nitric acid (0.5 mol L-1). This was done by adjusting the position of the inner conduction inside the cavity.

To see how the medium inside the reaction tube affects the measurement, several absorption profiles were created. Water was used as a reference.

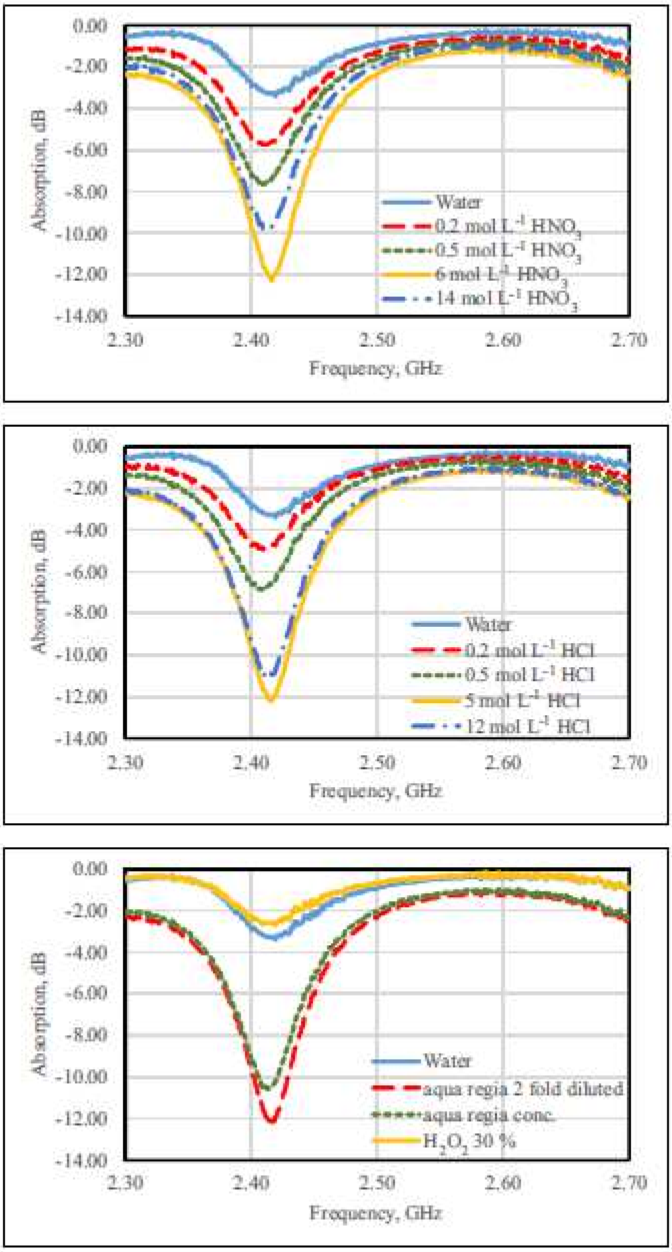

Figure 2.13: Microwave absorption spectra for nitric acid, hydrochloric acid, aqua regia and hydrogen peroxide

Figure 2.13 shows that for both, nitric and hydrochloric acid, the absorption maximum is not synonymous with the highest concentration. At the absorption maximum a slight shift of 7 MHz and 8 MHz respectively is observed. The same dependency on the concentration can be found for aqua regia, while hydrogen peroxide behaves similar to water.

The differences in the absorption efficiency leads to the assumption that a dependence on the conductivity of a medium is present. This is shown in the figures below.

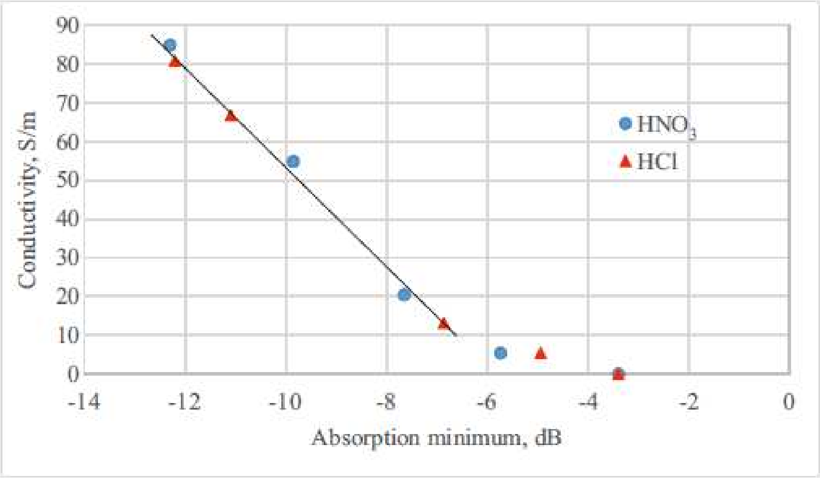

Figure 2.14: Microwave absorption of nitric and hydrochloric acid in regards to the conductivity

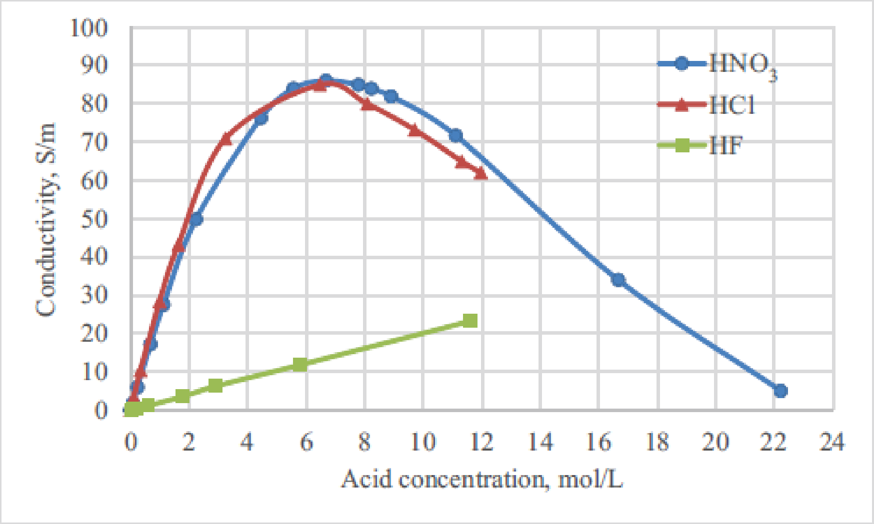

Figure 2.15: Correlation between acid concentration and conductivity of HNO_3, HCl and HF, data compiled from [75]

The shown dependency between the concentration and the conductivity correlates very well with the found dependency between the concentration and the absorption. Originally it was thought that by increasing the electric field strength the absorption efficiency would automatically increase. The gained data however, implicate that above a conductivity of ~10 S m^{-1} the heating of a liquid sample is no longer dominated by the dielectric heating (E field). In that case induction by the H field is most likely responsible for increasing temperatures.

Optimization

Similar to the other two reactors, efficiency of the setup has been controlled by measuring the RCCs of digested glucose, nicotinic acid and L-phenylalanine. While glucose is easy to digest, it also correlates with the generation of large volumes of reaction gasses. Nicotinic acid and L-phenylalanine however are samples, which are difficult to digest completely.

For glucose a relatively high RCC is found (see Figure 2.16), especially considering that the concentration of glucose was significantly lower, than in the other two reactor systems (2 g L^{-1} compared with 25 g L^{-1}).

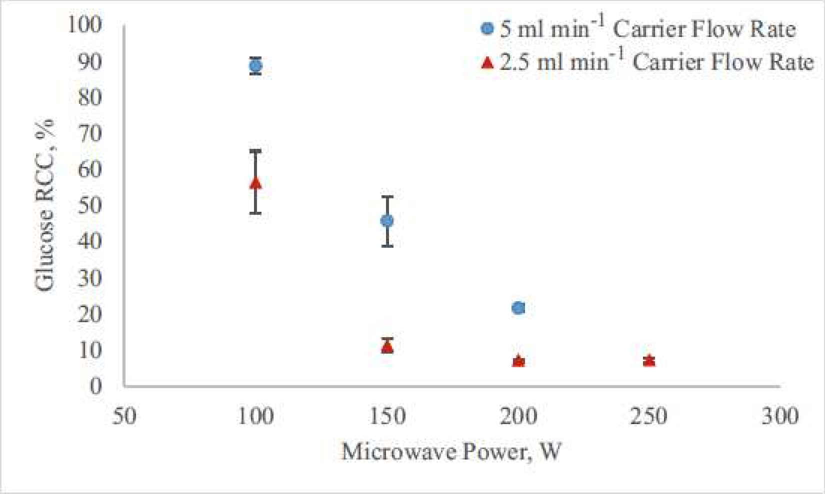

Figure 2.16: RCC of a digested glucose solution (2 g L^{-1}) at the flow rates of 2.5 and 5 mL min^{-1}, n=3

The results in the figure above show that a slower carrier flow rate corresponds with a lower RCC. As this also means a longer residence time in the heated zone it is expected. What is surprisingly however, is the gradually decrease of the RCC with increasing microwave power. In contrast to that, while using the previous reactors a sharp drop of the RCC at certain power levels could be found.

The RCC of nicotinic acid at 200 W and also at 250 W is around 95 %. For L-phenylalanine a very small difference between the two power levels can be found with ~88 % and ~82 % RCC respectively. The samples contained 2 g L^{-1} nicotinic acid or L-phenylalanine and were measured with a flow rate of 2.5 mL min^{-1}.

Reflected microwave power

Excessive and increasing magnetron temperatures during a measurement indicated a severe amount of reflected power. To prove that, the forward and reflected power of one magnetron pulse were measured. Due to the inner workings of the Multiwave 3000, the actually emitted peak power is around twice the desired average power.

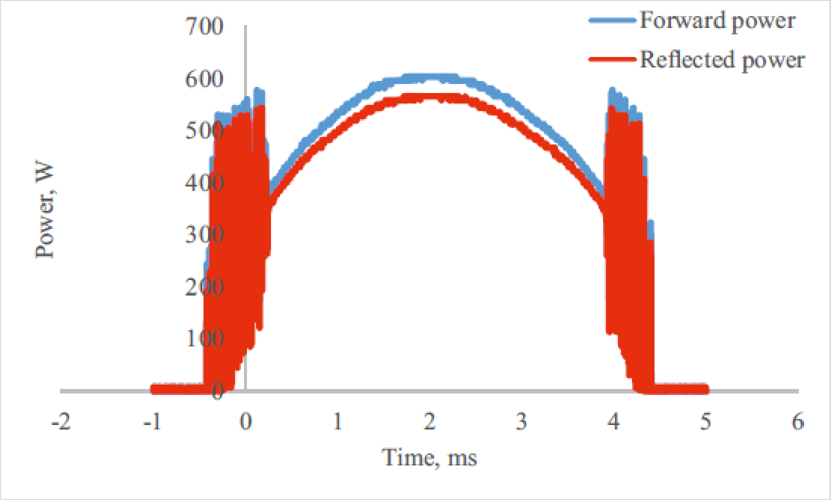

Figure 2.17: Forward and reflected power of one microwave pulse, 200 W average power

The signal noise at the beginning and the end of the pulse indicate an instability of the microwave output. The anode voltage in that region is not sufficient for a stable microwave output. In Figure 2.17 it is easy to see that the amount of reflected power is way too high. Only about 60 to 70 W were absorbed by the sample and/or reactor material (at an average power of 200 W). This explains the poor digestion performance as shown by the high RCCs found.

As the network analyzer predicted otherwise, the high amount of reflected power is quite surprising. With further computer simulations an explanation could be found. It has been reported that an E filed has to be tangentially oriented in regard to the digestion tube to assure an energy transfer [76]. The only part in the coaxial setup where the tube is oriented tangential to the field is the in- and outlet of the tube (approximately 10 cm each), as that’s the only part where it is parallel to the inner conductor. The windings of the tube are only affected marginally. Consequently, the heating of the sample takes place just at the beginning of the digestion tube, as well as at the outlet-part, with a cooling phase in between. As it has been noted before, above a conductivity of ~10 S m^{-1} the E field isn´t dominating the heating. That also means that the dependency on the field orientation is different for every sample.

2.2.3 Conclusion and Outlook

The high-pressure coaxial setup, while analytically not as successful as expected, provided very important insights. The results showed a clear correlation between absorption efficiency and sample conductivity. Furthermore, it isn´t enough to just increase the electric field strength, but also the orientation of the field has a significant impact on the digestion.

To conclude, a successful improvement of the original flow digestion setup with the glass coil reactor has been done. Unfortunately, as the coaxial cavity didn´t work so well, the original idea to couple the underwater laser ablation system, which was explained in chapter 1, to the flow digestion setup couldn´t be carried out. Furthermore, additional experiments with the underwater laser ablation system needs to be done, as it improves the performance in some ways, but in others there are still major problems.

3 Signal enhancement

Since the first development of an ICP-MS and ICP-OES a lot of investigations has been done to figure out which parameters effect a measurement. Starting with the generator power, the spectrometers or mass analysers used, the viewing high and so one. But apart from mechanical construction also the sample composition and the gasses used have a great influence on the results.
In the following two chapters first the influence of additional carbon and bromine content in the sample or the gaseous part is investigated and described, then the addition of oxygen or nitrogen to the nebulizer or intermediate gas flow.

3.1 Matrix effects of carbon and bromine in inductively coupled plasma optical emission spectrometry[63]

Helmar Wiltsche, Monika Winkler and Paul Tirk

This chapter was published under the title shown above in the Journal of Analytical Atomic Spectrometry, Volume 30 (2015), pages 2223–2234; DOI: 10.1039/C5JA00237K

3.1.1 Abstract

In inductively-coupled plasma (ICP) based techniques the signal enhancing effect of carbon on some elements like arsenic or selenium is well documented. However, there is a large spread in the reported magnitude of this effect and whether it can be observed for other elements too. In this investigation we studied the effect of larger amounts of carbon on a total of 157 emission lines of 36 elements. A strong instrument dependence of the "carbon enhancement effect" was encountered in inductively-coupled plasma optical emission spectrometry (ICP-OES), despite the use of the same sample solutions and the same sample introduction system. Several potential enhancement sources (carbon in the form of methanol, phenylalanine and CO_2 as well as bromine) were compared. By tapping the high voltage power supply of the RF generator, current and voltage fed to the power oscillator could be recorded simultaneously with the emission line signal. From these data it was concluded that

the carbon-based matrix effect is a combination of five factors: (1) depending on the source of carbon, changes in the sample nebulization; (2) carbon induced charge exchange reactions; (3) plasma impedance changes caused by the introduction of large quantities of carbon into the ICP: depending on the RF generator used, this effect causes power regulation problems and results in higher RF power coupled to the discharge; (4) thermal pinch effect – the ICP discharge shrinks and becomes smaller; (5) the state of matter (gaseous or liquid) of the introduced carbon sources is relevant to the magnitude of the carbon enhancement effect.

3.1.2 Introduction

The introduction of larger quantities of carbon into the inductively-coupled plasma (ICP) instrument is reported to increase the sensitivity of elements with the ionization potential (IP) in the range of about 9 to 12 eV [77–90]. This enhancement has been observed in both inductively-coupled plasma optical emission spectrometry (ICP-OES) and inductively-coupled plasma mass spectrometry (ICP-MS). Although this "carbon enhancement effect" was reported nearly 25 years ago [77], the understanding of the underlying mechanism is still unsatisfactory as apparent from the many conflicting results published since then.

By far the largest number of studies describing the "carbon enhancement effect" have been performed using ICP-MS as the speciation analysis of As and Se received great attention and these two elements exhibit in general the largest enhancement by carbon. The differences in the attained level of enhancement are striking: whereas some authors reported a carbon induced suppression of the As and Se signal in the range of 50-70 % (1350 W RF power, 2 v/v methanol) [84], most authors observed a signal enhancement by a factor of 2-5 (*e.g.* ref. [81–83,85,89,91,92]). Even an 11-fold enhancement of the Se-signal has been reported [90]. Indeed, it is difficult to compare these data as different sources of carbon were used. Several authors [89,91,92] concluded that the change in nebulization efficiency caused by C-sources such as methanol cannot explain the carbon induced signal enhancement, particularly when considering that the same effect is caused by glycerin [77,92], glucose [91], ammonium acetate [91] and urea [93]. By using methane as the carbon source Allain et al. [77] confirmed that differences in the nebulization efficiency are not the sole reason for the "carbon enhancement effect". Despite the different carbon sources used, most authors [77,78,80,81,83–85,89] found that in ICP-MS the As and Se signal initially increases with increasing carbon content of the sample solution, and then reaches a plateau and decreases again. The maximum enhancement of As and Se appears to be a function of the carbon source and of the instrument used.

The reports on the enhancement or suppression of other elements by carbon are even more confusing. Whereas for Au (IP 9.23 eV) [77,89,94] and Be (IP 9.32 eV) [80] carbon induced signal enhancement is reported, for Zn (IP 9.39 eV), S (IP 10.36 eV), Hg (IP 10.44 eV) and I (IP 10.45 eV) both carbon induced enhancement [77,80,81,83,89,91–93] and the absence of this effect [77,88,92] are reported.

Fewer authors have so far investigated the carbon enhancement effect in ICP-OES. Machát *et al.* [87] found that the small spectral interference on the Se I 196.026 nm emission line is caused by CO band emission. The authors noted an instrument dependent enhancement of Se by 20 to 58 % when 10 g L^{-1} C (glycerol; data corrected for nebulization efficiency changes) was introduced into the ICP and that As and Te were enhanced too. Moreover, they found that S, P and Br (from H_2SO_4, H_3PO_4 and HBr, respectively) enhanced the signals of As, Se and Te significantly. Grindlay *et al.* [79] investigated the carbon-related matrix effect and found As and Se enhanced by up to 30 % in the presence of 20 g L^{-1} C from citric acid. Simultaneously low excitation energy atomic lines (EP < 6 eV) were suppressed by up to 15 %, while ionic lines remained unaffected.

A thorough discussion about the potential mechanism behind the "carbon enhancement effect" is given only in few publications. Abou-Shakra *et al.* [95] proposed a charge exchange mechanism between C^+ and selenium atoms. According to this hypothesis, excited Se^+ ($4p^3$ $2D^0$) is formed whose upper level energy of 1098 kJ mol_{-1} is sufficiently close to the IP of carbon (1086 kJ mol_{-1}). Thereby, both the enhancement in ICP-OES and ICP-MS could be explained. Grindlay et al. [92] extended and refined this theory further, as a charge transfer reaction requires not only the minimum energy difference between the involved levels, but obliges the fulfillment of the Wigner spin conservation rule. The authors determined by ICP-MS that the dominant carbon species in the ICP are C^+ and CO^+ and concluded that a high charge transfer probability exists for As, Au, Hg, I, Ir, Os, P, Pt, S, Sb, Se, Te, and Pd. Experimentally Grindlay *et al.* found a carbon induced signal enhancement only for As, Au, Hg, I, Sb, Se, and Te.

As listed above, reports on the carbon enhancement effect presented in the literature rely heavily on ICP-MS data. Particularly for mechanistic studies, the lack of additional information on fundamental plasma parameters such as electron number densities or ionization temperature is unsatisfying. The processes happening in the interface region are another source of potential bias for mechanistic studies: just behind the sample cone a supersonic jet is formed, wherein the broad velocity distribution of atoms from the ICP is turned into a much narrower one, centered around the velocity of Ar [96]. Moreover, this zone is a source of collisions and reactions between the constituents of the expanding gas. It seems not entirely unlikely that, in parts, the large differences in the signal enhancement of As and Se observed for different ICP-MS instruments are caused in this region, as carbon is added in a very high concentration. Another factor that could cause additional bias when studying the carbon enhancement effect is the reported shift of the region of maximum ion density in the ICP [85,97] that necessitates the readjustment of the sampling depth. Particularly for ICP-MS instruments that alter the sampling depth by changing the nebulizer gas flow, additional bias from different nebulized sample masses might be introduced.

The situation is different for ICP-OES: once the radiation is emitted from an excited state, the factors that could affect the signal thereafter are minute compared to the expansion of a hot atmospheric pressure plasma into the high vacuum of the mass spectrometer, the associated supersonic expansion and charge separation. Particularly for axially viewed ICP-OESs slight changes in the zone of maximum excitation will not affect the overall signal intensity as much as in ICP-MS, as the observed region inside the normal analytical zone will be averaged by the optical setup.

The aim of this work is to provide insights into the factors that affect the signal enhancement of high IP elements by carbon in the ICP in order to distinguish between spectroscopic and instrumental effects. As apparent by the foregoing discussion, ICP-OES was mainly used for this purpose.

3.1.3 Experimental

3.1.3.1 Instrumentation

An axially viewed ICP-OES (CIROS Vision EOP, Spectro, Germany) with a fixed viewing depth was used in this work. The instrument dependence of the investigated effect was also studied using two other ICP-OESs (Optima 3000 XL and Optima 5300 DV; both PerkinElmer, USA) under instrument conditions comparable to those provided in Table 3.1 as well as one ICP-MS (Elan DRC+, PerkinElmer, USA). The ICP-OES operating conditions listed in Table 3.1 are compromise conditions for multi-element analysis. They were optimized for aqueous (3 % v/v HNO_3) solutions for the highest signal to background ratio for the observed emission lines of As, Ca, Cl, Fe, P, S, Se, and Zn.

A 4-turn probe coil connected to a frequency counter (TF930, TTi Thurlby Thandar Instruments Limited, UK) recorded the frequency response of the free running RF generator. Details of this setup were published previously [98].

Table 3.1: ICP-OES operating conditions (CIROS Vision EOP, Specto, Germany)

Spectrometer	Paschen-Runge mount with [99] charge-coupled device (CCD) line-detectors
RF generator	27 MHz, free running Huth-Kühn [99] type power oscillator; also known as the tuned plate tuned grid oscillator [100]
Plasma power, W	1350
Outer gas flow, L min^{-1}	12
Intermediate gas flow, L min^{-1}	0.6
Nebulizer gas flow, L min^{-1}	0.83
Sample flow rate, mL min^{-1}	1.8
ICP torch	Standard torch with 2.5 mm ID injector; fixed (one piece) torch
Nebulizer	Cross-flow
Spray chamber	Scott type
Number of measurements	4
Integration time, s	24

Current and voltage delivered to the RF generator were constantly recorded by taping the low voltage control lines between the high voltage power supply (HV-PSU) and the generator control board with analog-digital converters (ADCs). These control lines provide voltages proportional to the output current (1 V ≡ 200 mA) and output voltage (1 V ≡ 1000 V) of the HV-PSU. Four 16 bit ADCs (ADS1115, Texas Instrument) controlled by a microcontroller (ATSAM3X8E on an “Arduino Due - open source electronics prototyping platform”; https://www.arduino.cc) delivered 475 samples/second for each channel to the control PC. The schematic of the ADC board is shown in the ESI1 of this article. As the ADS1115 includes a programmable gain amplifier, no operational amplifier buffer stage was deemed necessary and the connection to the HV-PSU control lines was made directly with a 10 kΩ resistor. The ADC board fulfilled the noise-, gain- and drift-specifications given in the ADS1115 datasheet. However, due to the lethal voltage present at the HV-PSU output, no attempt was made to check the factory calibration between the high voltage output and the low voltage control lines.

The nebulization efficiency and mass flow of samples introduced into the ICP were determined using the well-established method of continuous weighing [101]. Contrary to the setup employed previously for this purpose [102] two beakers located at the balance were used rather than one: the first beaker contained the sample solution whereas the second was used to collect the liquid returned from the spray chamber. Thereby the density of each solution could be measured independently with a density meter (DMA4500, Anton Paar, Austria).

An external thermal-based mass flow controller (100 sccm, Mass-Flo 1179, MKS Instruments, Germany) controlled the flow of CO_2. The appropriate gas correction factor was used to correct the response of the nitrogen calibrated mass flow controller for the different physical properties of CO_2 as recommended by the manufacturer.

3.1.3.2 Reagents

Purified water (18 MΩ cm, Barnstead Nanopure, Thermo Fisher Scientific, USA) and high purity acids (HNO_3, purified by sub-boiling) were used throughout. Standard solutions were prepared from a 100 mg L^{-1} multi-element stock solution (Al, Ag, As, B, Ba, Be, Bi, Ca, Cd, Co, Cr, Cu, Fe, K, Li, Mg, Mn, Mo, Na, Ni, Pb, Sb, Se, Sr, Ti, Tl, V, and Zn, Roth, Germany), several 1 g L^{-1} single element stock solutions (As, Au, B, Bi, Hg, Pb, Se: Merck, Germany; Br, S, P: SCP Science, USA) and in the case of I from KIO_3 (pa, Merck, Germany) by dilution with 3 % HNO_3 (v/v). The ICP excitation temperature was determined using a 300 mg L^{-1} Fe solution containing 3 % HNO_3 (v/v) prepared from a 10 g L^{-1} Fe single element stock solution (Alfa Aesar, Germany). Water saturated with bromine was prepared by equilibration of high purity water with Br_2 (Sigma Aldrich, ACS reagent, Germany) for one week in a dark glass bottle. Methanol (Normapur, VWR, Germany), NaCl (Fluka, Germany), and phenylalanine (f. biochemistry, Merck, Germany) dissolved in 3 % (v/v) HNO_3 were used to study plasma-based matrix effects. Argon was of 5.0 quality (Messer, Austria) and carbon dioxide of Biogen C quality (Linde, Austria).

3.1.3.3 Optical emission-based plasma diagnostics

The magnesium ion to atom ratio (plasma robustness criteria [103]) was calculated from the Mg II 280.270 nm/Mg I 285.213 nm emission line intensity ratio using a 10 mg L^{-1} Mg solution.

The Boltzmann plot method [104] was used to determine the Fe(I) excitation temperature T_{exc}. Details on the emission lines used and fundamental constants are reported elsewhere [98].

3.1.3.4 Experimental procedure and processing of the spectra

In order to record a consistent set of data, the effects of gaseous (CO_2) and liquid reagents (Br_2, aqueous solutions (3 % v/v HNO_3) of NaCl or phenylalanine, or methanol) were investigated using a standardized procedure with five test standards: after recording the blank spectra, standard solutions 1 to 4 were measured. Between the samples, the sample introduction system was rinsed with diluted nitric acid (3 % v/v) for 60 seconds. The elements and their concentrations in each standard solution were: solution 1: 2 mg L^{-1} of Al, Be, Ca, Cd, Co, Cr, Cu, Fe, K, Li, Mg, Mn, Mo, Na, Ni, Sb, Sr, Ti, Tl, V, Zn, 10 mg L^{-1} of B, Bi, Pb, and 20 mg L^{-1} As and Se; solution 2: 10 mg L^{-1} of Au, Br, Hg, P, S; solution 3: 30 mg L^{-1} I; solution 4: 300 mg L^{-1} Fe.

Gases were added either to the intermediate gas stream of the ICP torch using a small T-piece, or to the spray chamber through a 2 mm ID PTFE tube. For experiments with liquid reagents, the aforementioned four test standards and a blank solution were prepared from the appropriately diluted reagent (methanol, water saturated with Br_2, solutions of NaCl or phenylalanine) and the relevant single or multi-element stock solution.

All analyte signals were normalized to the aqueous standard (3 % v/v HNO_3) using the following procedure: background correction was applied to all spectra. In the first step of the data treatment, the emission signals of the blank solutions for each reagent concentration level were compared with the emission signals of the respective analyte-containing standard. If the signal in the blank solution was larger than 10 % of the uncorrected standard, the line was rejected for further processing, as a spectral interference could not be excluded. Otherwise, if the emission signal passed this criterion, the blank signal was subtracted from the analyte signal and the data were then normalized to the respective aqueous signal (3 % v/v HNO_3).

3.1.4 Results and discussion

3.1.4.1 Repeatability of the excitation temperature determination

The interpretation of the results presented in this work relies heavily on the excitation temperature of Fe(I) determined by the Boltzmann plot method. Particularly when comparing data recorded over a period of about one month, the repeatability of the excitation temperature (T_{exc}) is of vital importance. It is important to note that the T_{exc} reported here represents an average temperature of the region in the ICP that is observed by the spectrometer.

The excitation temperature of Fe(I) was determined on four consecutive days. Before recording the emission spectra the RF generator was allowed to "warm up" for 30 min [98]. The excitation temperature was 6470 ± 15 K, 6450 ± 20 K, 6450 ± 10 K, 6460 ± 10 K (mean value ± s; n = 5) using the plasma conditions listed in Table 3.1. Then the ICP torch was removed, acid cleaned, reinstalled and the excitation temperature was again recorded on the following days: 6530 ± 20 K, 6540 ± 20 K, 6520 ± 20 K, 6520 ± 10 K. After installing the torch again, the observation position of the spectrometer was tuned following the instrument manufacturer's recommendations and similar signal intensities were obtained for the Mn tuning solution. Simultaneously with the observed small change of the excitation temperature, the plasma robustness increased slightly from 6.8 ± 0.1 to 7.0 ± 0.1 when the torch position was slightly altered in the cause of the cleaning process.

The significant difference in the excitation temperature before and after the torch cleaning can be attributed to small changes in the position of the ICP torch within the load coil. Clearly, any investigation on the effect of an external parameter must be recorded without removing or changing the ICP torch, as otherwise an uncontrolled experimental bias is introduced. It is important to note that in the instrument used there is no mechanical indicator for the torch alignment but only the recommendation to introduce the torch into the load coil until the distance between the inner glass tube and the first turn of the load coil is 1 mm. Although for the experiment reported above the exact position of the torch was not determined, a later investigation with a caliper indicated a positioning repeatability of about ± 0.2 mm.

It seems also important to note that the precision of the excitation temperature determination was very high: for five independent recordings the standard deviation was always found to be between 10 and 20 K. The uncertainty of the slope of the least square fitted line in the Boltzmann plot was about 100 K. As both the short term (5 repetitions) as well as the long term (4 consecutive days) precision of the excitation temperature determination were much higher, it must be concluded that the uncertainty of the slope in the Boltzmann plot is dominated by the uncertainty of the transition probability data. Consequently, the absolute value of the reported excitation temperatures might be biased, but relative changes can be expected to be identified correctly.

3.1.4.2 Instrumental dependence of the effect of carbon on the signal of Se

When comparing the degree of enhancement of Se by carbon reported in the literature, the differences in the magnitude of the enhancements are striking, though the various experimental conditions and reagents make a direct comparison difficult. The effect of methanol (0-10 % m/m) on selenium was investigated on three different ICP-OESs and one ICP-MS instruments. As the torch geometries of these instruments are different, it was not possible to maintain similar outer- and intermediate gas flows. Consequently, these flow rates were selected to match typical conditions used for the analysis of aqueous (diluted HNO_3) samples: both Optima instruments were operated at 15 L min^{-1} outer gas flow and 0.5 L min^{-1} intermediate gas flow; the ICP-MS used 15 L min^{-1} outer gas flow and 1.3 L min^{-1} intermediate gas flow. The RF power, nebulizer gas flow and sample flow rate were kept constant as listed in Table 3.1, as well as the nebulizer and spray chamber. Thereby comparable experimental conditions were achieved as evident from the similar plasma robustness (Mg II 280.270 nm/Mg I 285.213 nm ratio in 3 % v/v HNO_3) that were 7.0 ± 0.1, 6.8 ± 0.1 and 6.5 ± 0.1 for the Spectro CIROS Vision, PerkinElmer Optima 3000 XL and Optima 5300 DV (the data of the two Optima instruments were corrected for differences in the spectrometers' echelle grating efficiency by applying the correction factor 1.85 to the Mg-ratio [105,106]).

For the ICP-MS experiment, the nebulizer gas flow was optimized for maximum signal intensity in an aqueous solution (3 % v/v HNO_3).

The differences in the instrument dependent effect of carbon are shown in Figure 3.1.

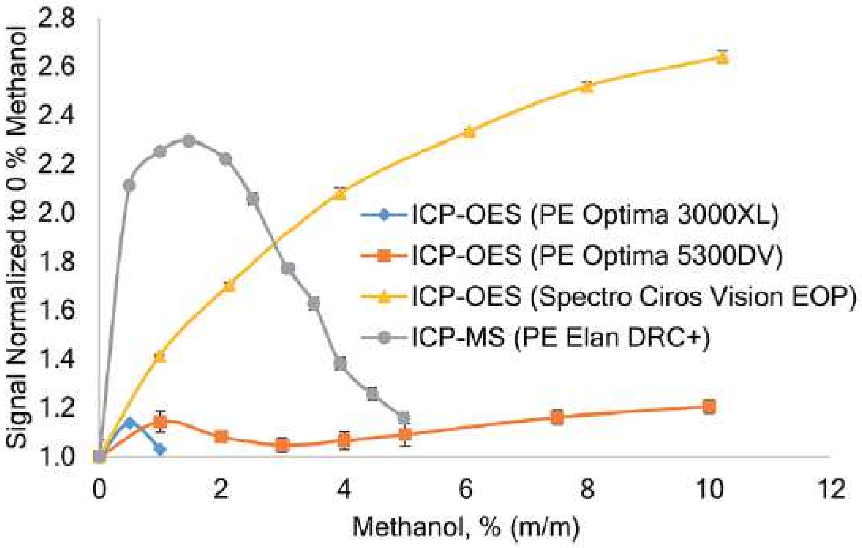

Figure 3.1: Effect of increasing methanol concentration on the signal of Se in ICP-OES (Se 203.985 nm) and ICP-MS (m/z=78) recorded on different instruments. The Se concentration was 10 mg L^{-1} in ICP-OES and 10 µg L^{-1} in ICP-MS. No internal standard was used; the Einzel-lens of the ICP-MS was tuned for aqueous solutions. Error bars: standard deviation, n=5.

In ICP-MS the ^{78}Se signal first increased by a factor of up to 2.3 at 1.5 % (m/m) methanol and then decreased again. This pattern is consistent with ICP-MS data reported by other authors [78,80,85,91], though the maximum enhancement factor and the corresponding methanol concentration appear to differ from instrument to instrument.

A different behavior was recorded on the three ICP-OES instruments investigated: PerkinElmer Optima 3000XL showed little tolerance to increased methanol load to the plasma and above 1 % (m/m) methanol the ICP extinguished. Interestingly, only a rather small Se signal enhancement of 14 % was recorded on this instrument at 0.5 % (m/m) methanol. Using a PerkinElmer Optima 5300DV (axially viewed), the ICP discharge was stable up to a maximum methanol concentration of 10 % (using a 1.8 mm ID injector tube), but the enhancement of selenium was only 20 % at the highest methanol concentration tested.

Using the Spectro Ciros Vision EOP ICP-OES, a steady and large signal enhancement of Se was encountered. At 10 % (m/m) methanol a signal enhancement by a factor of 2.6 was observed for Se I 203.985 nm. This enhancement was consistent on all investigated Se emission lines and factors of 2.5 and 2.2 were recorded for Se I 196.090 nm and Se I 207.479 nm, respectively.

Machát *et al.* [87] also encountered different Se enhancement factors on different ICP-OES instruments, but different sample introduction systems were used.

3.1.4.3 Effect of methanol

As the Spectro Ciros Vision ICP-OES showed the largest enhancement of Se and allowed the simultaneous acquisition of the entire relevant spectrum, this instrument was used for further investigations. A total of 157 emission lines of 36 elements were investigated. Table 3.2 lists the effect of 10 % (m/m) methanol on selected lines. The data can be classified broadly into four groups.

The first group of emission lines was suppressed by about 10-20 % and includes some ion lines of Ba and Sr as well as some atom lines of Mn, Na and Ni. These lines have a very low excitation potential (2-3 eV) in common.

The effect of methanol was small on the second group of elements (enhancement by a factor of 0.9 to 1.1). In general, the excitation energies of atom lines in this group were between 3 and 5 eV. For ion lines the total line energy (ionization + excitation energy) was between 9 and 11 eV.

The third group of emission lines was enhanced by about 20-50 %. The excitation energy of these lines was in general between 5 and 6 eV and the total line energy of ion lines was between 11 and 14 eV.

Signal enhancements compared to an aqueous solution (3 % v/v HNO_3) of more than 50 % were observed for atom lines with an excitation potential greater than 6 eV and for some high energy ion lines in the region of about 15.5 eV. This fourth group included the atom lines of Ar, As, Br, Cl, I, P, S, and Se as well as some high energy ion lines of Ag, Cd, Tl, and Zn.

It is important to note that the listed energy ranges of the four groups are not sharply defined and that some emission lines do not follow the listed general trend. Moreover, there is no clear correlation between the total line energy (excitation potential for atom lines) and the enhancement, but only a trend.

Table 3.2: Signal enhancement/suppression factors (emission line signal obtained in the given reagent divided by the signal obtained in 3 % v/v HNO_3) of selected emission lines by various reagents. A complete list of 157 emission lines of 36 elements is available in the ESI. ND: not determined; Int: spectral interference defined as blank signal >10 % of the signal in the analyte containing solution before blank subtraction; RSD<3 % for all emission lines; for an aqueous solution (3 % v/v HNO_3) the plasma robustness was 7.0 ± 0.1 and the excitation temperature T_{exc} was 6610 ± 20 K

Emission line, nm	**Total line energy, eV**	**Methanol 10 %**	**Phenylalanine 8 g L^{-1} C**	**15 sccm CO_2 added to the aerosol gas stream**	**15 sccm CO_2 added to the intermediate gas flow**	**Br_2 34 g L^{-1}**	**NaCl 30 g L^{-1}**
Al I 396.152	3.14	1.00	0.98	0.76	1.27	1.06	0.79
Al II 167.078	13.41	1.50	1.02	1.04	1.83	0.95	0.69
Ar I 404.442	14.69	1.97	0.98	1.36	2.49	0.88	0.90
As I 197.262	6.29	1.92	1.08	1.47	1.98	1.03	0.84
As I 189.042	6.56	1.97	1.08	1.52	2.08	1.04	0.83
As I 193.759	6.40	1.90	1.07	1.48	2.01	1.04	0.84
Au I 267.595	4.63	1.09	1.00	0.89	1.17	1.02	0.82
Au I 242.795	5.11	1.18	1.00	0.92	1.25	1.03	0.81
B I 249.773	4.96	1.16	0.97	0.94	1.26	1.01	0.76
Be I 234.861	5.28	1.18	0.99	0.93	1.28	0.96	0.75
Be II 313.042	13.28	1.42	1.08	1.07	1.40	1.05	0.66
Br I 148.845	8.33	1.57	0.98	0.93	1.59	ND	ND
Br I 144.99	8.55	Int	0.98	1.05	1.73	ND	ND
Cd I 228.802	5.42	1.31	1.02	0.98	1.44	0.97	0.79
Cd II 214.438	14.77	1.57	1.04	1.07	1.85	0.91	0.67
Cl I 134.724	9.20	1.77	0.99	1.20	2.03	0.83	Int
Co II 230.786	13.75	1.19	1.02	0.85	1.40	0.90	0.65
Cr II 205.552	12.80	1.20	1.03	0.86	1.36	0.95	0.67
Hg I 253.652	4.89	0.97	0.99	0.84	1.12	0.99	0.83
Hg I 184.95	6.70	1.45	1.00	1.16	1.79	0.98	0.85
Hg II 194.227	16.82	1.41	1.01	1.05	1.77	0.91	0.77
I I 183.038	6.77	1.52	1.04	1.20	1.86	Int	0.76
I I 178.276	6.95	1.69	1.05	1.61	2.07	Int	0.83
Mg I 285.213	4.35	1.00	0.96	0.73	1.28	0.95	0.79
Mg II 280.27	12.07	1.14	1.00	0.84	1.35	0.95	0.61
P I 213.618	7.21	2.09	1.03	1.63	2.20	1.14	0.86
P I 169.403	8.73	2.08	1.05	1.71	2.21	1.13	0.81
P I 138.147	8.97	2.00	1.03	1.65	2.16	1.13	0.88
S I 180.731	6.86	1.59	0.97	1.18	Int	1.18	0.94
S I 182.034	6.86	1.64	0.98	1.17	1.67	1.19	0.91
Se I 207.479	5.97	2.24	1.22	1.65	2.37	1.85	0.71
Se I 196.09	6.32	2.51	1.20	1.98	2.89	1.86	0.78
Se I 203.985	6.32	2.64	1.22	2.02	2.97	1.83	0.78
Tl I 276.787	4.48	1.06	0.95	0.79	1.27	1.04	0.81
Tl II 132.171	15.49	2.13	1.03	1.36	2.68	Int	0.72
Zn I 213.856	5.80	1.28	1.01	0.94	1.41	0.93	0.77
Zn II 202.548	15.51	1.81	1.05	1.23	2.10	0.91	0.69
Plasma robustness		8.2 ± 0.1	7.5 ± 0.1	7.8 ± 0.1	7.2 ± 0.1	7.1 ± 0.1	5.4 ± 0.1
T_{exc}, K		6980 ± 10	6590 ± 10	6800 ± 10	6840 ± 20	6550 ± 20	6510 ± 20

The power drawn by the RF generator plotted as a function of the methanol concentration nebulized during the measurement is shown in Figure 3.2.

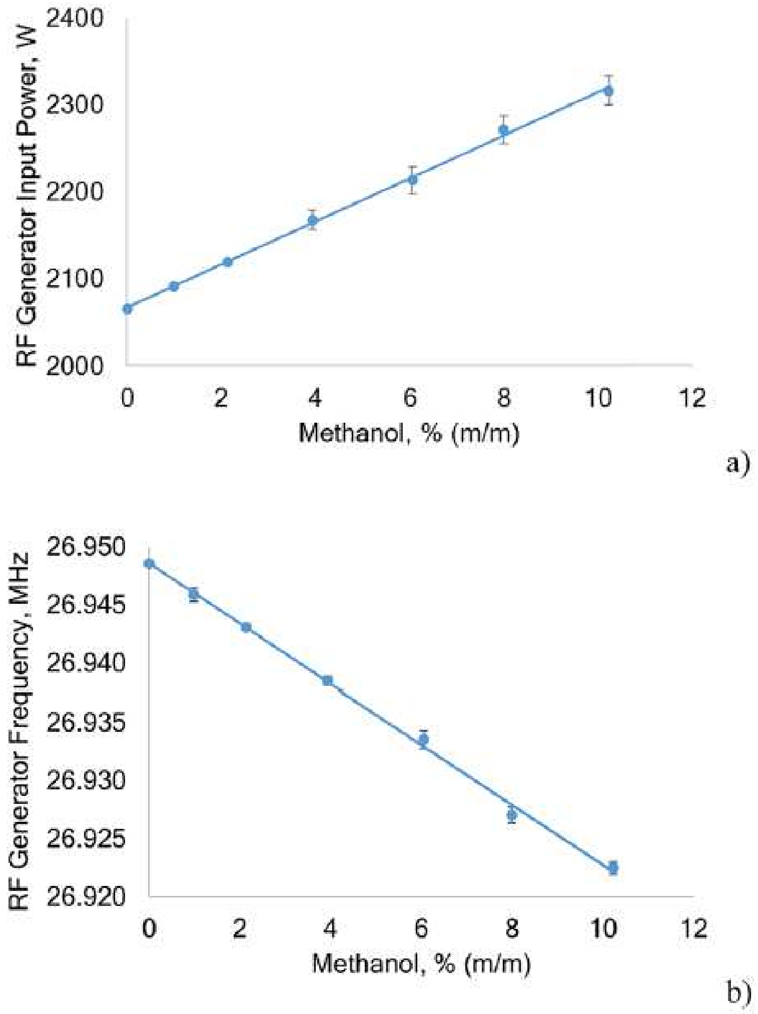

Figure 3.2: Power drawn by the RF generator for a nominal output of 1350 W (a) and frequency of the generator (b) as a function of the methanol concentration nebulized during measurement. The error bars represent the standard deviation of five independent experiments.

The Huth-Kühn type power oscillator used is current controlled. For every RF power level that can be selected in the instrument software, a corresponding current is set by the HV power supply. The current is derived from a factory power calibration. The power oscillator behaves purely resistive during normal operation – Ohm’s law therefore applies and the power drawn by the power oscillator is the product of current (RMS) and voltage (RMS) read directly from the HV power supply.

From Figure 3.2a it is evident that with increasing methanol concentration the power drawn by the RF generator increases significantly (about 250 W when changing from diluted nitric acid (3 % v/v HNO_3) to 10 % methanol). As expected from a current controlled power oscillator, the power vacuum tube plate current remained constant, but the plate voltage increased from 3565 V to 4000 V when the sample solution was switched from 3 % (v/v) HNO_3 to 10 % (m/m) methanol. At the same time the frequency of the power oscillator decreased by 26.1 kHz. It seems interesting to note that for aqueous aerosols an increase of the RF generator power is accompanied by a small increase in the frequency. The observed linear decrease of the RF generator frequency (Figure 3.2b) and the simultaneous linear increase in the power uptake when the methanol concentration in the sample solution is increased indicates destabilization of the plasma as also observed previously [98]. In addition, this can also be concluded from the rising SDs of the plate voltage that increased the SDs of the generator input power when the methanol concentration rose.

The reason for the observed increase of power drawn by the RF generator can be expected to be a significant impedance change of the plasma caused by the large quantities of carbon introduced. However, only a part of the additionally drawn power will be coupled to the plasma, while the rest is converted to heat in the RF generator. The reported increase of power uptake of the RF generator has, to the best of our knowledge, not been reported in the literature. However, Larsen and Stürup [83] noted that "the upper practical RF power input was 1320 W" because otherwise the cooling capacity of the ICP-MS interface would have been exceeded. As aqueous solutions could indeed be analyzed at higher RF power levels, this finding could be attributed to a higher power uptake of the RF generator.

When increasing the methanol concentration in the nebulized sample solution, the ICP was found to shrink in size and withdraw from the injector tip. This thermal pinch effect [107] results in a smaller, brighter discharge. From Figure 3.3 it is evident that by nebulizing 10 % (m/m) methanol, the plasma completely withdrew from the injector region and the plasma base was located just after the second turn of the load coil. Yet, the quantification of this effect is difficult, as the load coil hides the most important region of the ICP.

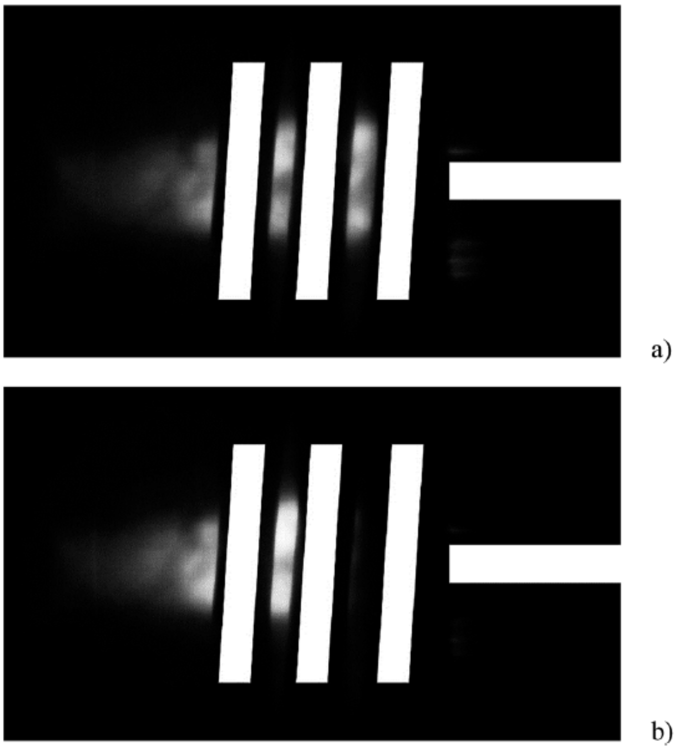

Figure 3.3: Effect of methanol on plasma volume. (a) Introduction of 3% v/v HNO_3; (b) introduction of 10% (m/m) methanol. The positions of the three turns of the load coil and the injector are represented with the white bars for clarity. Both images were recorded under identical photographic conditions (aperture setting, exposure time). Note that in image (b) the plasma withdrew from the space between the first and the second tun of the load coil.

The shifting of the plasma base away from the injector can also be expected to affect the recorded analyte emission intensities: although the plasma was axially viewed and the viewing depth was not changed, the zone within the ICP imaged onto the entrance slit of the spectrometer will follow the shift of the plasma base to some extent. Simultaneously the plasma power density changed the behavior of the emission lines, which is not easily predictable. Chan and Hieftje [108] showed that the magnitude of matrix effects in the ICP is not constant when changing the observed location within the ICP. However, the large focal length of the spectrometer’s entrance optics might reduce this effect when compared to the plasma cross-sections investigated by Chan and Hieftje or radial viewing.

In conclusion, the large quantities of carbon introduced by nebulizing 10 % methanol altered plasma impedance and thereby led to an increase of the power vacuum tube’s plate voltage. This in turn increased the RF power delivered to the ICP. Simultaneously, the plasma decreased in size and became hotter as evident from the rise in the excitation temperature from 6610 ± 20 K (3 % v/v HNO_3) to 6980 ± 10 K (10 % methanol). It is apparent that an increase of RF power delivered to the ICP combined with a decrease of the plasma volume is associated with a change in the analyte emission signal intensity.

While all analyte emission lines that were significantly enhanced by carbon showed a steady signal increase with rising methanol concentration, plasma robustness only increased up to 6 % (m/m) methanol (peak value 8.8) and then decreased again to 8.2 at 10 % (m/m) methanol.

One of the inherent problems of using methanol as the source of carbon is the difficulty of quantifying the exact amount of carbon introduced into the ICP. The density of all methanol containing solutions was measured prior to the introduction into the spray chamber and in the waste solution that left the spray chamber after system equilibration. Moreover, the mass flow of aerosol leaving the spray chamber was determined by the method of continuous weighing. From these data a mass balance was calculated assuming a constant liquid flow rate from the peristaltic pump of 1.82 mL min^{-1}: by subtracting the mass flow of methanol in the drained solution from the mass flow of methanol pumped to the spray chamber the mass flow of methanol introduced into the ICP was calculated. Using this method corrects for differences in aerosol formation and preferential evaporation of methanol from the surface of the spray chamber and aerosol droplets. Mora *et al.* [109] found that the D_{50} (droplet distribution diameter below which 50 % of the cumulative aerosol volume is found) of the primary aerosol of a water–methanol mixture decreases with increasing methanol content of the mixture. However, this effect was found to be rather small (D_{50} changed by 3 %) when comparing water with 10 % methanol.

The carbon mass flow introduced into the ICP increased almost linearly with rising methanol concentration in the sample solution fed to the nebulizer. However, below 4 % (m/m) methanol the function bends, indicating less pronounced vaporization of methanol in the spray chamber. At the maximum concentration of 10 % (m/m) methanol, 8.4 mg min^{-1} carbon was introduced into the ICP. The uncertainty of this calculation was found to be dominated by the method of continuous weighing: whereas the removal of the liquid from the sample beaker was constant with time, the draining of the waste solution was discontinuous, as individual droplets formed on the lower end of the Scott type spray chamber inner tube. Thereby a fluctuating signal was created. The error of the slope was below 6 % for the used recording time of 10 minutes. It is interesting to note that without the described correction for the preferential vaporization of methanol in the spray chamber the mass flow of carbon introduced into the ICP would have been underestimated by a factor of 1.7.

3.1.4.4 Effect of phenylalanine and CO_2

Methanol is a volatile liquid that is introduced into the ICP not only as a liquid contained in the aerosol but also as vapor. Though the total mass flow of methanol transported to the ICP was quantified, we attempted to separate the effects of these two phases on the analyte signal. Firstly, carbon was introduced in the form of a polar, well-soluble but non-volatile substance – phenylalanine was chosen for this purpose. Secondly, a gaseous carbon source (CO_2) was investigated, whereby any nebulization-induced bias could be excluded. CO_2 was added either to the aerosol or to the intermediate gas stream.

As shown in Table 3.2 the effects of these three carbon sources on the investigated analytes are quite different: 8 g L^{-1} carbon introduced into the ICP as phenylalanine did not change the signal intensity of most investigated emission lines by more than 5 %. The only exceptions were As, Be(II), and Se with signal enhancements of 10-20 %. It is also interesting to note that of all carbon containing reagents investigated only phenylalanine did not alter the emission intensity of the Ar I 404.442 nm emission line. Phenylalanine neither changed the excitation temperature significantly nor did it alter the RF generator frequency appreciably (about 1 kHz). The power vacuum tube's plate voltage also remained constant. Combined, these facts suggest that carbon introduced as phenylalanine did not alter the plasma impedance and the enhancement of As, Be(II), and Se is not caused by changes in the ICP itself, as observed when using methanol as the carbon source. It is important to note that the enhancement of As, Be(II), and Se increased with greater phenylalanine concentration in the solution, reaching its maximum at the highest tested reagent concentration (close to the limit of solubility).

In contrast to phenylalanine, CO_2 as the gaseous carbon source showed a markedly different behavior, as listed in Table 3.2. When introduced into the aerosol gas stream, a signal enhancement pattern comparable to that of methanol was recorded, although the signal enhancement factors were between 20 and 40 % lower than when using methanol as the carbon source. The excitation temperature was lower too (6800 ± 10 K vs. 6980 ± 10 K). Similar to methanol, a pronounced thermal pinch effect was observed when increasing the flow of CO_2. The plasma impedance was also found to change, as evident from the higher power vacuum tube plate voltage (at 15 sccm a plate voltage of 3993 V was recorded). The frequency of the power oscillator decreased by 28.9 kHz when switching from 0 to 15 sccm CO_2.

When CO_2 was introduced into the intermediate gas flow of the ICP, 5-20 % higher signal enhancement factors were encountered when compared to methanol, as listed in Table 3.2. The excitation temperature was slightly higher and the plasma robustness was lower. Just as with methanol, when CO_2 was introduced into the aerosol gas stream, a strong thermal pinch effect was observed, which again was accompanied by high plate voltage and frequency excursion (3950 V and 27.4 kHz).

In Figure 3.4a the carbon emission signal (C I 193.091 nm) of the investigated carbon sources is plotted as a function of the carbon mass flow delivered to the ICP. This mass flow was calculated from the determined nebulization efficiency in the case of phenylalanine, or by using the ideal gas law for CO_2. For methanol, the method described above that also includes the preferential vaporization was used.

The emission signals did not increase in a linear fashion as the mass flow of carbon was extremely high. For CO_2 the C emission signal was surprisingly similar, despite the different gas flows it was introduced into. Although below 5.5 mg min^{-1} carbon from CO_2, the C emission signal was higher when introducing the gas into the aerosol stream rather than into the intermediate stream, the difference was only about 30 % at 1 mg min^{-1} and 9 % at 2.7 mg min^{-1}.

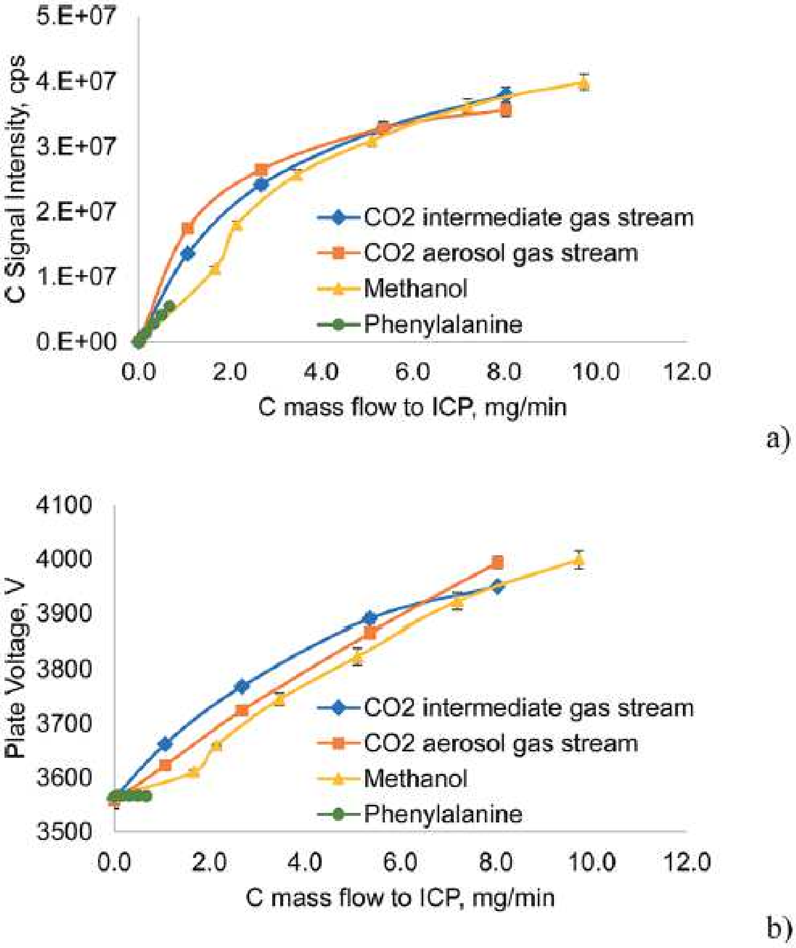

Figure 3.4: Signal intensity of the C I 193.091 nm emission line and power vacuum tube plate voltage as a function of the carbon mass flow introduced into the ICP for the investigated carbon sources. The error bars represent the standard deviation of five independent experiments.

From Figure 3.4b it can be deduced that CO_2 introduced into the intermediate gas stream of the ICP acts stronger on the plasma core than when introduced into the aerosol gas stream, as the power vacuum tube’s plate voltage rises faster due to the impedance changes of the plasma core. As already noted, higher C-loading of the ICP caused the base of the discharge – the region where the aerosol gas stream enters the plasma – to withdraw from the region between the end of the injector tube and the first turn of the load coil (“normal position”) to the space between the first and the second turn of the load coil (thermal pinch effect). The increased distance between the injector tube and the base of the ICP can be expected to allow a higher diffusional exchange between the aerosol and the intermediate gas stream. Thereby the carbon loading is not restricted to one of these streams, explaining the observed effects.

Another interesting feature shown in Figure 3.4 is the effect of low concentrations of methanol on the ICP. Whereas high C loading resulting from methanol causes comparable effects on the plate voltage to similar mass flows of C from CO_2, low concentrations of methanol showed significantly less effect on the plate voltage than in the case of CO_2. This trend was even stronger for phenylalanine, where no effect on the plate voltage was found. These effects could be explained by considering that phenylalanine is introduced only in the form of an aerosol. Carbon is released only after decomposition inside the analyte channel and consequently the diffusion of C into the plasma core can be expected to start much later than in the case of a similar mass flow of CO_2. Thereby, the mass of C reaching the plasma core is much lower and the plate voltage reflects this trend. Following this hypothesis, two processes must be considered in the case of methanol: the vapor phase behaves similarly to gaseous reagents (CO_2) whereas the methanol inside the liquid droplets of the aerosol behaves like phenylalanine. At low methanol concentrations the evaporation of methanol in the spray chamber is not as dominant as at higher concentrations; the lower C emission signal and the smaller change in plate voltage for $1.7\,\mathrm{mg\,min^{-1}}$ C from methanol can be related to this mechanism.

Generally speaking, the enhancement factors of As and Se reported in the literature for non-volatile carbon sources (glucose, citric acid, oxalic acid or glycerol) were always lower than for more volatile reagents such as methanol or even for gases (CH_4), both in ICP-OES [79,86,87] and in ICP-MS [77,78,80,82,83,85,89–91].

3.1.4.5 Effect of bromine

As already noted, many attempts to explain the signal enhancing effect of carbon rely on the hypothesis of a charge transfer between C^+ and the high IP element. If carbon with an IP of 11.26 eV is behaving in this manner, Br with an IP of 11.81 eV can be expected to show similar effects.

In contrast to previous reports [87] we wanted to avoid variations in the nebulization efficiency and therefore used water saturated with bromine rather than HBr. Seven concentration levels ($0\text{-}34\,\mathrm{g\,L^{-1}}$ Br_2) were prepared from bromine-saturated water. The Br_2 concentration was calculated assuming a solubility of Br_2 in water [110] of $33.56\,\mathrm{g\,L^{-1}}$. All bromine concentrations given below correspond to the mass of bromine dissolved in water. Due to the toxicity of bromine, we have not attempted to quantify the mass flow of bromine reaching the plasma.

Bromine had little to no effect on most of the investigated emission lines. The signal intensities recorded in a 34 g L^{-1} Br_2 solution differed by less than ± 10 % from the signal recorded from an aqueous solution (3 % v/v HNO_3). The only exceptions were P, S and Se. For P and S the signal intensities initially rose quickly with increasing Br_2 concentration reaching a plateau at about 3.4 g L^{-1} Br_2 with signal intensities of about 13 % and 20 % (P and S respectively) higher than in an aqueous standard. For Se the signal increased almost linearly up to 6.7 g L^{-1} Br_2 (67 % higher signal than in diluted nitric acid) and then leveled off, reaching about 85% signal enhancement at 34 g L^{-1} Br_2. It is most interesting to note that neither As was enhanced by Br_2, nor were Au or Hg.

Plasma robustness and the excitation temperature remained constant when switching from an aqueous solution (3 % v/v HNO_3) to 34 g L^{-1} Br_2 and neither the plate voltage nor the power drawn by the RF generator changed significantly. The frequency of the RF generator dropped slightly but significantly by 2.6 kHz.

From these findings it must be concluded that the introduction of bromine did not affect the RF generator and it can be assumed that the power delivered to the ICP remained unchanged. The signal enhancement of P, S and particularly Se cannot be attributed to changes in the nebulization efficiency as other elements would have been affected too. Therefore, the effect of bromine on P, S and Se appears to be a true matrix effect of bromine on these three elements.

If a charge transfer process is the underlying mechanism of the observed effects, two conditions must be met: firstly, the Wigner spin conservation rule [111] must be fulfilled; secondly, the reaction energy defect should be minimal. Grindlay *et al.* [92] assumed that this type of reaction is likely to happen if the involved energy levels differ by between -1.0 eV and +0.5 eV.

From the data listed in Table 3.3 we can draw the conclusion that the Wigner spin conservation rule is fulfilled for every examined element. However, the energy difference between the involved levels appears to explain most of the observed effects of bromine: with the exception of Au, I, P, S, and Se the energy difference between the involved levels is too large. Iodine was not investigated, as the Br_2 used was slightly contaminated with this element. For P, S and Se a signal enhancement was observed that could consequently be attributed to a charge transfer reaction. However, for Au no significant signal increase was encountered when using Br_2, though the energy difference of the involved levels was only slightly larger than in the case of Se. This finding is unexpected, as the Au signal was enhanced in the presence of C.

Table 3.3: Electronic states and energy defects (ΔE) for the charge transfer reaction between Br^+ and selected elements. Br ionization potential: 11.81 eV; Br ground state ^2P; Br^+ ground state: ^3P; data from [112]

Element	**Atom ground state term**	**Energy level of the electronic state closest to the IP of Br**		**ΔE (eV)**	**Spin**	
		Term	Energy (eV)		S_i	S_p
As	^4S	^1D	11.04	0.77	5/2, 3/2, 1/2	1/2
Au	^2S	^3D	11.41	0.40	3/2, 1/2	3/2, 1/2
Be	^1S	^2P	13.28	-1.47	1, 0	1, 0
Cd	^1S	^2P	14.47	-2.66	1, 0	1, 0
Cl	^2P	^3P	12.97	-1.16	3/2, 1/2	3/2, 1/2
Hg	^1S	^2S	10.44	1.37	1, 0	1, 0
I	^2P	^1D	12.15	-0.34	3/2, 1/2	1/2
P	^4S	^1D	11.59	0.22	5/2, 3/2, 1/2	1/2
S	^3P	^2D	12.20	-0.39	2, 1	1, 0
Se	^3P	^2D	11.46	0.35	2, 1	1, 0
Zn	^1S	^2S	9.39	2.42	1, 0	1, 0

3.1.4.6 Effect of NaCl

The presence of high concentrations (>1 g L^{-1}) of easily ionizable elements (EIEs) such as Na is reported to cause plasma related signal variations [113] in the emission line intensities of other elements. Consistent with our previous work [98] we encountered a small, but significant decrease of the RF generator frequency (2.2 kHz) and a severe drop of plasma robustness (from 7.0 to 5.4 when increasing the NaCl concentration in the sample solution from 0 g L^{-1} to 30 g L^{-1}). However, the excitation temperature decreased only to 6510 ± 20 K over the same interval. Dennaud *et al.* [114] calculated the theoretical plasma robustness as a function of the temperature and found a linear correlation between these two factors, assuming local thermal equilibrium (LTE) in the plasma discharge. When plotting the excitation temperature vs. plasma robustness for all reagents reported Table 3.2 bromine and all carbon-based reagents follow a general linear trend. However, for NaCl the excitation temperature strongly deviates from this trend. As the measured decrease of the plasma robustness agrees well with data reported in the literature (*e.g.* Brenner *et al.* [115] found that at 1350 W RF power plasma robustness decreased from 9.1 to 7.4 when increasing the NaCl concentration from 0 to 10 g L^{-1}), the surprisingly high excitation temperature might stem from a stronger deviation of the iron atom level population from the Boltzmann distribution and the associated departure from the LTE. However, the Boltzmann plots of the Fe(I) lines were not significantly curved (calculation based on an f-test of the residual standard deviations of the Boltzmann plot using either a liner fit or a second order polynomial fit) as reported by Kitagawa and Horlick [116].

The investigated emission lines were in general all suppressed by large quantities of NaCl (30 g L^{-1}) as shown in Table 3.2. In contrast to the effect of C, the power vacuum tube's plate voltage remained constant up to about 6 g L^{-1} and then dropped almost linearly by 50 V towards the highest investigated NaCl concentration of 30 g L^{-1}. Though this drop is significant, the suppression of the analyte emission signals cannot be related to this reduction in RF power, as the drop of 50 V corresponds to a reduction of the RF generator input power of only about 30 W.

3.1.4.7 Differentiating between the factors contributing to the carbon enhancement effect

From the foregoing discussion it can be concluded that the signal enhancing effect of carbon on several elements is a combination of changes in the excitation equilibrium (*e.g.* caused by a charge transfer reaction) and higher plasma power density. The latter stems from RF generator control issues and the thermal pinch effect.

In an attempt to discriminate between these two effects, solutions containing As, Au, Be, Br, Cl, Hg, P, S, and Se (concentration of each element similar to the previously used standard solutions) in either 3 % (v/v) HNO_3 or 10 % (m/m) methanol together with the respective blank solutions (only diluted nitric acid or 10 % methanol) were measured at constant torch gas flows (as listed in Table 3.1) but at different RF power levels (1300-1495 W; 50 W increments; setting a higher power level than 1495 W was not possible, as the instrument control software then increased the outer gas flow in an attempt to protect the torch).

As expected, a rising RF power level resulted, in both 3 % (v/v) HNO_3 and methanol, in an increase of the blank signal corrected analyte emission intensity. However, distinct differences were encountered between the investigated emission lines: methanol had little effect on low excitation energy (4-5 eV) atom lines (*e.g.* Au I 267.595 or Hg I 253.652 nm) as the signal intensity was similar to that in 3 % (v/v) HNO_3. This finding is consistent with data presented in Table 3.2. For emission lines of higher excitation energy, the analyte emission signal in methanol was always higher than in the corresponding aqueous standard for all RF power levels. This effect became more pronounced with increasing total emission line energy, although only a general trend was encountered but no function was found to sufficiently fit all data points. When plotting the signal intensity for each emission line as a function of the RF power level used, straight lines were obtained ($R_2 > 0.999$). The slope of these lines was always lower in methanol when compared to aqueous solutions. From this finding it can be concluded that the magnitude of the carbon enhancement effect is also dependent on the RF power level used. A similar observation has been reported by Kralj and Veber [91].

To separate the effects of increased plasma power density and changes in the emission line excitation equilibrium on the analyte signal, the RF power vs. emission line intensity plots can be used. When assuming that there is no change in the excitation equilibrium by methanol (*e.g.* by a charge transfer reaction), any change in the emission signal caused by methanol would be dependent on the power density in the ICP discharge. Consequently, "apparent" RF power levels can be calculated from the RF power vs. emission line intensity plots of aqueous standards (3 % v/v HNO_3) and the corresponding analyte signal in 10 % methanol at a fixed RF power level (*e.g.* 1350 W). These "apparent" RF power levels describe the hypothetical RF power necessary for obtaining the same emission signal for an aqueous (3 % v/v HNO_3) solution as in 10 % methanol if the change in plasma power density was the only effect of methanol on the ICP. In Table 3.4 these "apparent" RF power levels are listed for 1350 W. There is no clear correlation between these "apparent" RF power levels and the total energy of the emission line.

Table 3.4: Calculated, hypothetical RF power levels to obtain the same emission signa intensity in an aqueous solution (3 % v/v HNO_3) as in 10 % (m/m) methanol at 1350 W if the RF power level is the only factor that alters the signal intensity

Element and emission line, nm	**Total line energy, eV**	**“Apparent” RF power, W**
Ar I 404.442	14.69	1540
Ar I 430.010	14.51	1540
As I 189.042	6.56	1660
As I 193.759	6.40	1640
As I 197.262	6.29	1660
Au I 201.200	7.30	1480
Au I 242.795	5.11	1430
Au I 267.595	4.63	1400
Be I 234.861	5.28	1410
Be I 313.042	13.28	1480
Be II 313.107	13.28	1470
Br I 144.990	8.55	1540
Cl I 134.724	9.20	1540
Cl I 135.165	9.28	1720
Cl I 136.345	9.20	1540
Hg I 184.950	6.70	1480
Hg II 194.227	16.82	1480
Hg I 253.652	4.89	1320
Hg I 435.835	7.73	1440
P I 138.147	8.97	1620
P I 169.403	8.73	1630
P I 177.495	6.99	1640
P I 178.287	6.95	1620
P I 213.618	7.21	1650
P I 214.914	7.18	1660
S I 142.503	8.70	1530
S I 180.731	6.86	1560
S I 182.034	6.86	1590
Se I 196.090	6.32	1830
Se I 203.985	6.32	1900

The tapping of the RF generator's HV power supply revealed, as reported above, that in the presence of 10 % methanol the power drawn by the RF generator increased by about 250 W. The efficiency of the RF generator (power delivered to the ICP as set in the instrument control software divided by the generator input power) was about 60 %. Thereby it can be estimated that the power level in the ICP discharge in the presence of methanol was roughly 1350 W + 250 W × 0.6 = 1500 W. Simultaneously, the thermal pinch effect decreased the volume of the plasma. Using the method of Greenfield and McGeachin [117] the decrease of the plasma volume estimated from Figure 3.3 was 20-30 %. This value represents only a rough estimate, as the boundaries of the ICP are not sharply defined and the plasma can only be approximated as a geometrical combination of a cylinder and a cone. It appears questionable that these two mechanisms for increasing the power density of the ICP are simply additive. Moreover, it is not clear whether the impedance changes of the ICP are a consequence of the plasma's constriction or a change in the total gas composition, or a combination of both effects. In conclusion, too many uncertainties and unknowns are present to even estimate the true power level in the ICP discharge when loaded with methanol and only calorimetric means appear to be a viable method for providing reliable data. However, the power fed to the ICP can be approximated using voltage and current drawn from the HV power supply: at 1350 W the set current is 0.58 A. As previously described, the current remains constant but the voltage fed to the RF generator increases with increasing carbon load of the ICP. Consequently, at the maximum rating of the HV power supply of 4200 V the generator can draw 4200 V × 0.58 A = 2436 W power. Using again an efficiency of 60 % results in about 1460 W that the RF generator can drive into the load – the ICP – under worst-case conditions.

Using this 1460 W, the "apparent" power levels listed in Table 3.4 might allow us to distinguish between plasma power density related signal enhancement and changes of the excitation equilibrium: if the "apparent" power level of an emission line is much higher than 1460 W, a secondary process must be involved. When assuming that a difference of 200 W is significant, the following emission lines can be expected to be enhanced by other processes rather than increased RF power: As I 189.042 nm, As I 193.759 nm, As I 197.262 nm, Cl I 135.165 nm, P I 138.147 nm, P I 169.403 nm, P I 177.495 nm, P I 178.287 nm, P I 213.618 nm, P I 214.914 nm, Se I 196.090 nm, and Se I 203.985 nm. The excitation energy of these atom lines is between 6.3 and

9.3 eV. It is interesting to note that all investigated emission lines of As, P and Se follow this trend but only one chlorine line (135.165 nm) follows this trend.

On the other hand, the enhancement of emission lines with an "apparent" power level of ≤1460 W can be explained solely on the basis of the increased RF power coupled into the ICP. This group involves Au I 242.795 nm, Au I 267.595 nm, Be I 234.861 nm, Hg I 253.652 nm, Hg I 435.835 nm and potentially also Au I 201.200 nm, Be II 313.042 nm, Be II 313.107 nm, Hg I 184.950 nm, and Hg II 194.227 nm (the "apparent" power of these lines is only 20 W above the calculated one). The energy sum of these lines spans from 4.6 to 16.8 eV.

For the remaining emission lines (Ar I 404.442 nm, Ar I 430.010 nm, Br I 144.990 nm, Cl I 134.724 nm, Cl I 136.345 nm, S I 142.503 nm, S I 180.731 nm, and S I 182.034 nm) listed in Table 3.4 no clear trend can be defined.

3.1.5 Conclusion

Carbon-based matrix effects in ICP-OES and ICP-MS arise not only from a single cause but appear to be a combination of several factors: (1) depending on the source of carbon used, changes of the sample transport efficiency in the nebulizer and spray chamber due to variations in viscosity, surface tension or density; (2) matrix-induced excitation of certain energy levels by mechanisms such as the charge transfer reaction; (3) thermal pinch effect that results in a constriction of the ICP and consequently a higher power density of the remaining discharge; (4) RF generator related effects due to changes in plasma impedance. Effects 3 and 4 can be expected to be different for every type of RF generator as the impedance changes will act differently on each specific circuit arrangement (free-running generators or crystal stabilized ones with an additional impedance matching network). Particularly the power control algorithm that regulates current and voltage fed to the power electronics can be expected to have a great influence on the stability of the RF generator when loading the ICP with large amounts of carbon. Even the dimensions of the torch or the operating frequency might cause differences in the effect of carbon. As already reported, slight changes of the torch position were found to alter the excitation temperature. The frequency on the other hand determines the skin depth of the RF current in the ICP and is often associated with either a three or a four turn load coil (27 or 40 MHz respectively). In conclusion, the response of the RF generator to plasma impedance changes appears to be the dominant reason for the large spread of the enhancement factors reported in the literature.

Another factor that should be considered in this context is the fact that not the concentration of carbon in the sample solution determines the degree of matrix effect, but the mass flow of carbon that reaches the ICP and its state of matter. Gaseous reagents affect the plasma core more readily than non-volatile liquid ones.

Based on the findings presented here, the charge transfer reaction combined with the higher power density in the ICP discharge appears to explain most of the element enhancements by C or Br. However, the mechanism fails to explain that in the presence of sufficient carbon elements that cannot be expected to be enhanced by a charge transfer reaction (very high reaction energy defect) also were strongly enhanced (*e.g.* some emission lines of Cl). We can only but agree with Grindlay *et al.* [92] that "additional studies are required to explain these anomalies".

3.2 Effect of the addition of N_2 or O_2 to the gas flows in an ICP-OES

3.2.1 Introduction

In the publication shown above [63] it has been highlighted, that especially the carbon content in a sample has a great influence on the measurement, depending on the amount of carbon, target element, emission line and the source of carbon. The carbon-addition in form of gas (CO_2) or a volatile liquid (methanol) proved to influence the measurement in a greater fashion, than the use of a non-volatile substance (phenylalanine). This leads to the assumption that other gaseous compounds could affect a measurement likewise.

The aim of this work was to investigate the effect of added N_2 and O_2 to the nebulizer gas flow (through the scott spraychamber) or to the intermediate gas flow. Not only the received signals were of importance, but additionally the RF generator input power and the responding frequency.

In the literature a lot of investigations can be found on the usage of mixed-gas plasmas, with N_2 and O_2 as the most prominent added gasses, but also with He or H_2.

Nitrogen has a higher thermal conductivity than argon, which should enable a better heat transfer in the ICP. This causes also an increased energy coupling between the induction zone and the central channel of the plasma. As a consequence of the high thermal conductivity of N_2 the excitation temperature decreases, when N_2 is added to the outer gas flow [118]. But also the addition of N_2 to the nebulizer has a cooling effect, especially on the central channel of the plasma. In comparison to that an addition to the auxiliary flow results in an increase of the central channel temperature, because of an improved heat transfer. [119]

Lam and McLaren [120] showed that an addition of N_2 to the outer gas flow causes an constriction of the plasma, which was also reported as 'plasma shrinking' or 'thermal pinching' by other authors [121–123]. However, if N_2 is added to the nebulizer gas, the central channel of the plasma is mostly widened, with the result of a decreased sensitivity in ICP-MS [120].

Previous studies showed that an addition of N_2 to the nebulizer gas flow increases the sensitivity of most emission lines, with no explicit difference between atomic and

ionic lines [124]. Additionally to enhanced signals, it is reported that the addition of N_2, depending on which gas stream it is added, or replacement of the same, can reduce polyatomic interferences in the ICP-MS and matric effects in both ICP-MS and ICP-OES. A greater plasma robustness (measured as the Mg(II)/Mg(I) ratio) and a reduction of matrix effects were published [98,124–128]. However, in the case of N_2 it is very important to note that there is a significant difference between adding the gas to the outer, intermediate or inner gas flow. Some of the advantages shown above may only occur with the addition to a specific gas flow and not the others.
Further on, because of the similar ionization potential of N_2 (15.58 eV) in comparison to argon (15.76 eV) the occurrence of charge transfer reactions is assumed [118].

The addition of O_2 to either of the gas flows proved to be similar to the addition of N_2. An improved plasma robustness, as well as a reduction of matrix effects were reported [127,129]. The addition of O_2 is especially highly efficient regarding the improvement of the determination of samples with a high carbon content. Carbon deposits on the torch are minimized and the emission of carbon compounds (so called Swan bands) is reduced [130]. This results in better signal/noise ratios [127,130].

3.2.2 Instrumentation and Reagents

The setup used was the same as for the gaseous carbon experiments previously described [63] with an axially viewed ICP-OES (CIROS Vision EOP, Spectro, Germany) and a mass flow controller (100 sccm, Mass-Flo 1179, MKS Instruments, Germany) for the addition of different amounts of N_2 or O_2, either to the nebulizer or the intermediate gas flow.
The ICP-OES operation conditions, as well as the setup used to measure the frequency response of the RF generator and the current and voltage delivered to generator are described elsewhere [63,98].

The chemicals and test solutions (see Table 3.5) were the same as in a previous publication (described in chapter 3.1). Argon 5.0 (Messer, Austria) and additionally N_2 5.0 (Linde, Austria) and O_2 5.0 (Linde, Austria) were used. These gases were added either to the nebulizer flow via the scott spraychamber, or to the intermediate stream by using a small T-piece. The equivalent of 5, 10, 15 and 20 mL N_2 or

O_2 min^{-1} were mixed to the argon flow and all 157 emission lines of the 36 elements were measured simultaneously.

For the determination of the enhancement factors four standard solutions were measured including one blank.

Table 3.5: Composition of the three test solutions

	Elements	**Concentration [mg L^{-1}]**
Solution 1	Al, Be, Ca, Cd, Co, Cr, Cu, Fe, K, Li, Mg, Mn, Mo, Na, Ni, Sb, Sr, Ti, Tl, V, Zn	2
	B, Bi, Pb,	10
	As, Se	20
Solution 2	Au, Br, Hg, P, S	10
Solution 3	I	30
Solution 4	Fe	300

The plasma robustness was determined via the measurement of a 2 mg L^{-1} Mg solution and the resulting emission line intensity ratio of Mg(II) 280.270 nm/Mg(I) 285.213 nm.

3.2.3 Results and Discussion

The investigation of carbon added either to a solution or to a gas flow showed that it doesn´t only effect emission line intensities, but the generator itself. The same trend can be seen with N_2 and O_2. With increasing concentration of both gasses the RF generator draws more power, whereby N_2 has a significantly higher influence. At a very low flow of 5 mL min^{-1} there is also a difference to be seen between the N_2-adding to the nebulizer of the intermediate gas flow, with the second having a higher impact on the generator power. This trend stays consistent at first, but mellows out at a higher flow of 20 mL min^{-1}. O_2 generally enhances the drawn power less and in this case the adding to the nebulizer flow is of a greater influence. At the same time the responding generator frequency decreases in the same fashion as the power increases. Again, added N_2 to the intermediate gas flow has the highest effect.

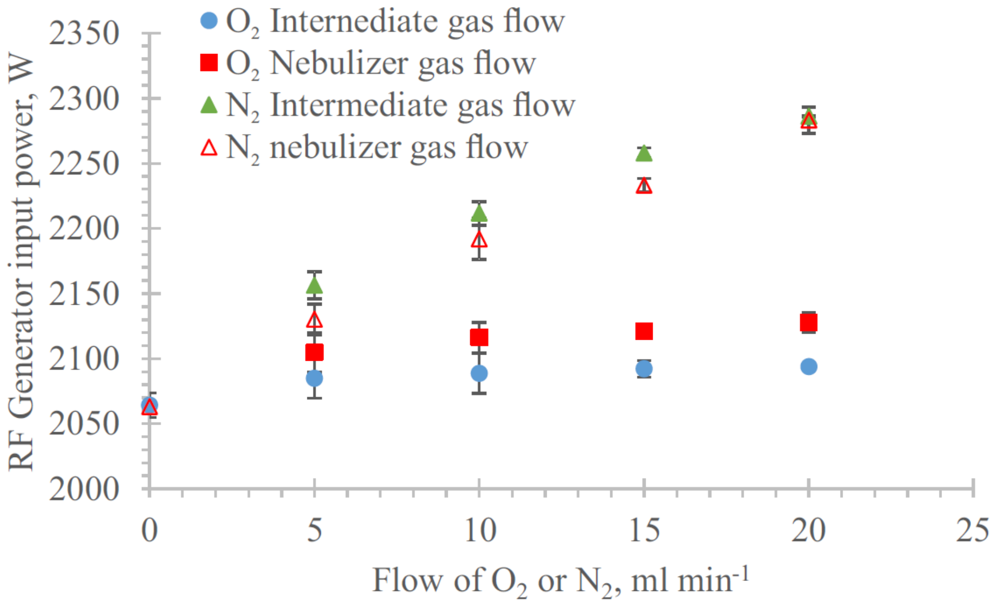

Figure 3.5: Power drawn by the RF generator (nominal output: 1350 W) with increasing amount of added N_2 or O_2

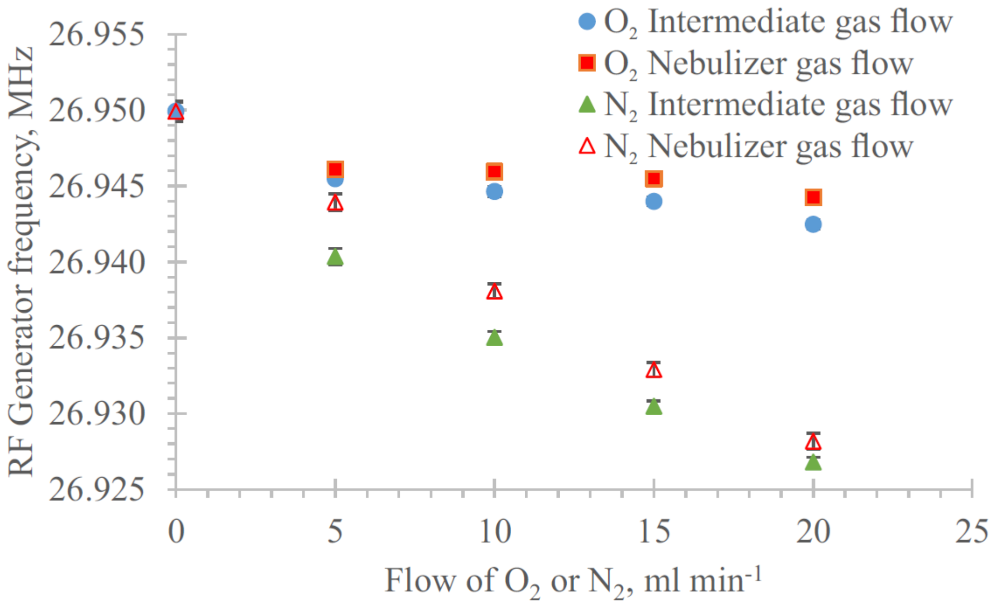

Figure 3.6: Frequency response of the RF generator with increasing amount of added N_2 or O_2

The results shown in the figures above indicate quite clearly that adding a foreign gas to a previously exclusive argon flow leads to a change in the generator properties. Therefore, it is easy to assume that this would also affect the emission line intensities.

At the same time a shrinking of the plasma and shifting from the injector tube has been observed, especially while adding N_2 to the nebulizer flow.

Figure 3.7 shows the effect of the gasses on the plasma robustness. N_2 added to the nebulizer flow has obviously the most impact. Simultaneously, O_2 doesn´t affect the plasma robustness at all, or even has a slight negative impact at higher flows.

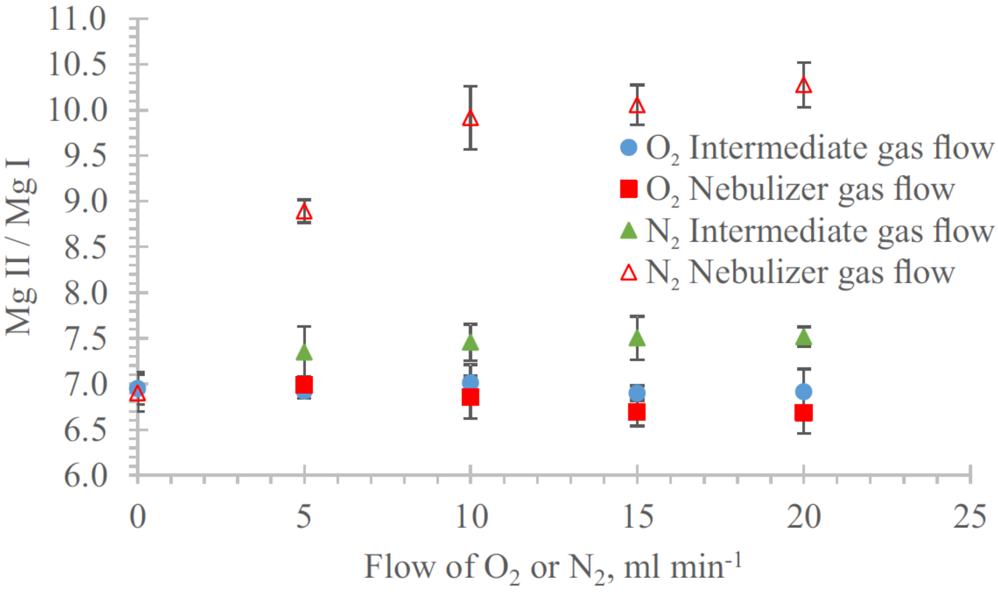

Figure 3.7: Plasma robustness as the ratio Mg(II)/Mg(I)

The enhancement factors (Table 3.6) were determined by adding 15 mL min^{-1} of N_2 or O_2 to either the intermediate or the nebulizer gas flow.

When looking at the emission lines intensities it is clear to see that, generally speaking, N_2 has a higher impact regarding signal enhancement or suppression than O_2. And in the case of both gasses, the addition to the intermediate gas flow has a stronger enhancement effect.

N_2 added to the intermediate gas flow causes most emission lines to be enhanced by 10-40 %. This includes almost all atom lines with excitation energies of 2-6 eV (e.g. Al, Na, Mn) and even some up to energies of 8 eV. Additionally, ion lines with total line energies (excitation and ionization) between 9 and 13 eV fall into that group.

Enhancement of over 50 % is the case for most atom lines with excitation potentials higher than 6 eV and ion lines with total line energies above 13 eV. Here the enhancement factors fluctuate quite strongly between 1.5 and 2.0, with a few exceptions of ion lines with an even higher factor.

The addition of N_2 to the nebulizer flow however shows a significantly different trend. Here, almost every atom line with an excitation energy lower than 5 eV is actually supressed by about 20-50 %. The biggest group consists of emission lines with enhancement factors between 0.9 and 1.1. This includes atom lines with the excitation potentials 5-8 eV and almost every ion line with a total line energy lower than 15 eV. Enhancement factors of 10-40 % can be found with atom lines of the energies 6-10 eV and ion lines above 15 eV.

The group of supressed elements include atom lines of the easily ionizable elements (EIEs) like Na, Mg and K. This is perfectly in sync with the literature. Various authors reported reduced matrix effects when adding N_2 to the nebulizer gas flow. As these effects can be caused by EIEs a suppression of the same would obviously limit their influence on a measurement. However, it is important to note that mainly a suppression of the atom lines is found, while the ion lines are only affected marginally.

With O_2 added to the intermediate gas flow the enhancement factors don´t fluctuate quite as much as with N_2. Most of the emission lines, both atom and ion lines, are enhanced by 10-40 %. Only atom lines with energies above 8 eV and ion lines with higher energies than 15 eV are affected stronger.

An addition of O_2 to the nebulizer flow seems to influence the emission signals only marginally. Enhancement factors of 0.9-1.1 are common with only a few exceptions.

Table 3.6 shows the enhancement/suppression factors of selected emission lines. For a better comparison with the enhancement factors of C (solution and gas), Br_2 and NaCl the same emission lines were selected as in the publication shown in chapter 3.1.

Table 3.6: Signal enhancement/suppression factors of selected emission lines; Int: spectral interference (blank signal >10 % of analyte signal); plasma robustness for an aqueous solution (3 % v/v HNO_3) and an exclusive Ar gas flow was 7.0 ± 0.1 with an excitation temperature T_{exc} of 6610 ± 20 K

Emission line, nm	Total line Energy, eV	15 mL min^{-1} N_2, Neb.	15 mL min^{-1} N_2, Interm.	15 mL min^{-1} O_2, Neb.	15 mL min^{-1} O_2, Interm.
Al I 396.152	3.14	0.74	1.31	1.00	1.21
Al II 167.078	13.41	1.25	1.86	1.08	1.44
Ar I 404.442	14.69	1.62	2.41	1.10	1.52
As I 197.262	6.29	1.19	1.51	1.04	1.26
As I 189.042	6.56	1.18	1.54	1.04	1.29
As I 193.759	6.40	1.19	1.52	1.04	1.28
Au I 267.595	4.63	1.07	1.27	1.14	1.14
Au I 242.795	5.11	1.08	1.34	1.14	1.17
B I 249.773	4.96	0.99	1.20	1.00	1.19
Be I 234.861	5.28	1.00	1.26	0.98	1.18
Be II 313.042	13.28	1.17	1.31	0.95	1.16
Br I 148.845	8.33	1.13	1.72	1.06	1.34
Br I 144.99	8.55	1.26	1.88	1.10	1.39
Cd I 228.802	5.42	0.99	1.33	1.00	1.21
Cd II 214.438	14.77	1.29	1.78	1.04	1.36
Cl I 134.724	9.20	1.31	2.05	1.14	1.47
Co II 230.786	13.75	1.08	1.46	1.00	1.25
Cr II 205.552	12.80	1.12	1.44	0.98	1.20
Hg I 253.652	4.89	0.98	1.13	0.97	1.13
Hg I 184.95	6.70	1.22	1.67	1.07	1.37
Hg II 194.227	16.82	1.24	1.74	1.07	1.35
I I 183.038	6.77	0.71	0.98	0.88	1.16
I I 178.276	6.95	0.90	1.26	0.98	1.25
Mg I 285.213	4.35	0.73	1.30	1.01	1.24
Mg II 280.27	12.07	1.07	1.41	0.97	1.23
P I 213.618	7.21	1.20	1.64	1.06	1.36
P I 169.403	8.73	1.15	1.64	1.05	1.36
P I 138.147	8.97	1.25	1.73	1.09	1.35
S I 180.731	6.86	1.13	1.64	1.09	1.34
S I 182.034	6.86	1.11	1.62	1.08	1.33
Se I 207.479	5.97	1.08	1.31	0.95	1.21
Se I 196.09	6.32	1.22	1.61	1.04	1.31
Se I 203.985	6.32	1.26	1.66	1.05	1.32
Tl I 276.787	4.48	0.82	1.23	0.94	1.17
Tl II 132.171	15.49	Int	Int	1.16	1.65
Zn I 213.856	5.80	1.03	1.38	1.00	1.22
Zn II 202.548	15.51	1.41	1.94	1.04	1.39
Plasma robustness		10.2 ± 0.2	7.5 ± 0.2	6.7 ± 0.1	6.8 ± 0.1

Figure 3.8 and Figure 3.9 show a comparison of elements/emission lines which are also affected quite strongly by a high carbon content of a sample or in the gas flow. More specifically it seems that they are highly influenced by the change in the drawn generator power as well as the decreased generator frequency. In both cases were the gasses added to the intermediate gas flow.

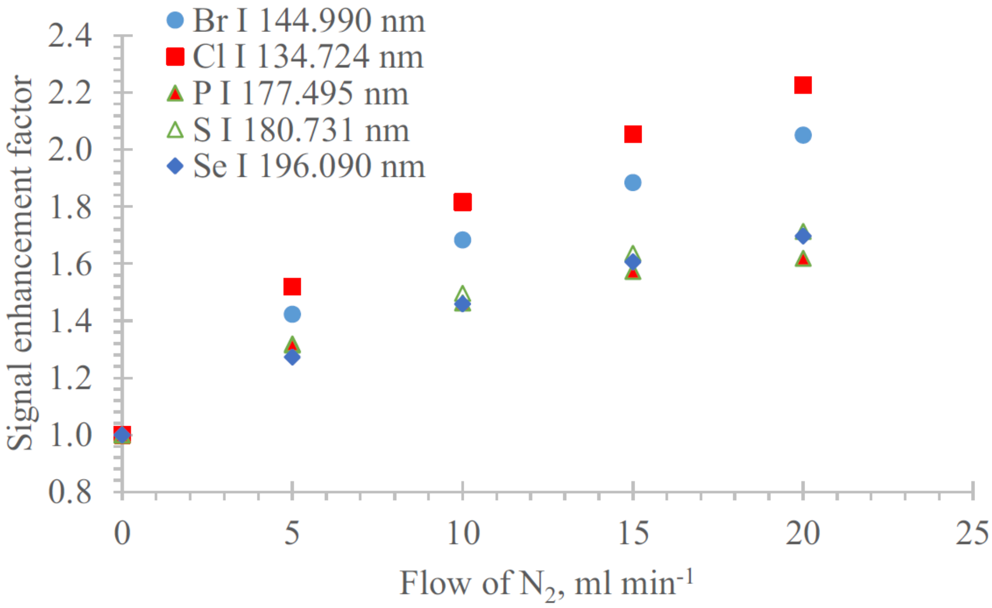

Figure 3.8: Signal enhancement factors of five atom emission lines with increasing N_2 flow (added to the intermediate gas flow)

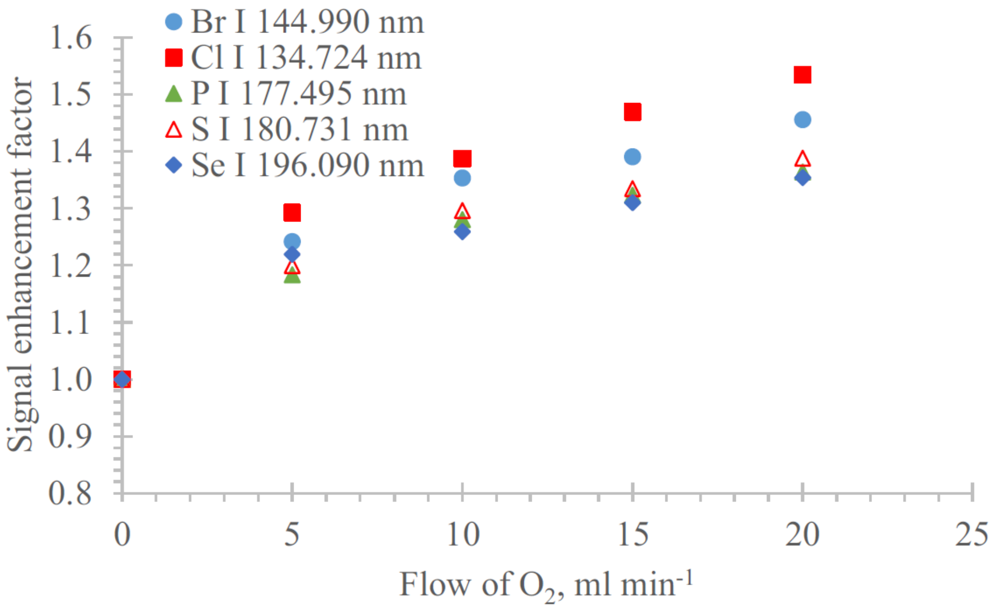

Figure 3.9: Signal enhancement factors of five atom emission lines with increasing O_2 flow (added to the intermediate gas flow)

The figures above indicate quite clearly that N_2 in general has a higher impact regarding signal enhancement than O_2. The enhancement factors of the same emission lines with the gasses added to the nebulizer flow are 40-70 % lower in the case of N_2 and around 30 % lower for O_2.

3.2.4 Conclusion and Outlook

Signal enhancement seems to be dependent on more than one factor. In a previous publication regarding a possible carbon-enhancement-effect it has been shown that there is a significant difference between adding carbon in liquid form or as a gas. The experiments with N_2 und O_2 indicate strongly that also the decision on which gas flow is spiked with a foreign gas has a great impact on the results.

The amount of enhancement or suppression of emission lines is caused by the following terms (same as with the enhancement caused by carbon):

1. RF generator induced enhancement: it was shown that with an increasing amount of foreign gas the drawn generator power is also increased and the frequency lowered (effect stronger with N_2 than with O_2). The resulting higher temperature explains many of the enhancement effects.

2. Plasma shrinking/thermal pinch effect: in some experiments not only the responses of the RF generator changed, but also the plasma visually. At a high foreign gas flow the plasma shrinks and moves away from the injector tube. This also causes a higher power density of the remaining discharge
3. Charge transfer effects: many of the enhanced signals can be explained by the points above. However, the occurrence of actual charge transfer reactions is possible and needs to be evaluated for every emission line separately.

To figure out which signal enhancement is actually just an effect of a free running RF generator out of control and what is a matrix induced excitation more experiments need to be done. One possible solution could be to constantly check the drawn power and frequency of the generator and adjust the set power. With this method one could guarantee a constant drawn power regardless of any additional gasses or substances. However, this cannot be expected to eradicate the thermal pinch effect.

4 Comparison of venting and non-venting microwave assisted digestion vessels

4.1 Introduction

The aim of this work was to investigate if venting of closed vessels during a microwave assisted digestion could lead to the loss of volatile elements.

Digestion vessels with a venting function are on the market for many years now. In the case of using closed vessels without a venting possibility a further heating until the desired digestion temperature is often stopped due to the reaching of the maximum pressure of a system. Venting steps release part of the pressure and therefore higher temperatures can be achieved. Unfortunately, opening a system under pressure to release the same could theoretically also lead to a loss of highly volatile elements like Hg, which was investigated in this thesis.

Many publications can be found about the stability of mercury either during the sample preparation or the storage afterwards. However, most of these concentrate on specific species of Hg, like inorganic or methylmercury. The total Hg concentration after a digestion is often not of interest. As with every other element there are a lot of factors which could influence a measurement. The most common of these factors are the sample itself, the container material and added reagents [131–140].

To improve the stability of Hg in a solution many authors suggest the addition of a small amount of HCl to create a stable $[HgCl_x]^{n-}$ complex [131,134,135,138,139].

Additionally to the added reagents, there are a lot of publications about which container material is the best to store samples in. The loss of Hg in acidified samples when using polyethylene tubes is well reported as well as the possibility to use Teflon or glass with no or minimal losses [131,135,139].

4.2 Instrumentation and Reagents

Two microwave systems were used in this thesis. One with closed vessels and one with closed vessels with an included venting system at a higher pressure.

Multiwave 3000 (Anton Paar, Graz, Austria):

HF100 vessel (closed vessels without venting) with a maximum pressure of 40 bar

digestion program: ramp of 20 minutes to 1200 W and holding it for 15 minutes; IR-limit: 210 °C

Multiwave GO (Anton Paar, Graz, Austria):

HVT50 vessels (closed vessels with a venting step at 20 bar)

digestion program: ramp of 10 minutes to 100 °C and holding it for 2 minutes; second ramp of 10 minutes to 180 °C and holding it for 8 minutes; venting pressure is 20 bar

Purified water (18 MΩ cm, Barnstead Nanopure, Thermo Fisher Scientific, USA) was used as well as nitric acid (69 %, purified by subboiling) and hydrochloric acid (30 %, Merck, suprapur). To measure the loss of volatile elements commercially available milk powder (Aptamil Folgemilch 2, Milupa Nutricia GmbH, Germany) was spiked with a single elements stock solution of Hg (1 g L^{-1}, in 10 % HNO_3, Roth, Germany). A Tl stock solution (1 g L^{-1}, in 2 % HNO_3, SCP Science, USA) was used as internal standard for the ICP-MS measurement. These stock solutions were also used for the liquid calibration.

The digested samples were appropriately diluted and measured with ICP-MS (Elan DRC+, cyclonic-spraychamber, Perkin Elmer, Massachusetts, USA).

Table 4.1: ICP-MS operating conditions for the measurement of the digested milk powder/Hg samples; Argon 5.0

Plasma Power	1350 W
Coolant Flow	15.00 L min^{-1}
Auxiliary Flow	1.20 L min^{-1}
Nebulizer Flow	1.00 L min^{-1}
Oxide rate	< 3 %
Doubly charged rate	< 3 %
Hg isotope	202
Tl isotope	205

Mercury was determined in representation of highly volatile elements as it has a well-known toxicity in certain structures. Mercury spiked to milk powder was selected as it is well known that the redox chemistry taking place during a digestion can foster the formation of highly volatile Hg^0. Different mixtures of nitric acid, hydrochloric acid and purified water were used. Milk powder was the sample of choice mainly because of its high sugar (42 %) and fat (20 %) content. The percent values were calculated with the table of contents given by the manufacturer. Sugar reacts quite strongly with nitric acid and guarantees therefore at least one venting step and a resulting possible loss of volatile elements.

The Multiwave 3000 records the pressure of one vessel and the IR temperature of all vessels each digestion while the Multiwave GO records just the temperature but also for every vessel. Therefore, it is unfortunately not possible to determine the number of venting steps nor their duration. However, as at every digestion with the Multiwave 3000 the pressure limit of 40 bar was reached before the end of the run, it is guaranteed that there are in fact venting steps with the Mutliwave GO, especially as the pressure limit for the venting is 20 bar.

4.3 Results and discussion

The aim of this work was not only to determine if a venting step during a microwave assisted acid digestion could lead to the loss of volatile elements, but also if the addition of hydrochloric acid as a stabilization reagent could prevent such a loss in the case of mercury. The theory of using hydrochloric acid in such a way was already discussed in the introduction.

The acid/water mixtures for the digestions and their labels are:
Name of the microwave_2 mL HCl → 4 mL HNO_3, 2 mL HCl
Name of the microwave_1 mL HCl → 4 mL HNO_3, 1 mL HCl, 1 mL H_2O
Name of the microwave_0.5 mL HCl → 4 mL HNO_3, 0.5 mL HCl, 1.5 mL H_2O
Name of the microwave_1 mL HCl_a.d. → 4 mL HNO_3, 2 mL H_2O, 1 mL HCl added after the digestion
Name of the microwave_0 mL HCl → 4 mL HNO_3, 2 mL H_2O

For the digestions approximately 200 mg milk powder were spiked with Hg and Tl as an internal standard (end concentration after dilution for each element were 10 µg L^{-1}). The vessels were thoroughly cleaned between the digestions to avoid cross contamination and the ICP-MS was specifically tuned for the measurement of Hg.

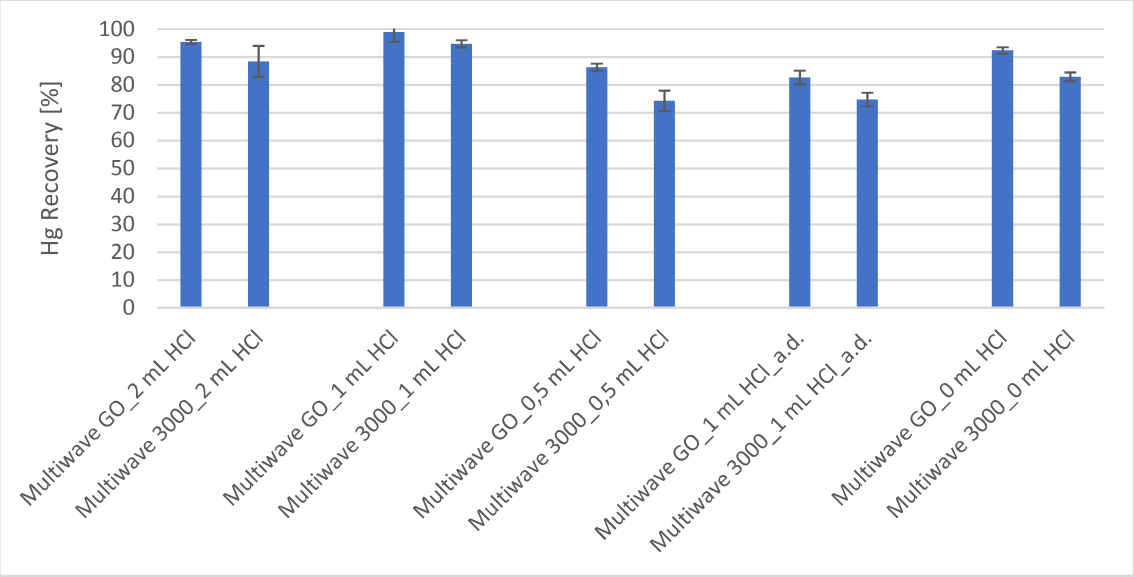

Figure 4.1: Hg recovery rates of different digestions of spiked milk powder; n=4

The standard uncertainty is defined as the half width confidence interval of 95 %. Figure 4.1 show that there are obviously some losses of Hg during the digestion. However, the results of the Multiwave GO with the venting vessels are in fact better than those of the Multiwave 3000. Also, no clear correlation between the amount of HCl and the recovery rates can be seen. This fact in itself is actually not very surprising. Some authors described a good stability of Hg without HCl for a few days and losses to the container walls only at long-term storage. It was assumed that by the addition of HCl these losses could be avoided. To prove or disprove this assumption the digested samples were stored in polypropylene tubes for 15 months in a cooling room at 4 °C.

Table 4.2: Hg recovery rates after 15 months in regards to the originally spiked concentration (mean value ± standard uncertainty, n=4) and the mean percentual loss during the storage time

Digestion	**Recovery [%]**	**Hg loss [%] during storage**
Multiwave GO_2 mL HCl	91,8 ± 1,0	3,7
Multiwave 3000_2 mL HCl	86,7 ± 1,6	2,0
Multiwave GO_1 mL HCl	89,4 ± 1,1	9,6
Multiwave 3000_1 mL HCl	86,9 ± 0,8	8,3
Multiwave GO_0,5 mL HCl	80,4 ± 0,5	6,9
Multiwave 3000_0,5 mL HCl	78,2 ± 0,7	-5,3
Multiwave GO_1 mL HCl_a.d.	80,1 ± 1,2	3,1
Multiwave 3000_1 mL HCl_a.d.	79,2 ± 0,9	-5,9
Multiwave GO_0 mL HCl	89,5 ± 1,7	3,1
Multiwave 3000_0 mL HCl	91,0 ± 1,0	-9,8

Again, no clear correlation between the HCl concentrations and Hg recovery can be seen. In the case of three Multiwave 3000 digestions there actually seems to be an addition of Hg. The reason for this is unknown and lies probably in a systematic error during the Hg quantification. It seems rather unlikely that the polymer tubes used for storage don´t form an equilibrium with the mercury present in the solution. Another option would be uncontrolled evaporation of water from the vessels. However, this should be corrected by the internal standard that was added already before the digestion (together with the Hg spike). All losses and seemingly gains of Hg during the storage time are however lower than 10 %. It seems not unlikely that the overall error of the digestion procedure combined with the Hg measurement and the storage sum up to a similar value, rendering the observed changes not significant.

5 Appendix

5.1 List of Figures

5.2 List of Tables

5.3 Acronyms

ADC – analog digital converter
BAM – Bundesanstalt für Materialforschung und -prüfung
EP – excitation potential
ICP – inductively-coupled plasma
ICP-MS – inductively-coupled plasma mass spectrometry
ICP-OES – inductively-coupled plasma optical emission spectrometry
IP – ionization potential
LA – laser ablation
LTE – local thermodynamic equilibrium
PC – polycarbonate
PEEK – polyether ether ketone
PFA – perfluoroalkoxy alkane
PTFE – polytetrafluorethylene
RCC – residual carbon content
RF – radiofrequency
RMS – root mean square
SD – standard deviation

5.4 Literature

1. Lichte FE. Determination of Elemental Content of Rocks by Laser Ablation Inductively Coupled Plasma Mass Spectrometry. Anal Chem. 1995 Jul 15;67(14):2479–85.

2. Baker SA, Bi M, Aucelio RQ, Smith BW, Winefordner JD. Analysis of soil and sediment samples by laser ablation inductively coupled plasma mass spectrometry. J Anal At Spectrom. 1999;14(1):19–26.

3. Shaheen ME, Gagnon JE, Fryer BJ. Femtosecond (fs) lasers coupled with modern ICP-MS instruments provide new and improved potential for in situ elemental and isotopic analyses in the geosciences. Chem Geol. 2012 Nov;330–331:260–73.

4. Brostoff LB, González JJ, Jett P, Russo RE. Trace element fingerprinting of ancient Chinese gold with femtosecond laser ablation-inductively coupled mass spectrometry. J Archaeol Sci. 2009 Feb;36(2):461–6.

5. Šelih VS, van Elteren JT. Quantitative multi-element mapping of ancient glass using a simple and robust LA-ICP-MS rastering procedure in combination with image analysis. Anal Bioanal Chem. 2011 Aug;401(2):745–55.

6. Ducreux-Zappa M, Mermet J-M. Analysis of glass by UV laser ablation inductively coupled plasma atomic emission spectrometry. Part 1. Effects of the laser parameters on the amount of ablated material and the temporal behaviour of the signal for different types of laser. Spectrochim Acta Part B At Spectrosc. 1996 Feb;51(3):321–32.

7. Burakov VS, Raikov SN. Quantitative analysis of alloys and glasses by a calibration-free method using laser-induced breakdown spectroscopy. Spectrochim Acta Part B At Spectrosc. 2007 Mar;62(3):217–23.

8. Wiltsche H, Günther D. Capabilities of femtosecond laser ablation ICP-MS for the major, minor, and trace element analysis of high alloyed steels and super alloys. Anal Bioanal Chem. 2011 Feb;399(6):2167–74.

9. Borisov OV, Mao XL, Fernandez A, Caetano M, Russo RE. Inductively coupled plasma mass spectrometric study of non-linear calibration behavior during laser ablation of binary Cu–Zn Alloys. Spectrochim Acta Part B At Spectrosc. 1999 Sep;54(9):1351–65.

10. Gagean M, Mermet JM. Study of laser ablation of brass materials using inductively coupled plasma atomic emission spectrometric detection. Spectrochim Acta Part B At Spectrosc. 1998 Apr;53(4):581–91.

11. Colao F, Fantoni R, Caneve L, Fornarini L, Lazic V, Santagata A, Teghil R, Giardini A. Study of laser produced plasma in Cu-based alloys. In: Advanced Laser Technologies 2004 [Internet]. International Society for Optics and Photonics; 2005 [cited 2019 Jan 30]. p. 51–9. Available from: https://www.spiedigitallibrary.org/conference-proceedings-of-

spie/5850/0000/Study-of-laser-produced-plasma-in-Cu-based-alloys/10.1117/12.633543.short

12. Colao F, Fantoni R, Lazic V, Caneve L, Giardini A, Spizzichino V. LIBS as a diagnostic tool during the laser cleaning of copper based alloys: experimental results. J Anal At Spectrom. 2004;19(4):502.

13. Yilmaz HC, Hattendorf B. A comparison of signal suppression and particle size distributions for ns- and fs-LA of metallic samples by LA-ETV-ICPMS. J Anal At Spectrom. 2017;32(10):1980–7.

14. Flamigni LA. Fundamental studies on the vaporization behavior of laser-generated aerosols in an inductively-coupled plasma used for mass spectrometry [Internet]. ETH Zurich; 2014 [cited 2019 Jan 30]. Available from: http://hdl.handle.net/20.500.11850/154589

15. LaHaye NL, Harilal SS, Diwakar PK, Hassanein A. Characterization of laser ablation sample introduction plasma plumes in fs-LA-ICP-MS. J Anal Spectrom. 2014;29(12):2267–74.

16. Lindner H, Koch J, Niemax K. Production of Ultrafine Particles by Nanosecond Laser Sampling Using Orthogonal Prepulse Laser Breakdown. Anal Chem. 2005 Dec;77(23):7528–33.

17. Kuhn H-R, Günther D. Elemental Fractionation Studies in Laser Ablation Inductively Coupled Plasma Mass Spectrometry on Laser-Induced Brass Aerosols. Anal Chem. 2003 Feb;75(4):747–53.

18. Poitrasson F, d’Abzac F-X. Femtosecond laser ablation inductively coupled plasma source mass spectrometry for elemental and isotopic analysis: are ultrafast lasers worthwhile? J Anal At Spectrom. 2017;32(6):1075–91.

19. Je TE. Application of a frequency quintupled Nd5YAG source (l=213 nm) for laser ablation inductively coupled plasma mass spectrometric analysis of minerals. :6.

20. Gunther D. Comparison of the ablation behaviour of 266 nm Nd5YAG and 193 nm ArF excimer lasers for LA-ICP-MS analysis† Plenary Lecture. :6.

21. Eggins SM, Kinsley LPJ, Shelley JMG. Deposition and element fractionation processes during atmospheric pressure laser sampling for analysis by ICP-MS. Appl Surf Sci. 1998 May;127–129:278–86.

22. Koch J, Wälle M, Dietiker R, Günther D. Analysis of Laser-Produced Aerosols by Inductively Coupled Plasma Mass Spectrometry: Transport Phenomena and Elemental Fractionation. Anal Chem. 2008 Feb;80(4):915–21.

23. Fernández B, Claverie F, Pécheyran C, Donard OFX, Claverie F. Direct analysis of solid samples by fs-LA-ICP-MS. TrAC Trends Anal Chem. 2007 Nov;26(10):951–66.

24. Liu X, Du D, Mourou G. Laser ablation and micromachining with ultrashort laser pulses. IEEE J Quantum Electron. 1997 Oct;33(10):1706–16.

25. Liu C, Mao XL, Mao SS, Zeng X, Greif R, Russo RE. Nanosecond and Femtosecond Laser Ablation of Brass: Particulate and ICPMS Measurements. Anal Chem. 2004 Jan 1;76(2):379–83.

26. Koch J, Lindner H, von Bohlen A, Hergenröder R, Niemax K. Elemental fractionation of dielectric aerosols produced by near-infrared femtosecond laser ablation of silicate glasses. J Anal At Spectrom. 2005;20(9):901.

27. Kuhn H-R, Günther D. Laser ablation-ICP-MS: particle size dependent elemental composition studies on filter-collected and online measured aerosols from glass. J Anal Spectrom. 2004;19(9):1158–64.

28. Shazzo YK, Karpov YA. Laser sampling in inductively coupled plasma mass spectrometry in the inorganic analysis of solid samples: Elemental fractionation as the main source of errors. J Anal Chem. 2016 Nov;71(11):1069–80.

29. Vanhaecke F, Dams R, Vandecasteele C. 'Zone model' as an explanation for signal behaviour and non-spectral interferences in inductively coupled plasma mass spectrometry. J Anal Spectrom. 1993;8(3):433–8.

30. Perdian DC, Bajic SJ, Baldwin DP, Houk RS. Time-resolved studies of particle effects in laser ablation inductively coupled plasma-mass spectrometry. 2008;11.

31. Zheng X-Y, Beard BL, Lee S, Reddy TR, Xu H, Johnson CM. Contrasting particle size distributions and Fe isotope fractionations during nanosecond and femtosecond laser ablation of Fe minerals: Implications for LA-MC-ICP-MS analysis of stable isotopes. Chem Geol. 2017 Feb;450:235–47.

32. Wohlgemuth-Ueberwasser CC, Jochum KP. Capability of fs-LA-ICP-MS for sulfide analysis in comparison to ns-LA-ICP-MS: reduction of laser induced matrix effects? J Anal At Spectrom. 2015;30(12):2469–80.

33. Poitrasson F, Mao X, Mao SS, Freydier R, Russo RE. Comparison of Ultraviolet Femtosecond and Nanosecond Laser Ablation Inductively Coupled Plasma Mass Spectrometry Analysis in Glass, Monazite, and Zircon. Anal Chem. 2003 Nov;75(22):6184–90.

34. Margetic V, Niemax K, Hergenroder R. A study of non-linear calibration graphs for brass with femtosecond laser-induced breakdown spectroscopy ঙ. At Spectrosc. 2001;8.

35. Takahashi T, Thornton B, Ohki K, Sakka T. Calibration-free analysis of immersed brass alloys using long-ns-duration pulse laser-induced breakdown spectroscopy with and without correction for nonstoichiometric ablation. Spectrochim Acta Part B At Spectrosc. 2015 Sep;111:8–14.

36. Matsumoto A, Tamura A, Koda R, Fukami K, Ogata YH, Nishi N, Thornton B, Sakka T. A calibration-free approach for on-site multi-element analysis of metal ions in aqueous solutions by electrodeposition-assisted underwater laser-induced breakdown spectroscopy. Spectrochim Acta Part B At Spectrosc. 2016 Apr;118:45–55.

37. Lide DR. CRC Handbook of Chemistry and Physics: A Ready-reference Book of Chemical and Physical Data. CRC Press; 1995. 2648 p.

38. Geertsen C, Briand A, Chartier F, Lacour J-L, Mauchien P, Sjöström S, Mermet J-M. Comparison between infrared and ultraviolet laser ablation at atmospheric pressure—implications for solid sampling inductively coupled plasma spectrometry. J Anal Spectrom. 1994;9(1):17–22.

39. Iida Y. Effects of atmosphere on laser vaporization and excitation processes of solid samples. Spectrochim Acta Part B At Spectrosc. 1990 Jan;45(12):1353–67.

40. Caneve L, Colao F, Fantoni R, Spizzichino V. Laser ablation of copper based alloys by single and double pulse laser induced breakdown spectroscopy. Appl Phys A. 2006 Nov;85(2):151–7.

41. Dell'Aglio M, Gaudiuso R, De Pascale O, De Giacomo A. Mechanisms and processes of pulsed laser ablation in liquids during nanoparticle production. Appl Surf Sci. 2015 Sep;348:4–9.

42. Zhang D, Liu J, Liang C. Perspective on how laser-ablated particles grow in liquids. Sci China Phys Mech Astron [Internet]. 2017 Jul [cited 2019 Jan 30];60(7). Available from: http://link.springer.com/10.1007/s11433-017-9035-8

43. Tamura A, Matsumoto A, Fukami K, Nishi N, Sakka T. Simultaneous observation of nascent plasma and bubble induced by laser ablation in water with various pulse durations. J Appl Phys. 2015 May 7;117(17):173304.

44. Zhang D, Gökce B, Notthoff C, Barcikowski S. Layered Seed-Growth of AgGe Football-like Microspheres via Precursor-Free Picosecond Laser Synthesis in Water. Sci Rep [Internet]. 2015 Nov [cited 2019 Feb 7];5(1). Available from: http://www.nature.com/articles/srep13661

45. Sakka T, Tamura A, Matsumoto A, Fukami K, Nishi N, Thornton B. Effects of pulse width on nascent laser-induced bubbles for underwater laser-induced breakdown spectroscopy. Spectrochim Acta Part B At Spectrosc. 2014 Jul;97:94–8.

46. Die Wechselwirkung eines Er:YAG-Laserstrahls mit Wasser - ZWP online - das Nachrichtenportal für die Dentalbranche [Internet]. [cited 2019 Feb 11]. Available from: https://www.zwp-online.info/fachgebiete/laserzahnmedizin/eryag/die-wechselwirkung-eines-er-yag-laserstrahls-mit-wasser

47. Hirata T, Nesbitt RW. U-Pb isotope geochronology of zircon: evaluation of the laser probe-inductively coupled plasma mass spectrometry technique. Geochim Cosmochim Acta. 1995 Jun;59(12):2491–500.

48. Knapp G. Microwave-heatable pressure reactor. 1995.

49. Wiltsche H, Tirk P, Motter H, Winkler M, Knapp G. A novel approach to high pressure flow digestion. J Anal Spectrom. 2014;29(2):272–9.

50. Linhares Marques T, Wiltsche H, Motter H, Nóbrega JA, Knapp G. High pressure microwave-assisted flow digestion system using a large volume reactor-feasibility for further analysis by inductively coupled plasma-based techniques. J Anal At Spectrom. 2015;30(9):1898–905.

51. Marques TL, Wiltsche H, Nóbrega JA, Winkler M, Knapp G. Performance evaluation of a high-pressure microwave-assisted flow digestion system for juice and milk sample preparation. Anal Bioanal Chem. 2017 Jul;409(18):4449–58.

52. Khan N, Jeong IS, Hwang IM, Kim JS, Choi SH, Nho EY, Choi JY, Park KS, Kim KS. Analysis of minor and trace elements in milk and yogurts by inductively coupled plasma-mass spectrometry (ICP-MS). Food Chem. 2014 Mar;147:220–4.

53. Suturović Z, Kravić S, Milanović S, Đurović A, Brezo T. Determination of heavy metals in milk and fermented milk products by potentiometric stripping analysis with constant inverse current in the analytical step. Food Chem. 2014 Jul;155:120–5.

54. Núñez-Sánchez N, Martínez-Marín AL, Polvillo O, Fernández-Cabanás VM, Carrizosa J, Urrutia B, Serradilla JM. Near Infrared Spectroscopy (NIRS) for the determination of the milk fat fatty acid profile of goats. Food Chem. 2016 Jan;190:244–52.

55. Welna M, Szymczycha-Madeja A. Effect of sample preparation procedure for the determination of As, Sb and Se in fruit juices by HG-ICP-OES. Food Chem. 2014 Sep;159:414–9.

56. Szymczycha-Madeja A, Welna M, Jedryczko D, Pohl P. Developments and strategies in the spectrochemical elemental analysis of fruit juices. TrAC Trends Anal Chem. 2014 Mar;55:68–80.

57. McKinstry P., Indyk H., Kim N. The determination of major and minor elements in milk and infant formula by slurry nebulisation and inductively coupled plasma - optical emission spectrometry (ICP-OES). Food Chem. 1999 May;65(2):245–52.

58. Sola-Larrañaga C, Navarro-Blasco I. Optimization of a slurry dispersion method for minerals and trace elements analysis in infant formulae by ICP OES and FAAS. Food Chem. 2009 Aug;115(3):1048–55.

59. A. Nóbrega J, Gélinas Y, Krushevska A, M. Barnes R. Direct Determination of Major and Trace Elements in Milk by Inductively Coupled Plasma Atomic Emission and Mass Spectrometry. J Anal Spectrom. 1997;12(10):1243–6.

60. Froes RES, Neto WB, Silva NOC e, Naveira RLP, Nascentes CC, da Silva JBB. Multivariate optimization by exploratory analysis applied to the determination of microelements in fruit juice by inductively coupled plasma optical emission spectrometry. Spectrochim Acta Part B At Spectrosc. 2009 Jun;64(6):619–22.

61. Szymczycha-Madeja A, Welna M. Evaluation of a simple and fast method for the multi-elemental analysis in commercial fruit juice samples using atomic emission spectrometry. Food Chem. 2013 Dec;141(4):3466–72.

62. Cindrić IJ, Zeiner M, Kröppl M, Stingeder G. Comparison of sample preparation methods for the ICP-AES determination of minor and major elements in clarified apple juices. Microchem J. 2011 Nov;99(2):364–9.

63. Wiltsche H, Winkler M, Tirk P. Matrix effects of carbon and bromine in inductively coupled plasma optical emission spectrometry. J Anal At Spectrom. 2015;30(10):2223–34.

64. Potortì AG, Di Bella G, Lo Turco V, Rando R, Dugo G. Non-toxic and potentially toxic elements in Italian donkey milk by ICP-MS and multivariate analysis. J Food Compos Anal. 2013 Aug;31(1):161–72.

65. Wiltsche H, Knapp G. Flow Digestion Systems with Microwave and Conductive Heating. In: Microwave-Assisted Sample Preparation for Trace Element Analysis [Internet]. Elsevier; 2014 [cited 2019 Mar 8]. p. 253–80. Available from: https://linkinghub.elsevier.com/retrieve/pii/B978044459420400009X

66. Pichler U, Haase A, Knapp G, Michaelis M. Microwave-Enhanced Flow System for High-Temperature Digestion of Resistant Organic Materials. Anal Chem. 1999 Sep;71(18):4050–5.

67. Stewart LJM, Barnes RM. Flow-through, microwave-heated digestion chamber for automated sample preparation prior to inductively coupled plasma spectrochemical analysis. The Analyst. 1994;119(5):1003.

68. Oliveira CC, Sartini RP, Zagatto EAG. Microwave-assisted sample preparation in sequential injection: spectrophotometric determination of magnesium, calcium and iron in food. Anal Chim Acta. 2000 May;413(1–2):41–8.

69. Pratt KW, Kingston HM, MacCrehan WA, Koch WF. Voltammetric and liquid chromatographic identification of organic products of microwave-assisted wet ashing of biological samples. Anal Chem. 1988 Oct;60(19):2024–7.

70. Daniel J, Batchelor J, Rhoades C, Jones B. The effect of digestion temperature on matrix decomposition using a high pressure asher. Spectrosc. 1998;19(6):198–203.

71. Froes RES, Borges Neto W, Naveira RLP, Silva NC, Nascentes CC, da Silva JBB. Exploratory analysis and inductively coupled plasma optical emission spectrometry (ICP OES) applied in the determination of metals in soft drinks. Microchem J. 2009 May;92(1):68–72.

72. Silvia J, Cadore S, Nobrega J, Baccan N. Dilute-and-shoot procedure for the determination of mineral constituents in vinegar samples by axially viewed inductively coupled plasma optical emission spectrometry (ICP OES). Food Addit Contam. 2007;24(2):130–9.

73. Carrilho EV, Nogueira AA, Nóbrega JA, Souza GB, Cruz GM. An attempt to correlate fat and protein content of biological samples with residual carbon after microwave-assisted digestion. Fresenius J Anal Chem. 2001 Oct;371(4):536–40.

74. Brenner IB, Zander AT. Axially and radially viewed inductively coupled plasmas ፖ a critical review. At Spectrosc. 2000;46.

75. conductivity v concentration.pdf [Internet]. [cited 2019 Mar 7]. Available from: http://myweb.wit.edu/sandinic/Research/conductivity%20v%20concentration.pdf

76. Sturm GSJ. Microwave Field Applicator Design in Small-Scale Chemical Processing. 2013 [cited 2019 Mar 19]; Available from: http://resolver.tudelft.nl/uuid:0407019d-248c-4061-b349-f9ea81085da1

77. Allain P, Jaunault L, Mauras Y, Mermet JM, Delaporte T. Signal enhancement of elements due to the presence of carbon-containing compounds in inductively coupled plasma mass spectrometry. Anal Chem. 1991 Jul 15;63(14):1497–8.

78. Gammelgaard B, Jøns O. Determination of selenium in urine by inductively coupled plasma mass spectrometry: interferences and optimization. J Anal Spectrom. 1999;14(5):867–74.

79. Grindlay G, Gras L, Mora J, de Loos-Vollebregt MTC. Carbon-related matrix effects in inductively coupled plasma atomic emission spectrometry. Spectrochim Acta Part B At Spectrosc. 2008 Feb;63(2):234–43.

80. Hu Z, Hu S, Gao S, Liu Y, Lin S. Volatile organic solvent-induced signal enhancements in inductively coupled plasma-mass spectrometry: a case study of methanol and acetone. Spectrochim Acta Part B At Spectrosc. 2004 Sep;59(9):1463–70.

81. Kovačevič M, Goessler W. Direct introduction of volatile carbon compounds into the spray chamber of an inductively coupled plasma mass spectrometer: Sensitivity enhancement for selenium. Spectrochim Acta Part B At Spectrosc. 2005 Oct;60(9–10):1357–62.

82. Kovačevič M, Goessler W, Mikac N, Veber M. Matrix effects during phosphorus determination with quadrupole inductively coupled plasma mass spectrometry. Anal Bioanal Chem. 2005 Sep;383(1):145–51.

83. Larsen EH, Stürup S. Carbon-enhanced inductively coupled plasma mass spectrometric detection of arsenic and selenium and its application to arsenic speciation. J Anal Spectrom. 1994;9(10):1099–105.

84. Liu S, Beauchemin D. Effect of methanol and sodium dodecylsulfate on radial profiles of ion abundance in inductively coupled plasma mass spectrometry. Spectrochim Acta Part B At Spectrosc. 2006 Mar;61(3):319–25.

85. Llorente I, Gómez M, Cámara C. Improvement of selenium determination in water by inductively coupled plasma mass spectrometry through use of organic compounds as matrix modifiers. Spectrochim Acta Part B At Spectrosc. 1997 Oct;52(12):1825–38.

86. Machát J, Kanický V, Otruba V. Determination of selenium in blood serum by inductively coupled plasma atomic emission spectrometry with pneumatic nebulization. Anal Bioanal Chem. 2002 Feb;372(4):576–81.

87. Machat J, Otruba V, Kanicky V. Spectral and non-spectral interferences in the determination of selenium by inductively coupled plasma atomic emission spectrometry. J Anal Spectrom. 2002;17(9):1096–102.

88. Pettine M, Casentini B, Mastroianni D, Capri S. Dissolved inorganic carbon effect in the determination of arsenic and chromium in mineral waters by inductively coupled plasma-mass spectrometry. Anal Chim Acta. 2007 Sep;599(2):191–8.

89. Rodushkin I, Nordlund P, Engström E, Baxter DC. Improved multi-elemental analyses by inductively coupled plasma-sector field mass spectrometry through methane addition to the plasma. J Anal At Spectrom. 2005;20(11):1250.

90. Warburton E, Goenaga-Infante H. Methane mixed plasma—improved sensitivity of inductively coupled plasma mass spectrometry detection for selenium speciation analysis of wheat-based food. J Anal Spectrom. 2007;22(4):370–6.

91. Kralj P, Veber M. INVESTIGATIONS INTO NONSPECTROSCOPIC EFFECTS OF ORGANIC COMPOUNDS IN INDUCTIVELY COUPLED PLASMA MASS SPECTROMETRY. Acta Chim Slov. 2003;12.

92. Grindlay G, Mora J, de Loos-Vollebregt M, Vanhaecke F. A systematic study on the influence of carbon on the behavior of hard-to-ionize elements in inductively coupled plasma–mass spectrometry. Spectrochim Acta Part B At Spectrosc. 2013 Aug;86:42–9.

93. Nakazawa T, Suzuki D, Sakuma H, Furuta N. Comparison of signal enhancement by co-existing carbon and by co-existing bromine in inductively coupled plasma mass spectrometry. J Anal Spectrom. 2014;29(7):1299–305.

94. Al-Ammar AS, Gupta RK, Barnes RM. Correction for non-spectroscopic matrix effects in inductively coupled plasma-mass spectrometry by common analyte internal standardization. Spectrochim Acta Part B At Spectrosc. 1999 Dec;54(13):1849–60.

95. Abou-Shakra FR, Rayman MP, Ward NI, Hotton V, Bastian G. Enzymatic Digestion for the Determination of Trace Elements in Blood Serum by Inductively Coupled Plasma Mass Spectrometry. J Anal At Spectrom. 1997;12(4):429–33.

96. Niu H, Houk RS. Fundamental aspects of ion extraction in inductively coupled plasma mass spectrometry. Spectrochim Acta Part B At Spectrosc. 1996 Jul;51(8):779–815.

97. Goossens J, Vanhaecke F, Moens L, Dams R. Elimination of interferences in the determination of arsenic and selenium in biological samples by inductively coupled plasma mass spectrometry. Anal Chim Acta. 1993 Aug;280(1):137–43.

98. Wiltsche H, Moradi F, Knapp G. Evaluation of the oscillator frequency of a free running RF generator as a diagnostic tool for inductively coupled plasma-optical emission spectrometry. Spectrochim Acta Part B At Spectrosc. 2012 May;71–72:48–53.

99. E.F. Huth, L. Kühn. Schaltungsweise zur Schwingungserzeugung mit Vakuumröhren. Ger. Pat., 310152; 1917.

100. P. Wetzl, O. Zehnder. Industrieröhren in Hochfequenzgeneratoren. BBC AG, Baden, Switzerland; 1980.

101. Maessen FJMJ, Seeverens PJH, Kreuning G. Analytical aspects of organic solvent load reduction in normal-power ICPs by aerosol thermostatting at low temperatures. Spectrochim Acta Part B At Spectrosc. 1984 Jan;39(9–11):1171–80.

102. Wiltsche H, Moradi F, Tirk P, Knapp G. Online combustion followed by carbon dioxide removal: evaluation of a new approach for the analysis of volatile organic substances by inductively coupled plasma optical emission spectrometry. J Anal Spectrom. 2014 Jul 4;29(10):1767–77.

103. Mermet JM. Use of magnesium as a test element for inductively coupled plasma atomic emission spectrometry diagnostics. Anal Chim Acta. 1991 Oct;250:85–94.

104. M. W. Blades. ‘Excitation mechanisms and discharge characteristics - Recent developments’, In: Inductively Coupled Plasma Emission Spectroscopy. Ed P W J M Boumans Wiley Intersci N Y. 1987;(90):387–420.

105. Brenner IB, Zander AT. Axially and radially viewed inductively coupled plasmas ፖ a critical review. Spectrochim Acta Part B At Spectrosc. 2000;55:1195–240.

106. Ivaldi JC, Tyson JF. Performance evaluation of an axially viewed horizontal inductively coupled plasma for optical emission spectrometry. Spectrochim Acta Part B At Spectrosc. 1995 Sep;50(10):1207–26.

107. Weir DG, Blades MW. Characteristics of an Inductively Coupled Argon Plasma Operating with Organic Aerosols Part 1I Spectral and Spatial Observations. J Anal Spectrom. 1994;9:1311–22.

108. Chan GC-Y, Hieftje GM. Spatial Emission Profiles for Flagging Matrix Interferences in Axial-Viewing Inductively Coupled Plasma-Atomic Emission Spectrometry: 2. Statistical Protocol. Anal Chem. 2013 Jan 2;85(1):58–65.

109. Mora J, Hernandis V, Canals A. Influence of solvent physical properties on drop size distribution, transport and sensitivity in flame atomic absorption spectrometry with pneumatic nebulization. J Anal At Spectrom. 1991;6(7):573.

110. Reaxys Database Beilstein Gmelin Reed Elsevier Prop SA. 2015;

111. Enos CS, Brenton AG, Lee AR. A unified view of the spin conservation rule for disparate collisional processes. Int J Mass Spectrom Ion Process. 1992 Dec;122:361–76.

112. A. E. Kramida, Y. Ralchenko, J. Reader and NIST ASD Team. in NIST Atomic Spectra Database (ver. 5.2 Online). Natl Insitute Stand Technol Gaithersburg. 2014;

113. Todolí JL, Gras L, Hernandis V, Mora J. Elemental matrix effects in ICP-AES. J Anal Spectrom. 2002;17(2):142–69.

114. Dennaud J, Howes A, Poussel E, Mermet J-M. Study of ionic-to-atomic line intensity ratios for two axial viewing-based inductively coupled plasma atomic emission spectrometers. Spectrochim Acta Part B At Spectrosc. 2001 Jan;56(1):101–12.

115. Brenner IB, Zischka M, Maichin B, Knapp G. Ca and Na interference effects in an axially viewed ICP using low and high aerosol loadings. J Anal At Spectrom. 1998;13(11):1257–64.

116. Kitagawa K, Horlick G. Deviation of the level populations of iron atoms and ions from the boltzmann distribution in an inductively coupled plasma. Part 2. Effect of an easily ionizable element. J Anal At Spectrom. 1992;7(8):1221.

117. Greenfield S, McGeachin HM. Calorimetric and dimensional studies on inductively coupled plasmas. Anal Chim Acta. 1978 Sep;100:101–19.

118. Scheffler GL, Pozebon D. Advantages, drawbacks and applications of mixed Ar–N $_2$ sources in inductively coupled plasma-based techniques: an overview. Anal Methods. 2014;6(16):6170–82.

119. Fundamental studies of mixed-gas inductively coupled plasmas [Internet]. [cited 2019 Feb 18]. Available from: https://ac.els-cdn.com/0584854794801088/1-s2.0-0584854794801088-main.pdf?_tid=7b7d205c-ae17-42e3-af0a-f45265ae6ba5&acdnat=1550493609_0623b9dc180fe83d5649848135793d4d

120. Lam JW, McLarent JW. Use of Aerosol Processing and Nitrogen - Argon Plasmas for Reduction of Oxide Intttrference in Inductively Coupled Plasma Mass Spectrometry. :6.

121. Ohata M, Takaku Y, Inagaki K, Hioki A, Chiba K. Improvement of Analytical Sensitivity by Ar-N2 Inductively Coupled Plasma in Axially Viewing Optical Emission Spectrometry. Anal Sci. 2009;25(2):161–3.

122. Agatemor C, Beauchemin D. Towards the reduction of matrix effects in inductively coupled plasma mass spectrometry without compromising detection limits: The use of argon–nitrogen mixed-gas plasma. Spectrochim Acta Part B At Spectrosc. 2011 Jan;66(1):1–11.

123. Spatially resolved electron density measurements in Ar, N2-Ar and O2-Ar ICPs using a photodiode array detection system [Internet]. [cited 2019 Feb 18]. Available from: https://ac.els-cdn.com/0584854786800970/1-s2.0-0584854786800970-main.pdf?_tid=3e8e50dc-ffbb-4fce-908e-55789b78b1d1&acdnat=1550506487_0326e1b896be986d3e2a579d9efcc5c1

124. Scheffler GL, Pozebon D. Advantages and effects of nitrogen doping into the central channel of plasma in axially viewed-inductively coupled plasma optical emission spectrometry. Anal Chim Acta. 2013 Jul;789:33–40.

125. Xiao G, Beauchemin D. Reduction of Matrix Effects and Mass Discrimination in Inductively Coupled Plasma Mass Spectrometry With Optimized Argon-Nitrogen Plasmas. J Anal At Spectrom. 1994;9:10.

126. Craig JM, Beauchemin D. Reduction of the effects of concomitant elements in inductively coupled plasma mass spectrometry by adding nitrogen to the plasma gas. J Anal At Spectrom. 1992;7(6):937.

127. Choot EH, Horlik G. Evaluation of the analytical performance of mixed gas inductively coupled plasmas. Spectrochim Acta Part B At Spectrosc. 1986 Jan;41(9):925–34.

128. Holliday AE, Beauchemin D. Spatial profiling of ion distributions in a nitrogen–argon plasma in inductively coupled plasma mass spectrometry. J Anal At Spectrom. 2003 Mar 27;18(4):289–95.

129. Chirinos JR, Kahen K, O'Brien S-AE, Montaser A. Mixed-gas inductively coupled plasma atomic emission spectrometry using a direct injection high efficiency nebulizer. Anal Bioanal Chem. 2002 Jan;372(1):128–35.

130. Donati GL, Amais RS, Williams CB. Recent advances in inductively coupled plasma optical emission spectrometry. J Anal At Spectrom. 2017;32(7):1283–96.

131. Guevara SR, Horvat M. Stability and behaviour of low level spiked inorganic mercury in natural water samples. Anal Methods. 2013;5(8):1996.

132. Fernández-Martínez R, Rucandio I, Gómez-Pinilla I, Borlaf F, García F, Larrea MT. Evaluation of different digestion systems for determination of trace mercury in seaweeds by cold vapour atomic fluorescence spectrometry. J Food Compos Anal. 2015 Mar;38:7–12.

133. Amaral CDB, Fialho LL, Camargo FPR, Pirola C, Nóbrega JA. Investigation of analyte losses using microwave-assisted sample digestion and closed vessels with venting. Talanta. 2016 Nov;160:354–9.

134. Avula B, Wang Y-H, Smillie TJ, Duzgoren-Aydin NS, Khan IA. Quantitative Determination of Multiple Elements in Botanicals and Dietary Supplements Using ICP-MS. J Agric Food Chem. 2010 Aug 25;58(16):8887–94.

135. Parker JL, Bloom NS. Preservation and storage techniques for low-level aqueous mercury speciation. Sci Total Environ. 2005 Jan;337(1–3):253–63.

136. Yu L-P, Yan X-P. Factors affecting the stability of inorganic and methylmercury during sample storage. TrAC Trends Anal Chem. 2003 Apr;22(4):245–53.

137. Rosain RM, Wai CM. The rate of loss of mercury from aqueous solution when stored in various containers. Anal Chim Acta. 1973 Jul;65(2):279–84.

138. Ahmed R, Stoeppler M. Storage and stability of mercury and methylmercury in sea water. Anal Chim Acta. 1987;192:109–13.

139. Louie H, Wong C, Huang YJ, Fredrickson S. A study of techniques for the preservation of mercury and other trace elements in water for analysis by

inductively coupled plasma mass spectrometry (ICP-MS). Anal Methods. 2012;4(2):522–9.

140. Riscassi A, Miller CL, Brooks SC. Impact of collection container material and holding times on sample integrity for mercury and methylmercury in water: Container and holding time impact on Hg. Limnol Oceanogr Methods. 2014 Jun;12(6):407–20.